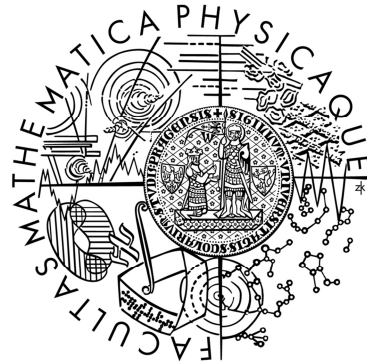


Charles University in Prague
Faculty of Mathematics and Physics

DOCTORAL THESIS



Jakub Zázvorka

Photoconductivity, photoluminescence and charge collection in semiinsulating CdTe and CdZnTe

Institute of Physics of Charles University

Supervisor of the doctoral thesis: prof. Ing. Jan Franc, DrSc.

Study programme: Physics

Specialization: Quantum optics and optoelectronics

Prague 2016

I declare that I carried out this doctoral thesis independently, and only with the cited sources, literature and other professional sources.

I understand that my work relates to the rights and obligations under the Act No. 121/2000 Coll., the Copyright Act, as amended, in particular the fact that the Charles University in Prague has the right to conclude a license agreement on the use of this work as a school work pursuant to Section 60 paragraph 1 of the Copyright Act.

In..... date.....

Motto

"All of our days are numbered. We cannot afford to be idle. To act on a bad idea is better than to not act at all. Because the worth of the idea never becomes apparent until you do it.

Sometimes this idea can be the smallest thing in the world. A little flame that you hunch over and cup with your hand, and pray it will not be extinguished by all the storm that howls about it. If you can hold on to that flame, great things can be constructed around it, that are massive and powerful and world-changing.

All held up by the tiniest of ideas."

Nick Cave: 20,000 Days on Earth, Dir. I. Forsyth & J. Pollard,
Channel 4 DVD, 2014

Acknowledgement

Our greatest achievements are never done just by ourselves. Much as the large ensemble of particles and their interaction in quantum physics forms the macrospace, similarly we are influenced by everyone around us and that leads us to who we are. Our life, the experience we gathered, is the sum of communication, interaction and learning from all the giants whose shoulders we stand on.

Even though we can see to the end of all, it is good to keep looking. And we have to realize that without the people around us, we would be blind. I do not know the future, but I am grateful for the present and very thankful for my past that lead up to writing this thesis, for all of the people guiding and inspiring me. I am thankful to all of them.

Some of those people were:

*Marie Zázvorková
Karel Zázvorka
Mirka Zázvorková
Tomáš Šimčík
Adéla Šimčíková
Sára Šimčíková
Michal Šimčík
Dana Tomešová a Josef Tomeš
Iva Nádvorníková
Zuzana Hřebcová
Hana Hlaváčková
Miroslav Hopjan
Martin Jeníček
Martin Halaj
Petra Domašinská
Alex Fauler
Michael Fiederle
Martin Pichotka
Radek Molín
Miroslav Bartošek
Kateřina Hřebíková
Michaela Zelingrová
Marek Stahl
Jakub Hájek
Tomáš Grošup
Andrea Schatralová
Michael Schröter
Tomáš Janda
Miroslav Kořínek
and many others...*

My thanks also belong to:

*SPIE society; Optics and Education
Scholarship
SPIE/OSA Charles Univ. Student
Chapter
DAAD - German Academic Exchange
Service
Baden–Württemberg–Stiftung*

Special thanks belong to my colleagues at the Institute of Physics:

*Martin Veis
Eduard Belas
Pavel Hlídek
Pavel Moravec
Roman Grill
Václav Dědič
Jakub Pekárek
Martin Rejhon
Lukáš Šedivý
Lukáš Beran
Eva Jesenská
Pavel Höschl
Jan Ulrych*

My greatest gratitude belongs to my supervisor *Jan Franc*. His guidance over the years was very inspiring and his ideas, comments and advice were always most helpful.

Název práce: Fotovodivost, fotoluminiscence a sběr náboje
v semiizolačním CdTe a CdZnTe

Autor: Jakub Zázvorka

Katedra / Ústav: Fyzikální ústav Univerzity Karlovy

Vedoucí disertační práce:

prof. Ing. Jan Franc, DrSc., Fyzikální ústav Univerzity Karlovy

Abstrakt:

Telurid kademnatý (CdTe) a jeho sloučeniny jsou perspektivními materiály pro výrobu nechlazených detektorů vysokoenergetického záření. Příprava výsledného zařízení je ale ovlivněna mnoha parametry jako jsou materiálové nečistoty a defekty, homogenita a příprava povrchu materiálu. Tato teze obsahuje detailní studii vlivu přípravy vzorků a jevů ovlivňujících spektrální rozlišení a práci výsledného detektoru. Přítomnost hlubokých hladin je zkoumána pomocí fotoluminiscence a korelována s dalšími elektro-optickými měřeními, která se zabývají vlivem strukturálních vad materiálu.

Rozbor homogenity odporu a fotovodivosti v porovnání s detektivitou vzorku a jeho elektrickými vlastnostmi je studován pomocí elektrických měření transportu a sběru fotogenerovaného náboje. Získané výsledky jsou vyhodnoceny a porovnány s teoretickým modelem a výpočty. Naměřené jevy jsou objasněny pomocí teorie posunu Fermiho hladiny.

Dále je zkoumán vliv přípravy povrchu a jeho oxidace na měření odporu a fotovodivosti a celkové chování CdTe a CdZnTe. Jsou pozorovány změny vlastností detektorů v čase po jejich opracování. Časová změna velikost svodových proudů je korelována s tloušťkou povrchové vrstvy TeO₂.

Klíčová slova:

CdTe, hluboké hladiny, prostorový náboj, příprava povrchu.

Title: Photoconductivity, photoluminescence and charge collection
in semiinsulating CdTe and CdZnTe

Author: Jakub Zázvorka

Department: Institute of Physics of Charles University

Supervisor of the doctoral thesis:

prof. Ing. Jan Franc, DrSc., Institute of Physics of Charles University.

Abstract:

Cadmium telluride and its compounds with zinc are the material of choice in spectroscopic room temperature high energy radiation detectors. The development of the final device is influenced by many parameters, including material impurities and defects, homogeneity and surface preparation. This thesis offers a comprehensive investigation of the detector fabrication process and of the parameters and physical effects influencing the spectroscopic resolution and performance of the detector. Structure of deep levels is investigated through photoluminescence and correlated with other electro-optical measurements dealing with the impact of structural imperfections of the material and their effect.

The influence of resistivity and photoconductivity homogeneity on the detector performance is studied through electrical measurement of the charge carrier transport and charge collection of the sample. Obtained results are explained using the Fermi level shift theory and confronted with a theoretical model and calculations.

The impact of surface treatments and oxidation of the surface on resistivity, photoconductivity and the general performance of CdTe and CdZnTe samples is investigated. Changes in the attributes of the detector over time are observed. Correlation of studied surface TeO₂ oxide layer growth with decreased leakage current over time after surface etching is made.

Keywords:

CdTe, Deep levels, Space charge, Surface preparation.

Contents

1 Introduction	1
1.1 CdTe and CdZnTe	2
1.2 Detector preparation	3
1.3 Motivation and goals	5
2 Theory	6
2.1 Energetic levels inside the bandgap	6
2.2 Origin of the deep levels	8
2.3 Charge transport	10
2.4 Charge trapping and recombination	12
2.5 Charge collection	14
3 Experimental Methods	17
3.1 Photoluminescence	17
3.2 Contactless resistivity mapping (Corema)	19
3.3 α -spectroscopy and transient-current-technique (TCT)	21
3.4 Ellipsometry	23
3.5 Samples	24
RESULTS	
Deep Level Investigation	26
4.1 Photoluminescence	26
4.2 Photoluminescence of CdTe	26
4.2.1 Excitation above the bandgap, $\hbar\omega_{EXCIT} > E_G$	27
4.2.2 Temperature dependence with excitation above bandgap	30
4.2.3 Excitation spectroscopy at 4.6 K	32
4.2.1 Temperature dependence with excitation below bandgap, $\hbar\omega_{EXCIT} < E_G$	33
4.2.1 Spectral position of PL peaks and PLE spectra	35
4.2.2 Temperature and excitation dependence of PL peaks	39
4.2.3 Comments on the individual PL components	41
4.2.4 PL quenching activation energies	44
4.2.5 Comparison to results in other papers	45
4.3 Photoluminescence of CdZnTe	47

4.4 Chapter summary	51
5 Charge transport and detector performance	53
5.1 Contactless Sample Characterization	53
5.2 Detector Performance	56
5.2.1 Electron Collection	56
5.2.2 Hole Collection	65
5.3 Theoretical model	70
5.4 Chapter summary	75
6 Surface Preparation	76
6.1 Surface effects on deep levels	77
6.2 Resistivity and Photoconductivity	81
6.3 Surface effect on detector performance	90
6.4 Detailed investigation of contactless resistivity	92
6.5 Surface oxide thickness and growth	98
6.6 Chapter summary	107
7 Conclusions	108
References	110
List of Tables	118
Symbols and abbreviations	119

1. Introduction

“The discovery of semiconductors is one of the great scientific and technological breakthroughs of the 20th century. It has caused major economic change, and has perhaps changed civilization itself. Silicon, for example, now plays as important a role in our lives as carbon did in the 19th century [...].

The solids known as semiconductors have been the subject of very extensive research over recent decades, not simply because of their intrinsic interest but also because of ever numerous and powerful applications: rectifiers, transistors, photoelectric cells, magnetometers, solar cells, reprography, laser, and so forth [...]. All this industrial development has come into existence only because physics allows us to understand the specific properties of semiconductors, and then use this understanding to create ‘electron machines’ in the form of semiconductor devices.”

Cited from [1] B. Sapoval and C. Hermann,
Physics of semiconductors.
New York: Springer, 1995.

One of the useful applications of semiconductor materials and technology is the detection of high-energy radiation, meaning the X-ray and Gamma-ray spectra. Physical properties of semiconductors must be used for the detection of such radiation. There are two main approaches to the detection of the incoming radiation, direct and indirect. The latter approach is the conversion of the high-energy radiation into light in the visible spectra range by absorption, relaxation of the excited charge carriers and consequent re-emitting of energy through light at a different wavelength, usually in the visible range. The converted radiation is then detected with a common silicon detector. In this method the semiconductor serves as a mediator between the high-energy radiation and the silicon detector, hence being labeled as indirect measurement. Semiconductors with such properties of light conversion are called scintillators.

Direct approach involves materials with a high enough atom number for a better absorption which can transform the incoming radiation into electric charge. The charge is consequently collected at the contacted surface of the material.

The amount of collected electrons and holes corresponds to the energy of the measured radiation and when evaluating its spectroscopic information can be obtained. Direct approach of radiation detection usually has a better spectroscopic, but worse spatial resolution, when compared to scintillators. One of the materials suitable for radiation detection is cadmium telluride (CdTe) and its compounds with zinc (CdZnTe) and selenium (CdTeSe, CdZnTeSe).

1.1. CdTe and CdZnTe

Cadmium telluride is a semiconductor of the II–VI group which is nowadays mostly used for X–ray and gamma–ray detection [2]. It falls into the category of detectors operated at room temperature. It does not have to be cooled with liquid nitrogen, in contrast to germanium. CdTe has a relatively high average atomic number ($Z \approx 50$), which attests to a good absorption of high energy radiation, as the absorption ratio depends on the 4–5 power over the atom number ($a \approx Z^{4-5}$). The energetic bandgap between the valence and conduction band was measured as $E_G(4.2 \text{ K}) = 1.606 \text{ eV}$ at the temperature of cooled helium. For room temperature (295 K) the bandgap was estimated at $E_G = 1.526 \text{ eV}$ [3]. The larger bandgap (compared to silicon) results in a lower thermal noise of the electrons in the conduction band. CdTe is a direct semiconductor, so an electron can be excited from the valence band into the conduction band without the assistance of crystal lattice vibrations, the phonons.

The material is usually grown using the Vertical–Bridgman–Method (VGF) or the Travelling–Heater–Method (THM). By itself the material can contain various defects and impurities acting as shallow donors or acceptors and hindering a higher resistivity of the detector and a lower achievable dark current. The lowest possible dark current (leakage current) is desirable because it improves the final spectral resolution of the detector. The presence of the shallow energetic levels can be counterbalanced with the process of compensation. A defect of impurity causing a deep level in the middle of the bandgap is induced. The charged electron or holes at the shallow levels recombine or are trapped at the deep level and are efficiently compensated. This pins the Fermi level of the semiconductor to the middle of the bandgap and the highest possible resistivity is achieved. The mostly used dopants for the compensation process are chlorine or indium, but many elements

were tried and the results published. Theoretically estimated maximal resistivity value of CdTe is $2 \times 10^{10} \Omega \cdot \text{cm}$.

With the addition of zinc to the crystal, the bandgap of the material increases [4]. This effect is usable in few of the applications that CdTe offers. But mostly it is used to lower the leakage current of the detector even more and to achieve the resistivity value up to $\sim 10^{11} \Omega \cdot \text{cm}$ through the process of compensation. The typical content of zinc is about 10%. There are several commercial vendors producing CdTe and CdZnTe samples, including Acrorad (Japan), Redlen (Canada), Kromek (USA) and EURORAD (France). Nevertheless, the investigation of the material and the optimization of the detector fabrication still engages many research centers and facilities [5].

Nowadays the CdTe and CdZnTe detectors are used frequently in medical imaging (in computer tomography, SPECTs etc.), but the material has found its application in various fields. Because of its transparency in the infrared spectrum, it is used as windows in infrared optics, including windows for CO and CO₂ lasers. CdTe has a high electro-optic effect and is used for electro-optical modulators. With the addition of mercury (HgCdTe) it serves as an infrared detector; and sandwiched with cadmium sulfide (CdS) to form a p-i-n structure, it is used as a photovoltaic cell.

1.2. Detector preparation

The preparation of the final CdTe ionization radiation detector contains several vital steps that need to be investigated. In this thesis the process of detector development is divided into three sections: deep levels, electrical characterization, and surface treatment.

The growth of CdTe crystals is usually done by either VGF or THM methods. The starting material of cadmium and telluride “pellets” is placed into an ampoule that is heated up to the melting point of both constituents. Afterwards the melt is subjected to a temperature gradient and through cooling the crystal is slowly grown. The growth process takes from days up to weeks, depending on the chosen cooling rate. The intentional doping element used to achieve high resistivity by compensation is placed into the ampoule prior to melting. After the growth the crystal is inspected and cut into smaller samples. Monocrystalline material is

expected after a good, successful growth. Otherwise the individual material grains must be cut from the ingot. CdTe crystals can often exhibit twin grains or sub-grain boundaries and may contain inclusions because of the deviation from stoichiometry of the melt. As an effect of the segregation of zinc, its ratio can vary throughout the crystal growth axis.

As the crystal growth is a complicated and costly process, the composition of defects and impurities and their effects must be investigated through e.g. glow-discharge-mass-spectroscopy (GDMS). Impurities and defects can be embedded from the crystal ampoule, doping, tension at the crystal surface, etc. The deep energetic levels are of interest due to their participation in trapping and recombination of free photogenerated charge. When charge is trapped at the deep level, space charge is induced inside the detector and the effect of polarization can occur. In this phenomenon the inner electric field is concentrated under one of the biased electrodes and a dead layer can be formed under the other electrode. Charge carriers are not accelerated in this part of the sample and can be transported only through diffusion. This can hinder the operability of the detector. Publications suggest a connection between the deep levels found in the spectral range of 1.1 eV and the effect of polarization of the detector, which renders the device inert to incoming radiation [6]. Also further effects of Fermi level pinning by doping are to be investigated as it can influence the sensitivity and performance of the material. The commonly used methods for the deep level investigation are photoluminescence (PL), photo-induced current transient spectroscopy (PICTS), deep level transient spectroscopy (DLTS), thermo-electric effect spectroscopy (TEES), and others.

After the crystal growth and cutting of the ingot into smaller plates, the properties of the material critical for radiation detection have to be evaluated. Usually the wafer is cut into small samples and metal contacts on the surface are prepared for further measurement. Resistivity of the sample, together with charge carrier concentration and mobility is investigated by Hall effect measurements and current-voltage characteristics. A good value of electron mobility for CdTe is considered at about $1000 \text{ cm}^2 \cdot \text{V}^{-1} \cdot \text{s}^{-1}$. Resistivity and response to illumination (photoconductivity) can also be obtained by contactless measurement, not having to prepare the metal contacts. The contactless measurement can correlate with the Hall effect measurement and in many cases can predict the performance of the sample in the meaning of the electrical noise and resolution with radiation detection [7].

The response to the impact of α -particles and gamma-rays shows manifold spectra and samples with good detecting abilities can be selected. Of course, scientifically it is important to investigate the worsened properties in some part of the crystal and study the effects that led to such behavior.

Lately, the surface preparation effects on CdTe samples have been of much interest. The surface itself can act as a short-circuit and can negatively influence the detector preparation. The current flowing on the surface of the detector can be greater than the bulk current by orders of magnitude [8]. As the material undergoes many technological steps (cutting, lapping, polishing, etching etc.), their influences are thoroughly investigated. Nevertheless, many studies have shown contradictory results, and an optimal surface processing is still under discussion.

After the preparation of the detector, it is connected to an electronic readout system that can evaluate the current pulses induced by absorbed radiation. Detailed information on the electronic part can be found in [9]. The focus of this thesis is an investigation of fundamental properties of CdTe and CdZnTe material and of the technological process used for detector preparation.

1.3. Motivation and goals

CdTe and its compounds have been investigated at the Institute of Physics of Charles University in Prague for many years. The laboratory of crystal growth produces and develops the growth process. Commercial materials are investigated in the department of semiconductors and semiconductor optoelectronics, too. However, there are many steps leading to the preparation of a high-quality radiation detector. In the previous chapter the three most important parts were labeled as: investigation of deep levels, electrical characterization, and surface preparation.

The motivation for this thesis is to investigate closely the principles, physical processes and effects of all three detector production steps, and to research their impact on the final detector performance. The aim is to establish a correlation between the mostly used investigation methods and to connect the results into a comprehensive study of CdTe physics. One of the thesis goals is to develop an optimal material characterization and detector preparation method.

2. Theory

“Even though some properties of semiconductors were discovered experimentally in the course of the 19th century, an understanding of the origin of this behavior had to await the advent of quantum mechanics.” [1]

2.1. Energetic levels inside the bandgap

The energetic bands are a result of a perfect periodic potential of the atoms placed in a crystal lattice [10]. In reality, crystalline materials evince many structural imperfections created in the growth process (by temperature gradient, segregation, melt convection etc.). Unwanted atoms of different elements can also be embedded into the structure, creating impurity centers and effectively disrupting the periodicity of the crystal [11]. These defects act as scattering centers for the charge carriers. Interestingly enough, the imperfections play an essential role in modifying conduction electron concentration. A perfectly clean and pure silicon crystal in thermal equilibrium would contain only 10^{-12} free electrons per one atom [1]. Considering this, it is clear that the majority of free electrons in a real semiconductor material comes from impurities and defects. Sapoval [1] demonstrates the effect of impurities on the example of a phosphorus atom disrupting the silicon lattice. The same example with other defects is shown in Fig. 2.1.

The phosphorus atom, by having one valence electron more than silicon, has one remaining electron after creating covalent bonds with neighboring atoms. Phosphorus acts like an electron donor. The electron can afterwards be excited into the conduction band. The energy needed for the excitation depends on the nature of the impurity atom and can be lower than the bandgap (depending on atom size, nuclear charge, dielectric constant etc.). This way a new allowed energy state is created in the bandgap. If the energy for the electron excitation in the localized atom is small compared to the width of the bandgap, the defect is called shallow donor. Otherwise, if the energy level is induced at more than a few thermal energies $k_B T$ from the minimum of the conduction band, it is named deep level.

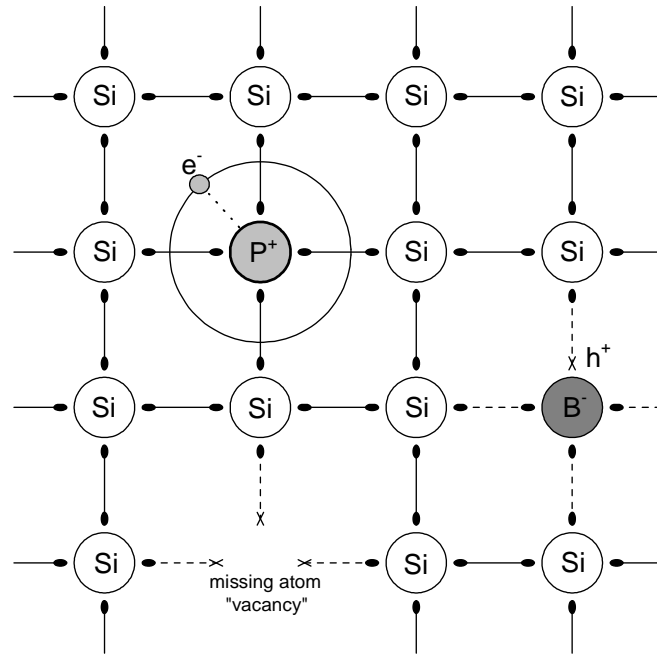


Fig. 2.1 Example of impurities and defects in a silicon crystalline structure. Phosphorus and boron impurities act as a donor and acceptor, respectively. Further defects including crystal imperfections can cause deep levels.

In contrast to donors, if the impurity consists of an atom having less valence electrons than its neighbors, it must take an electron to form the covalent lattice bond. This way a vacant electron place is created and the defect is denoted as acceptor. As in the case of donor, depending on the atom and the structure, shallow and deep acceptors can be distinguished. Simple schema of deep levels is depicted in Fig. 2.2.

The distinguishing between shallow levels and deep levels lies not only in the distance from the valence or conduction band, the form of a related wave-function also plays a significant role. Defects and impurity states causing deep levels cannot be described using the simple hydrogen-like atom model. The states forming the deep levels are more localized and must be calculated using accordingly modified wave-functions. The theory behind deep energetic levels is more complex and is described e.g. in [12]. The deep levels play a larger role in the electron-hole recombination and trapping than shallow levels; and they consequently influence the final semiconductor properties.

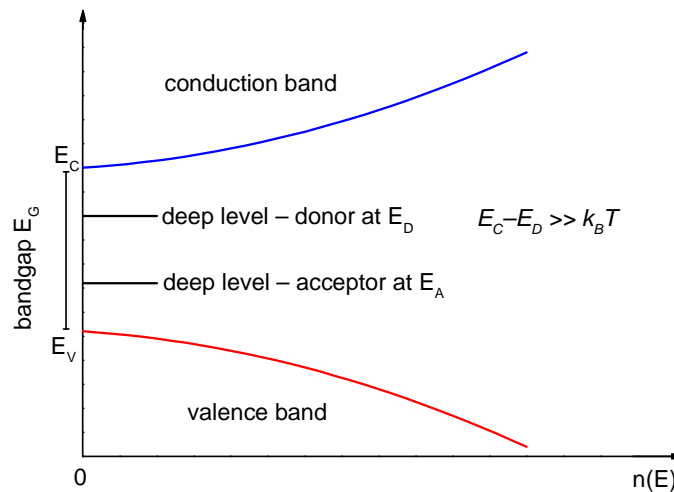


Fig. 2.2 Density of states $n(E)$ in a semiconductor near bandgap; simple depiction of deep levels.

2.2. Origin of the deep levels in CdTe

The deep levels in CdTe and CdZnTe have been studied by many research groups through various investigation methods including PICTS, DTLs, PL, etc. The goal of the research was to match the deep level to a defect or impurity in the crystal lattice of the material and to modify the growth process (induce a different dopant or adjust the growth parameters) to optimize the detector performance.

Castaldini *et. al.* [13] and Mathew [14] have both published results from extensive studies of the deep level structure. Many deep levels can be found inside the bandgap of CdTe and CdZnTe. The levels with larger influence can be those with a higher trapping cross-section. Two main levels are found in most of the measurements, one being near the middle of the bandgap, whereas the other is in the range around 1.1 eV. The latter deep level seems to be connected with space charge accumulation and polarization of the detector [6] and therefore will be in closer focus in chapter 4 of this thesis, where the results of a thorough investigation of photoluminescence band around 1.1 eV is presented. The complexity of the deep levels issue can be illustrated by the example of this particular PL band.

Numerous studies done using low-temperature photoluminescence and/or cathodoluminescence (CL) since the 1950's have shown that a broad band in the spectral region around 1.1 eV is often observed in single crystal,

high resistivity materials, see [15]. Intensity and/or position of the “1.1 eV” PL band can be influenced by various treatments, e.g.:

- annealing in Cd vapor [16], [17];
 - plastic deformation [17]–[19];
 - dislocation – e.g. dislocation induced by inclusions/precipitates [20], [21];
 - concentration of extended defects [22];
 - composition of an etching agent [23];
- and other types of treatments.

PL spectra changes in this spectral range can be given in relation to electric conductivity type and its value [24]–[26]. Several types of the 1.1–eV bands were reported in [27]. Decomposition into two or three components by a fitting procedure was used in [16], [28], [29].

Although the deep levels of CdTe and CdZnTe have been investigated thoroughly with photoluminescence, the method itself cannot reveal a precise origin of the deep levels by assigning them to particular defects. Nevertheless, some examples of published opinions can be stated. In many luminescence studies, a broad band around 1.1 eV is visible and dominant. In this thesis it is denoted as the “1.1 eV” band, including the spectral contributions from 0.9 to 1.25 eV. The components of the “1.1 eV” band were tentatively attributed to native defects, impurities and extended defects (dislocations and defects in their neighborhood). All “simple” native defects like vacancies V_{Te} [27], V_{Cd} [30], antisite Te_{Cd} [31], interstitials Te_i and their complexes [29] were proposed to be the origin of the PL band. A recombination in donor–acceptor pairs (where both donor and acceptor are deep) has been proposed. The splitting of the “1.1 eV” band was suggested to be caused by the different space distance of a deep donor and a deep acceptor; 1.046 eV and 1.129 eV for the closest arrangement and for the second closest neighbors, respectively. As possible candidates for deep donors and deep acceptors vacancies V_{Te} and interstitials Te_i were suggested, respectively.

Babentsov and James [32] discussed properties of anion vacancies in Zn– and Cd–related chalcogenides with the conclusion that the deeper PL band (at 0.8 eV in CdTe) is due to a recombination at the vacancy V_{Te} , whereas the “1.1 eV” PL band could be caused by either a recombination at the $V_{Cd} - V_{Te}$ vacancy pairs or by some impurity–related level.

A lot of candidates for defects causing deep levels can be found in papers dealing with calculation of formation energy for various defects [33]–[35]. Unfortunately, the results still remain controversial. Differences between results of various authors and the accuracy (usually much worse than 0.1 eV) of the calculation do not allow us the use of the results directly for a credible assignment of particular deep levels obtained in experiments.

Some impurities have been found to create PL bands near 1 eV. Moreover, not only “heavy” atoms like Fe, Sn or Ge can cause deep levels. Also “light” atoms (oxygen, hydrogen) can take part in the generation of a deep level. Du *et al.* [35] investigated various configurations of hydrogen bound to oxygen. Complexes of the O_{Te} –H type could play an important role in pinning the Fermi level near the middle of the bandgap [34], [35] because of a lower formation energy than those for native defects.

Deformation of the crystals is expected to create various types of dislocations. Hümmelgen and Schröter [36] found that the indentation of the p–type CdTe generates glide dislocations marked as Te(g) and Cd(g). The dislocations induce defect levels with ionization energy 0.44 eV and 0.43 eV, respectively. The complementary energy is $E_G - 0.44 \text{ eV} \approx 1.17 \text{ eV}$. The Y–line (1.47 eV) was assigned to a recombination of excitons bound to Te(g).

Kim *et al.* [24] reported that a characteristic behavior of the DLTS–peak near 1.1 eV (observed for CdMnTe and CdZnTe) corresponds to free carrier trapping on extended defects (dislocations) because the activation energy varies with the bias. The intensity of the I–DLTS (current DLTS) peak follows a logarithmic dependence on the trap filling pulse width. It has been connected with the PL “1.1 eV” band as well. Babentsov *et al.* [37] discussed the effects of uniaxial plastic deformation, indentation, and scribing and stated that moving dislocations introduce one–dimensional chains of defects (e.g. vacancies) that are not stable at room temperature. The result is a higher concentration of “usual” point defects with levels in the bandgap.

2.3. Charge transport

The electrons from the valence band can be excited (thermally, optically) into the conduction band. By this excitation they leave a vacant place in the valence band.

After the application of bias, the electrons in the conduction band move in the electric field. Because of the vacant place in the valence band, the electrons are moving in the electric field as well, always filling up the empty quantum state and creating a new one in their previous position. The collective movement of electrons in the valence band can be approximated and simplified by introduction of a new quasi-particle, the hole. It has an opposite charge to the electron and an opposite momentum than the electron excited into the valence band. By excitation, the pair electron-hole in the corresponding bands is formed. Both of them are collectively named charge carriers.

The charge carriers can be transported in the semiconducting material according to the drift-diffusion equation

$$j_e = en\mu_e E + k_B T \nabla n + e\zeta_n \nabla T, \quad (2.1)$$

where e is the absolute value of elemental charge of the electron, n is the electron concentration, E is the electric field, μ_e is the electron mobility and ζ_n is the Soret coefficient. Please note that this is only the electron part of the equation, the transport for holes would be written accordingly, with concentration of holes, hole mobility etc. The first part of the equation represents the drift in an electric field and is usually described by the conductivity $\sigma_n = en\mu_e$ and is equivalent to the macroscopic Ohm's law. The middle part denotes the diffusion of the charge carriers in a concentration gradient. The final part describing the Soret effect is usually neglected in the calculations.

After excitation and generation of electron-hole pairs the concentration of the corresponding charge carrier is increased by the addition of Δn electrons. The electron drift-current will be

$$j_{e\text{drift}} = e(n_0 + \Delta n)\mu_e E = en_0\mu_e E + e\Delta n\mu_e E. \quad (2.2)$$

Depending on the origin of the charge carrier before excitation, intrinsic (thermal) and impurity conductivity can be distinguished. In the case on intrinsic conductivity, caused by band-to-band transition, both electrons and holes are contributing to the current. Conductivity can also be caused by excitation of a charge carrier from

or to an impurity state, in which case only one type of charge carriers can contribute to the electric current.

2.4. Charge trapping and recombination

The statistics of the generation and recombination of electrons and holes in a semiconductor is described by the Shockley–Read–Hall model [38], [39].

The energy levels inside the bandgap, formed by impurities and defects, act as charge carriers traps and recombination centers. If the trapping probabilities of the electron and hole are equal on the specific energy level, it is denoted as recombination center. If the trapping probability of one carrier type is greater than the other one, the defect level is called electron or hole trap.

Assuming one deep energy level E_t with the concentration N_t , the trapping cross-sections for electrons and holes are S_e and S_h , respectively. The concentration of electrons already present on the level inside bandgap is n_t . The electrons can only be trapped in an empty state of the deep level. The electron trapping rate expressed with the electron speed v_e and the concentration of free electrons n will be

$$S_e v_e (N_t - n_t) n = \gamma_e (N_t - n_t) n. \quad (2.3)$$

In contrast to electrons, holes can only be trapped in a state filled with electrons. The trapping rate of holes can therefore be written as

$$S_h v_h n_t p = \gamma_p n_t p, \quad (2.4)$$

where v_h is the hole speed and p is the concentration of holes.

The trapped charge carriers can be thermally released back to the corresponding band with the probability α_e and α_h , respectively for electrons and holes. In the thermodynamic equilibrium (denoted with the subscription 0) the free electron concentration does not change. Therefore the trapping and thermal release are of the same value and the concentration of electron on the deep level is described as

$$n_{t0} = \frac{N_t}{\frac{\alpha_e}{\gamma_e n_0} + 1}. \quad (2.5)$$

Electrons follow the Fermi–Dirac statistics and are expressed

$$n_{t0} = N_t f = \frac{N_t}{\exp\left(-\frac{E_F + E_t}{k_B T}\right) + 1}. \quad (2.6)$$

Comparing the two previous equations with the distribution for free electrons the thermal release can be written as

$$\alpha_e n_t = \gamma_e N_C n_t \exp\left(-\frac{E_F}{k_B T}\right) = \gamma_e n_t n_1, \quad (2.7)$$

where N_C is the concentration of energy states in the conduction band and n_1 is the concentration of electrons with the Fermi level being pinned to the deep level. The equations for holes are derived similarly.

The trapping and de–trapping from the deep level therefore follows

$$\frac{dn_t}{dt} = \gamma_e (N_t - n_t) n - \gamma_h n_t p - \gamma_e n_t n_1 + \gamma_h (N_t - n_t) p_1. \quad (2.8)$$

As mentioned above, the trapped charge carriers have two options: recombination with the opposite carrier or thermal excitation. Some basic trapping processes are depicted in Fig. 2.3.

The trapped carriers do not contribute to the conductivity and the electric current as they cannot be transported from the localized state inside the bandgap. The trapping of a charge carrier forms a space charge inside the material and can heavily influence the applications of semiconductors.

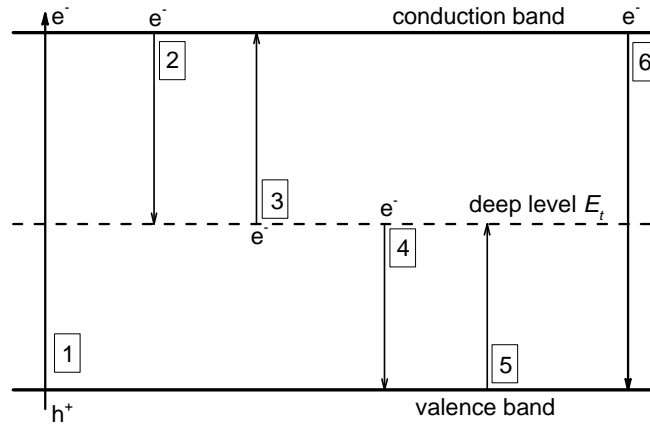


Fig. 2.3 Schema of the basic generation, recombination and trapping processes: 1) electron–hole pairs generation; 2) electron capture on the deep level; 3) electron thermal escape to the conduction band; 4) hole capture on the deep level; 5) hole thermal emission to the valence band; 6) band–to–band recombination.

2.5. Charge collection

The principle of the increased electron concentration after illumination of the semiconductor material is utilized in the application of radiation detection. The absorbed radiation excites electrons into the conduction band and generates electron–hole pairs. The free electrons are accelerated in an applied electric field and are transported to sample surface and a metal electrode. There the charge is collected and its amount gives the information of the absorbed radiation energy as the number of generated electrons is proportional to the radiation energy. The Shockley–Ramo theorem states that the moving charge inside the semiconducting material induces a charge Q on the collecting electrode [40]. The charge on the electrode Q and the induced current i on the electrode are given by

$$Q = -e \phi_0 ; i = e v E_0(x), \quad (2.9)$$

where e is the elemental charge (absolute value corresponding to electrons and holes), v is the velocity of the charge carrier, ϕ_0 and $E_0(x)$ are the electric potential and field at the instantaneous position of e in the case that the selected electrode is at unit potential and all other electrodes are grounded, all other charge removed. They are called the weighting potential and weighting field, respectively.

There are several detector layouts that work with the weighting potential to increase the performance of the radiation spectra acquisition. The simplest electrode arrangement is in the case of a planar detector, see Fig. 2.4.

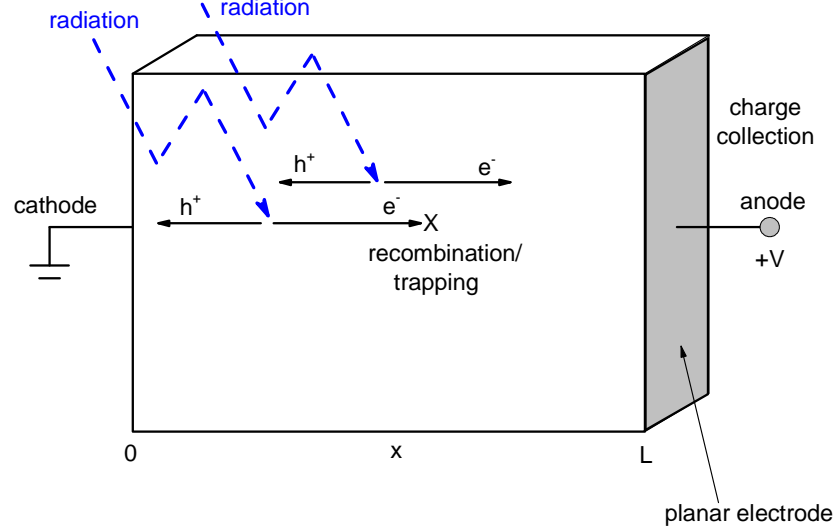


Fig. 2.4 Charge collection in a planar detector.

There are other detector layouts, e.g. pixel detector, Frisch grid, coplanar detector etc. Their weighting potential must be calculated accordingly, see [41]. The charge collection is influenced by trapping and recombination inside the bulk on the defects and impurities as described earlier.

The amount of the collected charge also depends on the bias applied to the detector. With a higher electric field the charge carriers become more accelerated and arrive at the electrode faster, some of them faster than time needed for their capture or recombination. The charge collection efficiency

$$CCE = \frac{Q}{Q_0} = \frac{\mu_{e,h}\tau_{e,h}U}{L^2} \left(1 - e^{-\frac{L^2}{\mu_{e,h}\tau_{e,h}U}} \right) \quad (2.10)$$

describes the dependency on the applied bias. The charge generated by radiation absorption is Q_0 , whereas the charge collected is Q . The applied voltage is denoted as U , the width of the sample as L . The mobility–lifetime product $\mu_{e,h}\tau_{e,h}$ corresponding to the electron and hole, respectively, is an important characterization parameter of the detector sample. A high mobility–lifetime product marks a good

performance of the material in the radiation detection. Therefore its investigation falls into standard characterization methods for detectors. Charge collection was also correlated with the photoconductivity measurement [42].

3. Experimental Methods

3.1. Photoluminescence

Photoluminescence is one of the important tools for material characterization and mainly for the study of shallow and deep energy levels created by defects, impurities and their complexes. It utilizes the recombination of charged carriers after their excitation through illumination. Photons incoming from an excitation source (usually laser) are absorbed in the studied material and give their energy to atoms and molecules. In the case of semiconductors, electrons or holes are excited into the conduction or valence band, respectively. After excitation, a non-radiative relaxation through energy exchange with the crystal lattice, assisted by phonons, can occur. Through the transition of the excited charge carrier to a state with a lower energy, the energy difference can be released in the form of a one carrier – one photon. Basic model of photoluminescence is shown in Fig. 3.1. Detailed description of the luminescence processes and various luminescence types can be found in [43].

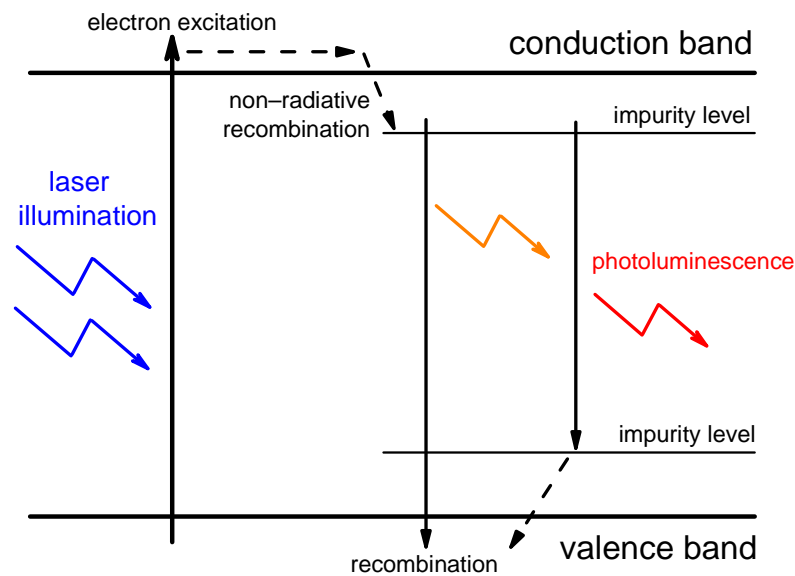


Fig. 3.1 Simplified model of the photoluminescence process in a semiconductor.

The luminescence spectra measured under excitation by photons of energies above the bandgap (1.606 eV at 4 K) in the spectral range of 1.2 – 1.6 eV represent standard characteristics of samples.

Typical structure in the photoluminescence measurement, including free exciton, exciton bound to donor/acceptor, exciton bound to doping element and their phonon replicas; is observed in CdTe and CdZnTe. Excitons bound to shallow acceptors like Na, Li, P, as well as peaks connected with donor–acceptor pair of the shallow defects and their phonon replicas are observed in the vicinity of the bandgap energy. Around 1.4 eV a broad band composed of several phonon replicas of the zero phonon line (ZPL) in the case of CdTe is visible. It tends to be attributed to special case of an acceptor: Cd vacancy with shallow donors forms a donor–acceptor pair. It is called the A–center. Other acceptors in this spectral range are attributed to be caused by Cu or Ag defects. Below 1.2 eV deep levels of the material can be found, however these investigations are published less frequently.

Photoluminescence of semiconductor samples is commonly excited by photons with energy higher than the bandgap of the material, $\hbar\omega_{EXCIT} > E_G$. Below gap excitation $\hbar\omega_{EXCIT} < E_G$ has been reported very rarely. The investigation of donor–acceptor pairs with different space distance of the acceptor from the donor (so called selective pair luminescence – SPL) has to use below–bandgap excitation. The SPL has been reported for CdTe crystals ([44] and references therein). An application of excitation at photon energies at the Urbach tail of the absorption edge (several meV below the bandgap) has been proven to be very useful because of PL excitation in the bulk of samples. Therefore, a higher PL signal can be obtained due to partial elimination of surface recombination [26], [44].

In the setup used in this thesis, the measured sample was placed in the helium flow cryostat Optistat (Oxford Instruments). The luminescence was excited either by a red line (638 nm, 1.94 eV) coming from a semiconductor laser Radius (Coherent) or from a tunable Ti:Sapphire laser Millennia pro 5sJ (Spectra Physics) in the range of 1.25 eV to 1.7 eV. The luminescence spectra were measured by the Bruker IFS 66s FTIR spectrometer equipped with a CaF₂ beamsplitter and a Si photodiode and liquid nitrogen cooled Ge and InSb detectors. Excitation radiation was blocked in front of the spectrometer by edge low pass filters Semrock 980 nm (1.27 eV), 830 nm (1.49 eV), 808 nm (1.53 eV) and 785 nm (1.58 eV). Only a color glass filter in front of the Si detector was used to eliminate the scattered light coming from the red laser.

3.2. Contactless resistivity mapping (Corema)

The principle of the contactless determination of a semiconductor wafer's resistivity was developed at the Fraunhofer-Institut in Freiburg, Germany. R. Stibal [7] published a paper on the measurement theory and the obtained resistivity correlation to measurement with contacts on the material GaAs, although in the publication described as time dependable charge measurement (TDCM).

Contactless resistivity measurement of contactless resistivity mapping employs the dielectric properties of the material as described in [7]. The sample (resistance R_S and capacity C_S) is placed between two electrodes, laying on the bottom one while having an air gap (capacity C_A) between the top electrode and the sample. The substitute electrical schema of this wiring is shown in Fig. 3.2.

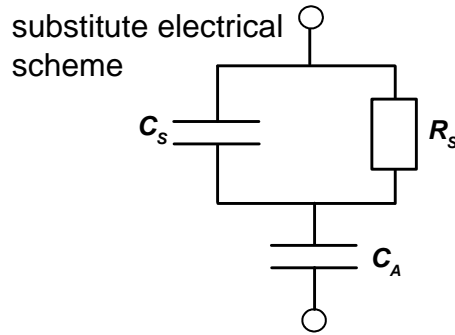


Fig. 3.2 Substitute electrical schema in the contactless resistivity measurement.

After applying bias, the electrodes act as a capacitor and the whole system consisting of the material and the air gap is charged. The top electrode is encapsulated in a guard ring electrode that is charged evenly with the measuring top electrode to prevent lateral charge accumulation. Evaluating the substitute electrical schema, the charging should follow a simple exponential behavior

$$Q(t) = Q_0 + \frac{C_A^2}{C_A + C_S} U \left(1 - e^{-\frac{t}{\tau_S}} \right), \quad (3.1)$$

where

$$R_S = \frac{\tau_S}{C_A + C_S}, \quad (3.2)$$

while τ_S being the charging time of the sample and U is the applied bias. By fitting of the measured charging curve with the all necessary parameters the sample, resistivity can be obtained. The resistivity is then calculated using

$$\rho = \frac{Q_0 \cdot \tau_S}{\varepsilon_0 \cdot \varepsilon_r \cdot Q_{inf}}, \quad (3.3)$$

where Q_0 is the dielectric charge of the material, Q_{inf} is the total charge of the capacitor, τ_S is the charge relaxation parameter; and ε_0 and ε_r are the vacuum permittivity and material relative permittivity, respectively. Throughout this study the value $\varepsilon_0 = 8.85419 \cdot 10^{-14} \text{ F} \cdot \text{cm}^{-1}$ is used. The value for relative permittivity $\varepsilon_r = 10.6$ is taken from [45] and used from now on throughout this thesis. Employing a x–y stage the resistivity of the sample can be mapped stepwise point by point and the distribution of the resistivity can be obtained.

The setup used for contactless resistivity measurement is the commercially available COREMA apparatus by Semimap GmbH. However the used setup has a modified bottom electrode made not from gold but from a transparent indium–tin–oxide layer on silicon glass. This serves for illuminating the sample and for contactless photoconductivity measurement. An illustrative schema of the setup is portrayed in Fig. 3.3. The light source used in this thesis was an SPM2 monochromator.

Photoconductivity was evaluated as the difference between reciprocal values of resistivity with and without illumination

$$g = \frac{1}{\rho_{light}} - \frac{1}{\rho_{dark}}. \quad (3.4)$$

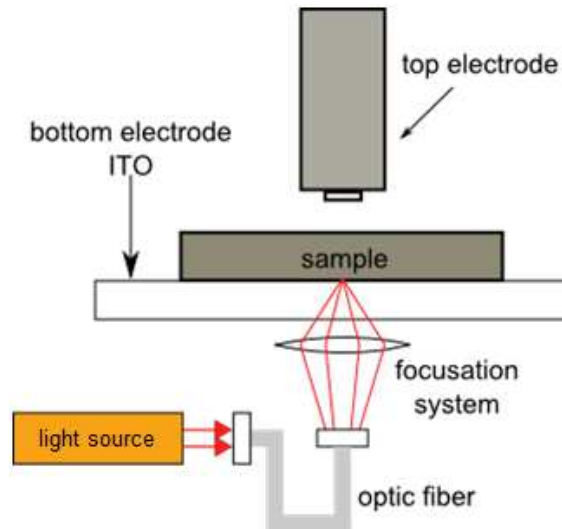


Fig. 3.3 *Illumination setup on the modified contactless resistivity mapping apparatus.*

3.3. α -spectroscopy and transient-current-technique (TCT)

For the investigation of the detector performance electrical characterization and the measurement of the sample's response to incoming radiation must be done. The simple measurement is the correlation between the applied bias and the current flowing through the electrical circuit with the detector when kept out of radiation path. This way the leakage current is determined. The current can flow through the bulk of the material or on the sample's surface. Marchini *et. al.* [8] found that only a fraction of the current flows through the bulk, most of electrons are transported on the surface. The leakage current should be as low as possible as its greater amount distorts the resolution of the final detector.

The spectroscopic information of the detector's response to incoming radiation is usually measured by irradiating the sample with X-rays/Gamma-rays/ α -particles from calibrated sources. The sources are usually ^{241}Am , ^{60}Co or ^{137}Cs . The absorbed radiation forms electron-hole pairs inside the bulk of the material which are transported in bias applied to the detector. The charge carrier movement generates current pulse on the collecting metal electrode. The amount of the transported carriers is proportional to the energy of detected radiation.

The current pulse is recorded, amplified, shaped and analyzed with a multi-channel analyzer. The current-voltage characteristics were measured with a Keithley 2410 Sourcemeter for bias on a serial $100\ \Omega$ resistor using the

Keithley 6514 Electrometer. The apparatus for the spectroscopic measurement consisted of a charge sensitive preamplifier, shaping amplifier (3 μs shaping time for electrons, 10 μs shaping time for holes) and a multichannel analyzer. The schema for the apparatus is shown in Fig. 3.4. The voltage was supplied by the Iseg SHQ 122M supply.

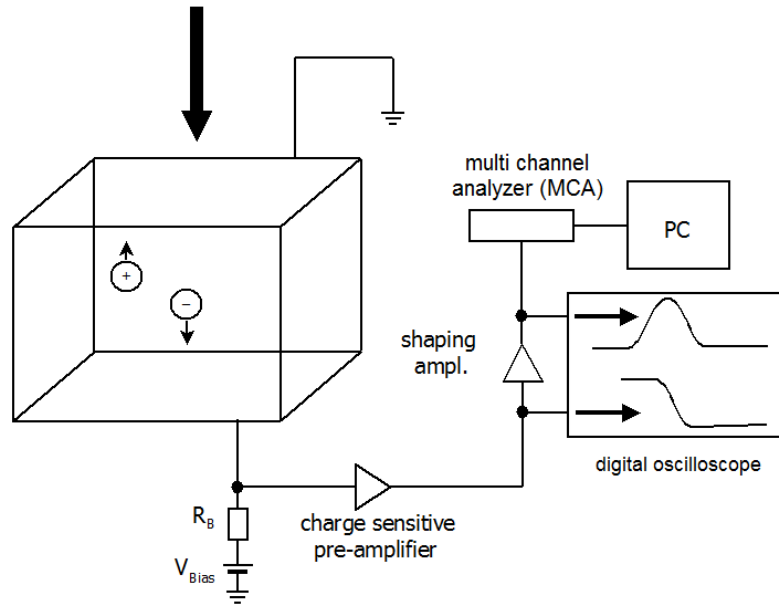


Fig. 3.4 Schema of the spectroscopic detector measurement.

The Transient–Current–Technique (TCT) serves to investigate the charge carrier transport through the detector itself. It measures the current pulses generated by the carrier movement. Vital detector properties including the mobility and the space charge deposited on the deep levels in the material can be obtained. The experimental setup using the α -particle ^{241}Am source is described in detail in [46]. The readout electrical circuit consists of a high frequency bipolar 3–GHz Miteq AM-1607-3000R amplifier with the conversion rate 6.85 mV/ μA . The current signal is recorded by a 4–GHz digital LeCroy oscilloscope and the signal is averaged over 1000 events. The high energy α -particles created a great amount of electron–hole pairs and the influence of the plasma effect of the measurement was visible, hindering a full evaluation of the pulses. Therefore the radiation source was changed to a laser diode with the peak wavelength at 662 nm, which was used in a pulsed–regime with the optical generation of the charge carriers. The modified apparatus should be denoted laser–induced TCT (L–TCT). The electrical schema of the measurement setup is shown in Fig. 3.5.

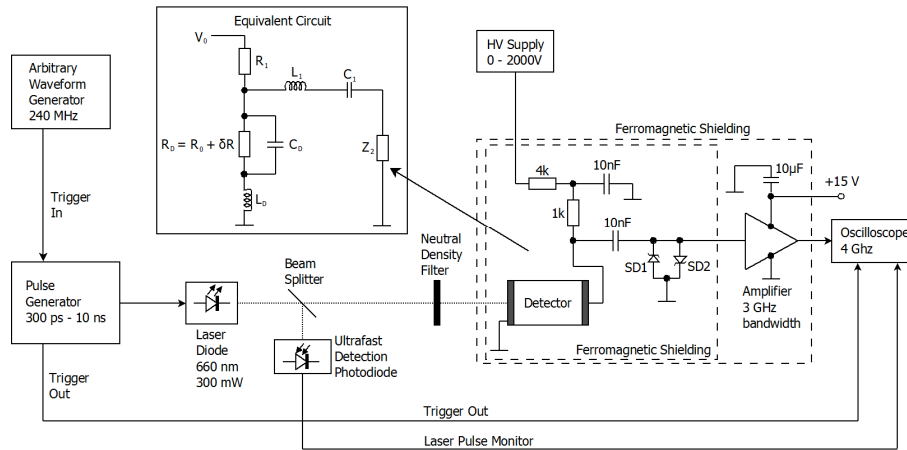


Fig. 3.5 Electrical schema of the L -TCT readout circuit.

3.4. Ellipsometry

Ellipsometry is a non-destructive optical technique, which proved itself as an effective tool for derivation of optical properties of matter and surface layer thickness [47]. It measures changes in light polarization upon reflection on the sample. This polarization change is represented by ellipsometric angles Ψ and Δ , which are related to Fresnel reflection coefficients for s- and p-polarized light by

$$\delta = \frac{r_p}{r_s} = \tan(\Psi) \cdot e^{i\Delta}. \quad (3.5)$$

The measured parameters Ψ and Δ are sensitive to surface conditions, layers thickness and dielectric functions of investigated materials. Therefore, with proper choice of a theoretical model structure one can fit the experimental data and derive spectrally dependent optical properties of investigated material as well as the thickness of the surface oxide layer. A commercial Mueller matrix ellipsometer J.A.Woollam RC2 was used to obtain the experimental data in the light energy range from 1.2 to 4 eV. The results were confronted with the theoretical model and the mean squared error (MSE) was used to evaluate the reliability of the fit.

3.5. Samples

For the investigation several CdTe and CdZnTe samples were used. Some were obtained from various commercial suppliers, some were grown in the Laboratory of crystal growth at the Institute of Physics at Charles University in Prague. The CdTe sample dimensions and parameters are shown in

Table 3.1. The CdZnTe samples used are presented in

Table 3.2.

Sample designation	Dopant	Origin	Resistivity [$\Omega \cdot \text{cm}$]	Dimensions [mm^3]
CT-I	Cl	Commercial	$4 \cdot 10^9$	$4 \times 4 \times 1.5$
CT-II	In	Prague	$9 \cdot 10^8$	$6 \times 6 \times 2$
CT-III			$9 \cdot 10^8$	$6 \times 6 \times 2$
CT-IV	In	Prague	$8 \cdot 10^8$	$7 \times 6.5 \times 2.2$

Table 3.1 CdTe samples used for the investigation.

Sample designation	Zinc content [%]	Dopant	Origin	Resistivity [$\Omega \cdot \text{cm}$]	Dimensions [mm^3]
CZT-I	~10	In	Commercial	$2 \cdot 10^{10}$	$6.4 \times 2.7 \times 2$
CZT-II	~10	In	Commercial	$2 \cdot 10^{10}$	$18 \times 18 \times 2$
CZT-III	~10	In	Commercial	$1 \cdot 10^{10}$	$5 \times 5 \times 2$
CZT-IV	~10	In	Commercial	$2 \cdot 10^{10}$	$7 \times 4 \times 2$
CZT-V	3.5	none	Prague	$2 \cdot 10^9$	$8 \times 5 \times 2$

Table 3.2 CdZnTe samples used for the investigation.

The parameters shown are taken after mechanical polishing of the sample, prior to their further preparation. The values for resistivity are obtained using the contactless resistivity mapping apparatus and average values of each sample is assessed also prior to chemical etching etc. The dopants and the impurities composition were measured with glow-discharge-mass-spectroscopy and are stated where necessary for the evaluation of the measurement results.

Results

4. Deep Level Investigation

4.1. Photoluminescence

In this chapter the attention is fixed on the investigation of deep levels in the spectral range of 0.9 eV up to 1.25 eV using photoluminescence measurements. Both temperature and excitation PL dependences of all deep level components contributing were measured. Excitation by photon energy both above the bandgap and below the bandgap was utilized. Commonly used above-bandgap excitation affects only the surface layer of the sample. Surface (non-radiative) recombination can affect the results. On the other hand, below-bandgap excitation reaches deeper into the bulk of the samples and more information on defects inside the sample can be obtained, including excitation spectroscopy. Some of the results presented in this chapter were published in [48], [49].

4.2. Photoluminescence of CdTe

The investigation was performed on two neighboring indium doped CdTe samples (named in Table 3.1 as CT-II and CT-III) which were cut off from a single crystal grown by the Vertical-Gradient-Freeze (VFG) method. Both samples dimensions were $6 \times 6 \times 2 \text{ mm}^3$. The intentional In-doping level was rather low: $5 \times 10^{15} \text{ cm}^{-3}$ in the charge. The sample was mechanically polished using a $1 \text{ }\mu\text{m}$ alumina (Al_2O_3) abrasive and then etched by immersion into a 3% bromine-methanol (Br-methanol) solution for 2 minutes. Despite of the low dopant concentration, the material is semi-insulating with a resistivity value of $\rho = 9 \times 10^8 \text{ }\Omega \cdot \text{cm}$, Hall electron concentration $n = 10^7 \text{ cm}^{-3}$, calculated Fermi level position $E_F = E_V + 0.861 \text{ eV}$ and electron mobility $\mu = 800 \text{ cm}^2 \cdot \text{V}^{-1} \cdot \text{s}^{-1}$; all values at room temperature. X-ray detectors made from the material were of average quality with mobility-lifetime product of electrons $\mu\tau \approx 5 \times 10^{-4} \text{ cm}^2 \cdot \text{V}^{-1}$. Chemical analysis (glow discharge mass spectroscopy-GDMS) shows a rather high concentration of sulfur (80 ppb), higher than the indium concentration in the sample

(see Table 4.1). One ppb corresponds to concentration $2.94 \times 10^{13} \text{ cm}^{-3}$. Rather a low concentration of shallow acceptors was found (Li, Na, P if incorporated as substituents, but donors if in interstitial positions). Aluminum should create shallow donor levels similar to In. Zn and S are isoelectronic impurities (both $\text{Zn}_x\text{Cd}_{1-x}\text{Te}$ and $\text{CdTe}_{1-x}\text{S}_x$ are ternary crystals), Cu and Ag are usually “deeper” acceptors. Fe, Sn, Sb have been reported to be connected with deep levels. Sample CT-III was studied through PL temperature dependence with excitation energy above the bandgap (chapter 4.2.2), all other investigation was performed on sample CT-II.

Element	Conc. [ppb]	Element	Conc. [ppb]
Li	< 1.1	Fe	< 25
B	< 5	Cu	7
Na	1	Zn	8
Al	12	Ag	< 15
Si	< 5	In	< 20
P	2	Sn	< 20
S	80	Sb	< 15

Table 4.1 *The most abundant impurities of CdTe-III sample as determined by GDMS.*

4.2.1. Excitation above the bandgap, $\hbar\omega_{EXCIT} > E_G$

The studied sample exhibits typical structures for CdTe doped with indium usually observed in the luminescence spectra with above-bandgap excitation, see Fig. 4.1 and Table 4.1. The luminescence bands marked as 1 – 6 and 8 are accompanied by their well-recognized optical phonon replicas. Dominant peak 4 is the so called C-line at 1.584 eV. The "1.45 eV" band is not single; at least two components can be distinguished. The well-resolved free and bound exciton recombination spectra are commonly attributed to samples of good crystalline quality. On the other hand, detection of a Y-line shows significant effect of lattice

deformation (dislocations) and rather manifold spectra of deep levels indicate the presence of various types of defects.

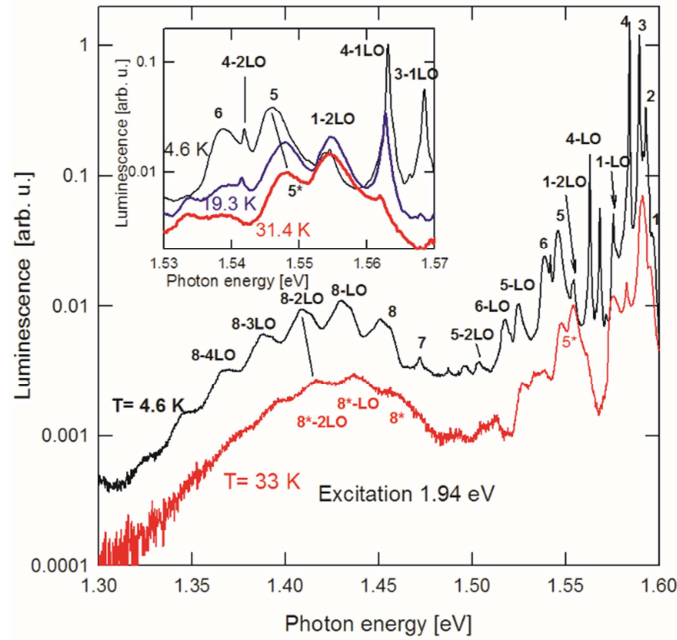


Fig. 4.1 Luminescence spectra in the range of exciton recombination (1,2,3,4), donor–shallow acceptor recombination (5,6), dislocation–bound exciton recombination (7) and recombination at A-centers / deeper acceptors (8). Changes in the spectral region of shallow acceptors recombination with increasing temperature are outlined in the inset.

Photoluminescence at lower photon energies as detected by the InSb detector is shown in Fig. 4.2. A broad band around 1.1 eV is dominant in the deep level spectra. The components of the "1.1 eV" PL band marked as 9, 10 and 11 are examined in more detail in the following parts of the chapter. The intensity of band 12 (0.9 eV) is highly influenced by a surface damage and will be investigated in chapter 6.3 of this thesis. Throughout the current chapter will be proven that the decomposition is necessary for the explanation of excitation spectroscopy and temperature dependence of the observed spectra.

	Position at 4K [eV]	Assignment
1	1.596	FE; dip due to reabsorption by free excitons / excitonic polaritons
2	1.593	(D ⁰ ,X); recombination of excitons bound to neutral donors
3	1.589	(A ⁰ ,X); recombination of excitons bound to neutral acceptors
4	1.584	C–line; recombination of excitons bound to complex defects containing In
5	1.546	DAP–like; recombination in pairs donor–acceptor complex containing cadmium vacancy; and/or isoelectronic impurity (like oxygen and/or possibly sulphur)
6	1.539	DAP; recombination in donor – acceptor pairs, substitution possibly Na _{Cd}
7	1.472	Y–line; recombination of excitons at specific type of dislocations
8	1.451	DAP recombination in pairs donor–deeper acceptors A centers (Cd vacancy + In donor) and Cu acceptors
	1.458	(e,A ⁰) recombination observed at 30 K
9	1.19	?
10	1.13	?
11	1.03	?
12	≤0.9	?
13	0.64	?
14	<0.55	?

Table 4.2 Luminescence bands observed in CdTe doped with In at 4 K. See [49] for references.

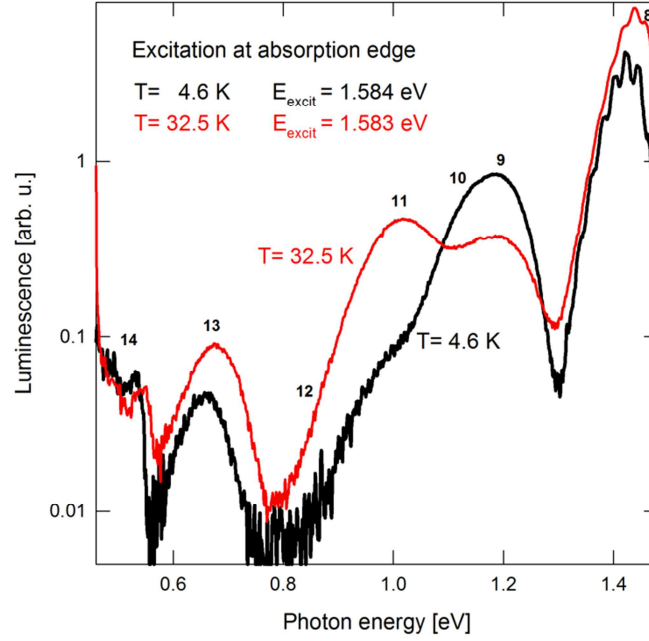


Fig. 4.2 PL spectra recorded by InSb detector with excitation at the absorption edge.

4.2.2. Temperature dependence with excitation above bandgap

At first the sample will be investigated with the excitation laser energy above the bandgap of the material, $\hbar\omega_{EXCIT} > E_G$.

The excitonic bands (1 – 4) are shifted to lower energies with increased temperature; the shift is given by the temperature dependence of the bandgap $E_G(T)$ [3]. The intensity of bound exciton recombination decreases monotonically with the increasing temperature; band 3 (A^0, X) diminishes at the highest rate. Free exciton (FE) structure 1 weakens slowly. The replica of FE (FE – 2LO) even reaches its maximum at 20 K, as can be seen in the inset in Fig. 4.1. The recombination in donor–acceptor pairs (DAP) is a natural behavior of bands 5, 6 and 8:



and it is transformed to recombination of a conduction electron with an acceptor (e, A^0):



The corresponding peaks are shifted to higher energies with temperature increase up to 30 K, as indicated by shift 5→5* in the inset in Fig. 4.1 and by a more pronounced shift of band 8.

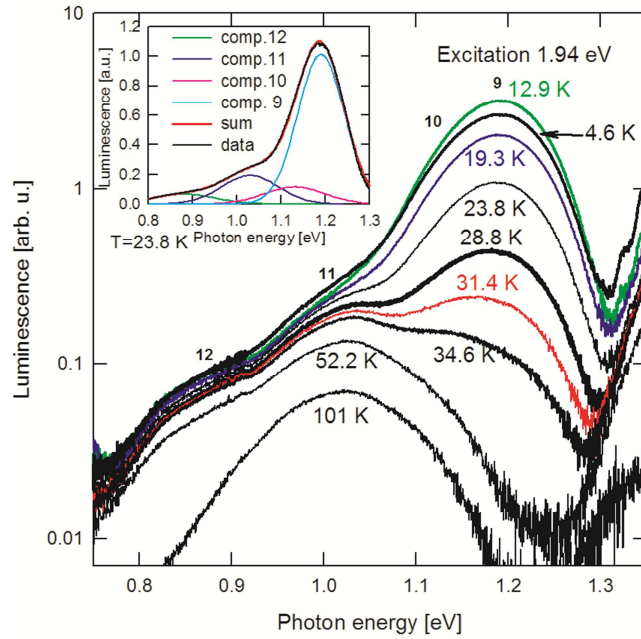


Fig. 4.3 PL spectra recorded by the Ge LN detector with above-bandgap excitation. Decomposition of the spectrum at 24 K is presented in the inset.

PL spectra in the region of the “1.1 eV” band are depicted in Fig. 4.3 for several temperatures. Spectral position of bare PL maxima at various types of excitation (including the $\hbar\omega_{EXCIT} > E_G$ excitation) in dependence on temperature are shown in Fig. 4.4. The shift of the PL maxima can be explained just by different temperature dependences of separate components intensities. The spectra presented in Fig. 4.3 can be decomposed by fitting procedures into four Gaussian bands, see inset in Fig. 4.3.

The intensities of both components 9 and 10 reach their maxima near 13 K. It resembles the temperature dependence of the free exciton replica. This can be

explained by a thermal escape of carriers from shallow levels supplying the radiative recombination channels with non-equilibrium carriers. Investigating the spectra at temperatures above 30 K, it becomes visible that peak component 11 is less quenched than components 9 and 10 and can be regarded as an independent band. Both components 9 and 10 are thermally quenched quite rapidly; they become very weak above 30 K. On the contrary, the intensity of the “1.4 eV” band decreases monotonically with increasing temperature under $\hbar\omega_{EXCIT} > E_G$ excitation.

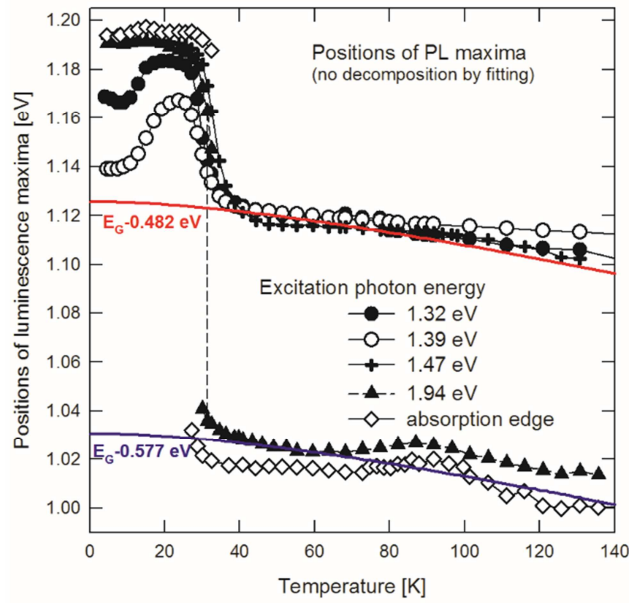


Fig. 4.4 Position of the luminescence maxima in the spectral range 1.0 – 1.2 eV versus temperature for several exciting photon energies. Temperature dependence of $E_G - 0.482$ eV and $E_G - 0.577$ eV are plotted as well.

4.2.3. Excitation spectroscopy at 4.6 K

Using the tunable Ti:Sapphire laser, the excitation spectroscopy with the incident photon energy below the bandgap ($\hbar\omega_{EXCIT} < E_G$) was measured at a fixed temperature of 4.6 K.

At excitation well below the absorption edge, the intensity of luminescence rapidly decreases with the drop of exciting photon energy due to the fall of the amount of absorbed light. The forms of the spectra are changed as well. Very different characteristics for components 9 and 10 are revealed contrary to excitation at absorption edge and at higher excitation energies. The components 9

and 10 become well-distinguishable at excitation below 1.5 eV. In various ranges of the excitation photon energy, one of the two independent bands dominates as can be seen in Fig. 4.5, where the positions of the bare PL maxima are depicted as a dependence on the exciting photon energy. Component 10 (PL near 1.13 eV) becomes stronger in a rather narrow interval of excitation photon energies 1.34 eV – 1.42 eV, whereas component 9 (PL near 1.19 eV) prevails outside of this interval as shown in Fig. 4.6, where results of fitting decomposition of the spectra are shown. A noteworthy threshold for components 9 and 10 at 1.45 eV coincides with ionization energy of “deeper” acceptors like A-centers or Cu impurity.

4.2.1. Temperature dependence with excitation below bandgap,

$$\hbar\omega_{EXCIT} < E_G$$

The final investigation of this material was the temperature dependence of PL signal with the excitation laser energy below the bandgap, $\hbar\omega_{EXCIT} < E_G$.

The shapes of the PL spectra are changed with temperature (see Fig. 4.7 for $\hbar\omega_{EXCIT} = 1.39$ eV). Component 10 is dominant at a low temperature, then contribution of component 9 reaches its maximum at 20 K and a rapid fall down of intensity of component 9 comes with temperature increased. This is demonstrated also by a shift of the luminescence maxima displayed in Fig. 4.4 where spectral positions of the measured PL maxima (no decomposition) are shown in dependence on temperature and excitation photon energy. In the case of excitation at the absorption edge and at higher photon energies, the “1.4 eV” band (not shown in Fig. 4.4) and component 11 of the 1.1 eV band are dominant above 30 K, whereas the excitation $\hbar\omega_{EXCIT} < E_G$ induces component 10 as the main contribution above 40 K. Results of fitting procedures for excitation photon energies 1.32 eV and 1.39 eV are shown in Fig. 4.8.

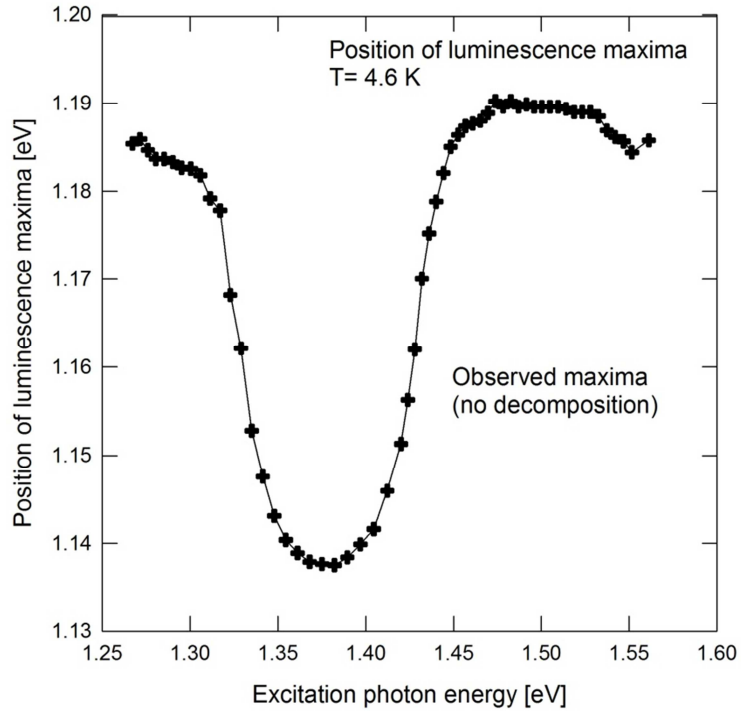


Fig. 4.5 Position of the bare luminescence maxima (in the spectral range of components 9 and 10) versus exciting photon energy at 4.6 K.

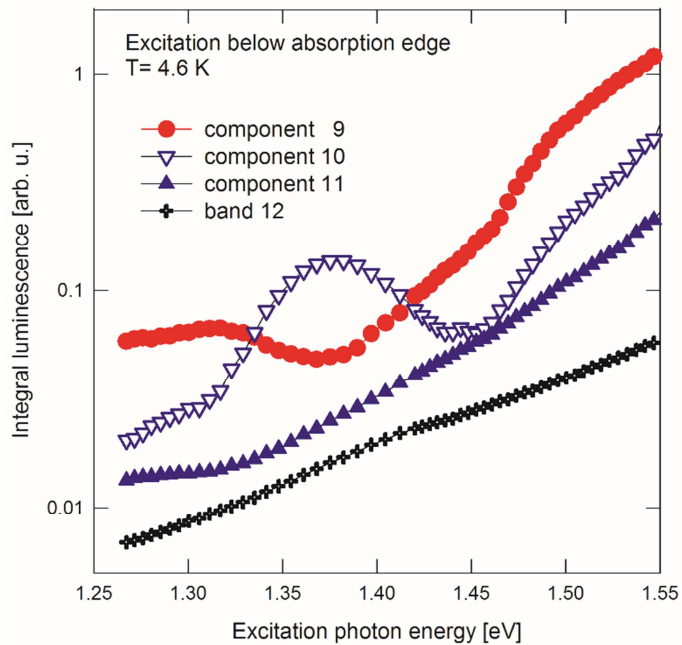


Fig. 4.6 PL excitation spectra – contributions of components 9, 10, 11 and 12 to the luminescence at 4.6 K obtained by fitting procedures.

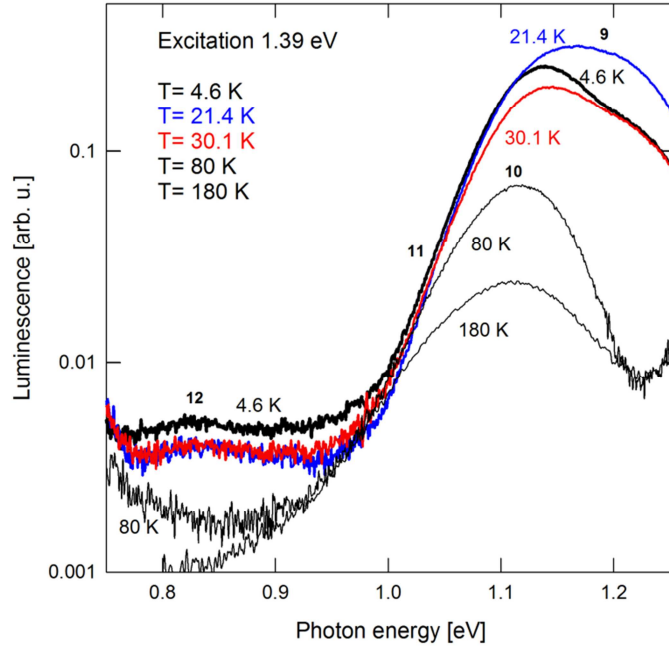


Fig. 4.7 Luminescence spectra excited at 1.39 eV.

Moreover, the thermal activation of component 10 becomes apparent with excitation $1.32 \text{ eV} < \hbar\omega_{EXCIT,MAX} \approx 1.38 \text{ eV}$ in the case of insufficient exciting photon energy to reach the maximal PL of component 10, i.e. below 1.36 eV. No such effect appears at higher excitation photon energy. Activation energy roughly estimated for very narrow interval at 24 K is 40 meV.

4.2.1. Spectral position of PL peaks and PLE spectra

It is widely accepted that PL bands are composed of phonon replicas of zero phonon lines (ZPL). The replicas are well-distinguished in the case of recombination in donor-acceptor pairs with shallow acceptors (spectral range at 1.5 eV) and in the “1.4 eV” band (at least in crystals of sufficient quality at low temperatures), see Fig. 1. The PL intensity of the respective replicas is given by the Poisson distribution with the Huang-Rhys factor S being a parameter characterizing the electron-phonon interaction.

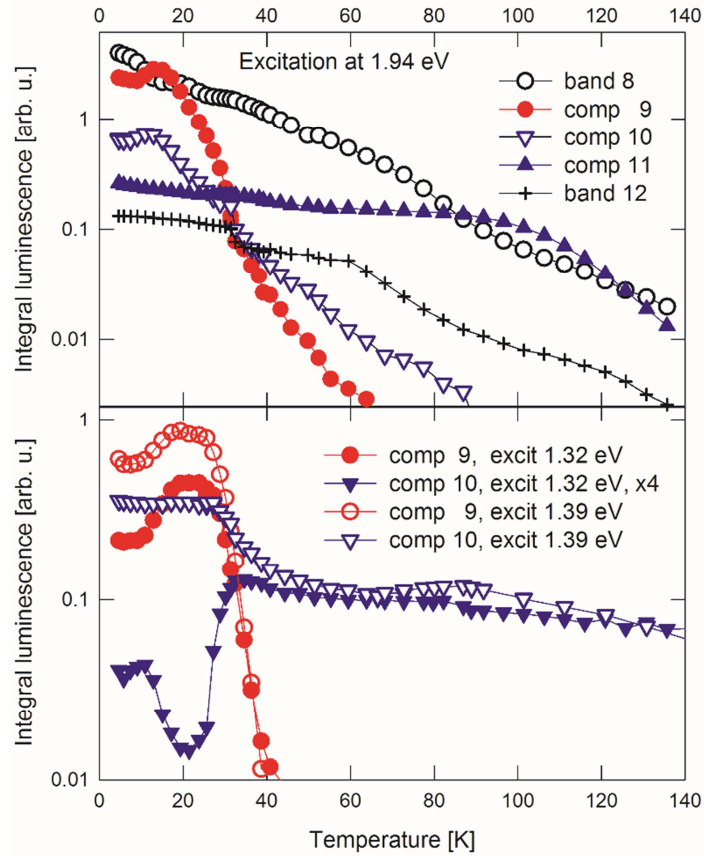


Fig. 4.8 Temperature dependence of fitted intensities of the respective components of the luminescence excited at 1.94 eV, 1.39 eV and 1.32 eV. Component 10 at excitation 1.32 eV is four times amplified.

It is expected that the electron–phonon interaction is stronger for deep, well–localized states of defects. Thus ZPL energy can be remarkably different from the peak of the PL band. Usually no replica structure is observed for deep defect levels including the “1.1 eV” band. No band with replica pattern was reported in published papers on CdTe in this spectral range. Therefore, the S parameter (needed for the estimation of the difference between the position of the PL peak and ZPL) cannot be determined directly. An important parameter is the width of PL bands. However, there are some other contributions leading to band broadening like fluctuations of structure and potential in the locality of the defect.

No phonon replicas were resolved for components 9 – 12.

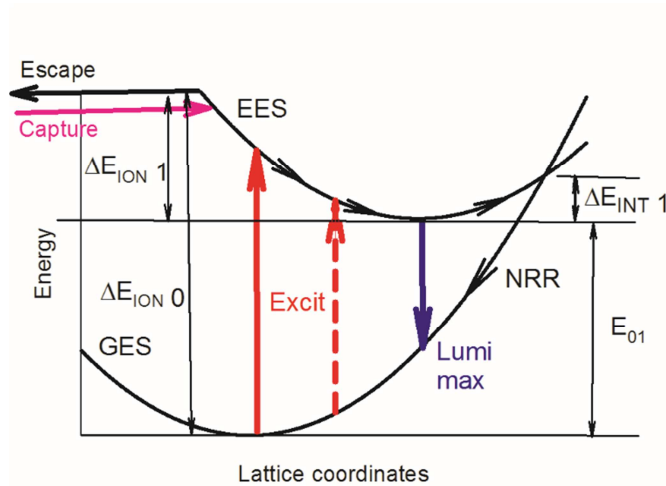


Fig. 4.9 One of the possible modifications of the schema energy diagram of the simplest model of a localized center with two localized electron states (ground GES and excited EES). A relaxation of atomic arrangement comes after the optical excitation (red arrow) and the peak of the PL band is represented by the blue downward arrow. NRR stands for non-radiative relaxation. E_{01} represents the difference between the excited electronic state and the ground electronic state, both in the case of relaxed atomic arrangement. $\Delta E_{INT 1}$ indicates activation energy (height of a barrier) for internal thermal PL quenching. The red dashed arrow shows the excitation possible at a higher temperature when even lower photon energy can excite the electronic state. The Escape and Capture arrows symbolize the possibilities of charge changes of the center.

The simplest energy diagram for both the excited and the ground state in photoluminescence phenomena is shown in Fig. 4.9. It uses the Franck-Condon principle (vertical arrows represent optical transitions with no phonon emission or absorption). The diagram is drawn for exciting photon energy lower than ionization energy of the ground state $\Delta E_{ION 0}$. The optical excitation is indicated by the red upward arrow (in principle this energy should be observable in excitation spectra PLE). Then a relaxation of atomic positions to a new equilibrium position happens. A radiative emission is drawn as the blue downward arrow and it corresponds to the PL peak. The energy of the zero-phonon line (ZPL) can be approximately identified with the energy difference between the excited and ground states of a defect in equilibrium (E_{01} in Fig. 4.9). As one can see in this simple model, the probable value for E_{01} is located in the interval between the PL peak and the PLE band.

By increasing the excitation photon energy a regime of center ionization is realized (bound-to-band transition). This means that:

- either the system of energy levels is changed and the center falls out of this absorption/emission channel,
- or a charge recapture happens and a relaxation either by a radiative or non-radiative process takes place.

Of course, a close link of PL and PLE is then broken. Whereas a relatively narrow excitation band is expected for an inner excitation of defect states, a threshold of excitation spectra for the ionization of deep levels is expected near the energy difference between the defect and bottom (top) of the CB (VB). The maximum of the absorption is expected at much higher photon energy. In an oversimplified model of photoionization by Lucovsky [50] (the case of extremely localized deep level state), the maximum would appear at $\hbar\omega_{EXCIT, MAX} \approx 2 E_{IONIZ}$. Such a maximum in the PLE spectra is overridden by much more intensive interband absorption.

The below-gap excitation produces a low excitation in the bulk of the sample (because of the low absorption coefficient) and processes like internal excitation inside defects or ionization of defect states (e.g. $A^- + h\nu \rightarrow A^0 + e^-$ for acceptor) or both can dominate. Therefore, the PLE local maximum observed for component 10 in Fig. 4.6 is a strong argument for the opinion that the PL component 10 is caused by an internal transition (bound-to-bound).

Finally, the mostly used experimental implementation is band-to-band excitation $\hbar\omega_{EXCIT} > E_G$. A simple version of processes in a donor-acceptor pair at above-gap excitation is outlined illustratively in Fig.1 in [51] where repeated captures/escapes of the charge are taken into account as well as internal PL emission and relaxation. Generally for bulk crystals with a commonly treated surface, the excitation spectra reach their maxima in the spectral region of the absorption edge (Urbach tail); then sharp structures due to absorption/reflection spectra of excitons are observed. The PLE spectra in the region of higher $\hbar\omega_{EXCIT}$ are not very spectrally dependent and PL is reduced because of surface non-radiative recombination.

4.2.2. Temperature and excitation dependence of PL peaks

As stated in the beginning of this chapter, the absolute majority of PL measurements is carried out at above-bandgap excitation, where generation of electron-hole pairs in the respective bands (CB, VB) is dominant. A non-equilibrium population of defect states with energy levels in the energy gap is created by a capture of the electrons and holes. With increasing temperature, a PL intensity decrease (thermal quenching) appears. Two main limit mechanisms can be distinguished:

1. The quenching is caused by the thermal excitation of an electron (hole) bound to the defect that enables to overcome a potential barrier $\Delta E_{INT 1}$ given by the dependence of total energies of the excited and ground states on atomic space arrangement as shown in Fig. 4.9. This mechanism is also possible in the case of above-gap excitation; see Fig 1b in [51]. The carriers in VB/CB are captured in a defect state and then they can recombine non-radiatively by breaking the barrier $\Delta E_{INT 1}$. A multiple phonon emission assists the relaxation/recombination. Because this process can proceed in one defect, this mechanism is reported as the “one-center model” or “internal recombination model” (the schema proposed by Seitz and Mott).
2. The quenching is due to a thermal escape of the carriers from the defect state back to the energy bands, e.g. escape of a hole from acceptor $A^0 \rightarrow A^- + h$. The escaped carriers can be captured by other defects where a recombination (non-radiative or radiative) proceeds. The carriers in CB/VB constitute a common reservoir for various recombination channels and a competition of individual channels comes into play. This is sometimes associated with the effect when thermal quenching of a PL band is accompanied with an increase of PL in another band. This can result in a non-monotonic temperature dependence of PL intensity: a thermal activation of the intensity at low temperatures in the latter band turns into the thermal quenching at higher temperatures. This type of the quenching mechanism is called the “multi-center model” or the Schön-Klasens mechanism [51].

Temperature dependence of PL in an acceptor band using a three-level model (one shallow donor, one acceptor and one non-radiative recombination center near the middle of the bandgap) under above-gap excitation was extensively discussed by Reshchikov [51] for wide-gap semiconductors and for various assumptions on the ionization energies of donors and acceptors, their concentrations, capture coefficients of the carriers and generation rates of electron-hole pairs. The “multi-center model” results in a great variety of PL temperature dependences: some of the dependence corresponds to an ingenious concept that “activation energy” of the quenching should be equal to the ionization energy. However, sometimes very different behavior (much lower “activation energy” for the thermal quenching) can be obtained, particularly when the concentration and/or capture coefficients for the middle-gap recombination center are high compared to the values for the donors and acceptors. This is the case of high resistivity samples with Fermi level near the middle of the bandgap and a result of the above mentioned common reservoir of carriers for various recombination processes.

A possible schema of some basic processes in the studied sample is drawn in Fig. 4.10. The luminescence transitions are supposed to be connected with electrons in the CB or with electrons bound to states near the CB bottom. A similar chart can be sketched for holes at the VB top as indicated for #9. The evaluation assumes that bands 8 – 11 are independent, i.e. that they are created by different defects/impurities. Of course, the population of band states and localized states is given by the competition of radiative and non-radiative recombination channels and by the capture and escape of electrons (holes) from traps.

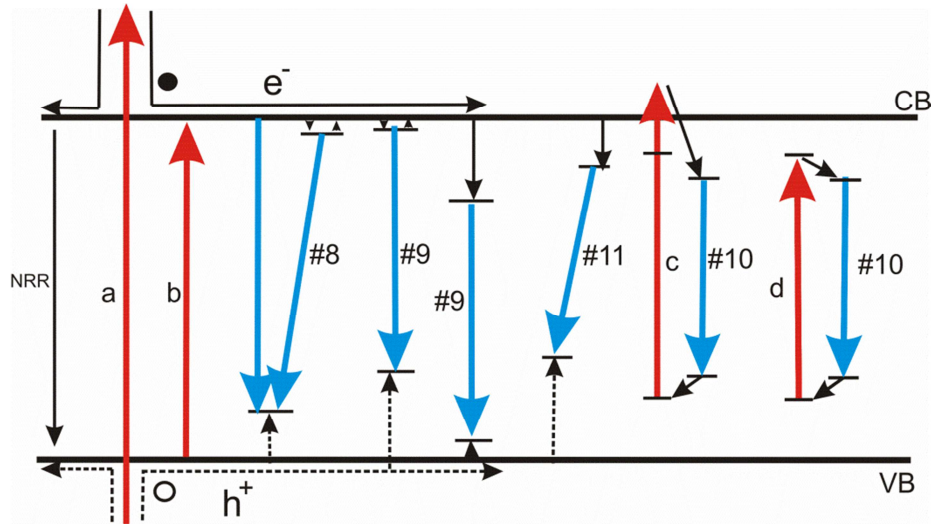


Fig. 4.10 Some of possible processes: a) excitation $\hbar\omega_{EXCIT} > E_G$; b) excitation at absorption edge; c) excitation $\hbar\omega_{EXCIT} < E_G$, ionization of the deep level; d) internal excitation of component 10. Black arrows outline charge carriers relaxation and transport including capture; NRR symbolizes non-radiative recombination. Inclined arrows #8 and #11 indicate possible DAP transitions.

4.2.3. Comments on the individual PL components

Component 9

Components 9 and 10 are not well-resolved at $\hbar\omega_{EXCIT} > E_G$ and their joint band dominates at temperatures below 30 K. On the contrary, the components can be well distinguished at the excitation $\hbar\omega_{EXCIT} < E_G$ (Fig. 4.5, Fig. 4.6, Fig. 4.7). This encouraged us to decompose components 9 and 10 by a fitting procedure, see inset in Fig. 4.3.

Properties of the component 9 with the band 8 can be compared. It is commonly accepted that band 8 (“1.4 eV band”) is caused by a recombination in shallow donor–deeper acceptor pairs at low temperatures and by a recombination of an electron in CB with a hole localized at the acceptor at higher temperatures. The position of the PL maximum is associated with this modification; a shift of several meV is observed (7 meV for our sample). On the contrary, no shift of several meV to a higher energy was recognized in component 9 with increasing temperature. At above-bandgap excitation, thermal quenching of the PL intensity of component 9 is much faster than that of the whole band 8 (together both the DAP

and (e, A^0) recombination, see Fig. 4.8). The temperature dependence of the PL intensity of component 9 could resemble rather only the component DAP of band 8 (that is effectively quenched above 20 K) than a sum $DAP + (e, A^0)$.

Thus component 9 can be caused by the transition from an excited state that is activated by carrier capture. Following the schema given in Fig. 1 in [51], two competitive quenching mechanisms described above and denoted as 4 and 5 in the figure can occur.

1. Escape of the carrier to the CB follows the excitation, i.e. the excited state is very effectively thermally depopulated at temperatures above 20 K. Either a shallow “one–electron” trap state with a level near the CB bottom (VB top) or a metastable state (including a possibility of the so called “negative–U centre”) should be taken into consideration.
2. Or there is a very low energy barrier for non–radiative recombination inside the center resulting in an effective thermal quenching over the potential barrier.

Of course, both mechanisms can be combined. Taking into account that the steep quenching of component 9 is accompanied by noticeable changes in other PL components (see Fig. 4.8), the possibility of an intensive exchange of the charges with the CB (or VB) is most likely.

A threshold in PLE spectrum near 1.45 eV is recognizable in Fig. 4.6. It is the energy where ionization of deeper acceptors (A–centers, Cu impurities) can make the concentration of carriers in bands higher. It is possible that defects connected with PL component 9 capture the electrons preferentially, giving raise to excited states of the defect very near the CB bottom. Thermal depopulation of the excited state with increasing temperature causes the rapid PL decrease.

Component 10

The dependence of the PL maxima positions (Fig. 4.5) and results of the PL spectra decomposition procedures (Fig. 4.6) on excitation photon energy can be explained using the simplest model with a strong electron–phonon interaction (at least at low photon excitation energy, process **d** in Fig. 4.10), schema depicted in Fig. 4.9. No charge transfer between the CB or the VB and the defect center may be

assumed. Thus the excitation in the localized center can be dominant for $\hbar\omega_{EXCIT} < 1.45$ eV, while excitation at $\hbar\omega_{EXCIT} > 1.45$ eV can cause photoionization (process **c** in Fig. 4.10). The photoionization is followed by a capture of carriers into the excited state of the center and then PL emission in component 10 appears.

Assuming:

- 1) main broadening of the PL band is given by the phonon emission mechanism;
- 2) the peak position for absorption (PL excitation) at 1.38 eV follows the symmetry rule concerning Stokes – anti–Stokes transitions;
- 3) both excitation and emission processes involve the same ground and excited electron states, but in changing atomic arrangement.

The ZPL position can then be estimated to be at 1.26 eV, i.e. the difference

$$E_{ZPL} - \hbar\omega_{PEAK} \approx 6 \times \hbar\omega_{LO}.$$

In Fig. 4.8 a striking difference between temperature dependences of the intensity of component 10 measured at excitation near the maximum of the PLE spectra ($\hbar\omega_{EXCIT} = 1.39$ eV) and measured below the maximum (1.32 eV) is visible. It is possible to explain the difference by a thermal activation of the ground state; see the dashed upward arrow in the energy schema of a localized center in Fig. 4.9. The thermal energy supplies a contribution to the lacking optical excitation energy. The activation energy 40 meV for the PL growth near 24 K at excitation of 1.32 eV was determined from the steepness of the temperature dependence. It is in a reasonable agreement with the difference 70 meV of the two excitations (considering the simultaneous thermal quenching).

Component 10 is dominant at higher temperatures under below–bandgap excitation when a concentration of non–equilibrium carriers in the CB and VB is low. The excited state of the related defects changes the charge with much lower probability than component 9. Component 10 wins a competition for charge carriers under the condition of low optical generation rate at higher temperatures; the excited state is deeper than that of component 9.

Component 11

Unlike components 9 and 10, component 11 can be observed up to relatively high temperatures under near- and above-bandgap excitation when carriers in both energy bands (VB and CB) are generated with a high concentration (in comparison with below-bandgap excitation). Component 11 could be attributed to an effective recombination center. Relatively high concentration of both electrons and holes seems to be the condition for dominance of this mechanism.

4.2.4. PL quenching activation energies

The activation energy of thermal quenching is assumed to be the ionization energy in an oversimplified concept. Both experimental results and model calculations [51] show that this is not correct, particularly for high resistivity samples. This inconsistency can be a source of differences between results various measurements (e.g. PL, PICTS, etc.).

The temperature dependences of the integrated PL intensity are complex. Spectra fitting using a simple model based on the assumption of Gaussian-like peaks is doubtful and questionable. It should be noted that the problem of spectra evaluation and the zero-phonon-line (ZPL) is usually simply “solved” by a choice $\hbar\omega_{\text{PEAK}} = \hbar\omega_{\text{ZPL}}$. The “activation energies” of quenching deduced from short temperature intervals at relatively high temperatures are summarized in

Table 4.3. Only data obtained for above-bandgap excitation were usable. Assuming that the luminescence would be caused by band-to-bound transitions and the quenching would be caused by a thermal escape of electrons (holes) into CB (VB), the values near either $\hbar\omega_{\text{ZPL}}$ or rather at $E_G - \hbar\omega_{\text{ZPL}}$ should be obtained according to a simple estimation. However, much lower values have been received. As mentioned above, if a high-rate recombination (possibly non-radiative) in materials with Fermi level near the middle of the bandgap is taken into account (as in [51]), much lower “activation energy” can be obtained than the one corresponding to ionization energy of the center for radiative recombination. Another possibility is a quenching caused by overcoming a barrier either inside the defect (like in Fig. 4.9) or more probably

in the case of high concentration of various defects by breaking barriers between neighboring defects. However, similar values of “activation energy” have been received for various components; and an interlink between temperature dependences of the respective components is obvious. Thus the above mentioned “multicenter–model” is preferred for the evaluation.

Component	Temperature range [K]	Activation energy [meV]	$\hbar\omega_{PEAK}$ [eV]	FWHM [eV]	$\hbar\omega_{ZPL}$ [eV]
8	71–115	73	1.43	0.075	1.45±0.001
	120–145	77			
9	36–60	68	1.19	0.125	1.27±0.04
10	50–80	68	1.13	0.162	1.26±0.01
11	125–145	95	1.03	0.154	1.14±0.08
12	60–125	70	0.83	0.172	1.0±0.1
	125–145	78			

Table 4.3 Activation energies deduced from PL thermal quenching at relatively high temperatures at above–gap excitation compared to estimated ZPL energies at 4 K (published in [48]). The values 1.430 and 1.450 are for the stronger component of the band 8.

4.2.5. Comparison to results in other papers

The same sample and its deep level structure was studied using the electro–optical Pockels effect and the results were published in [52]. Through spectroscopic measurement, deep levels responsible for the electrical polarization and depolarization of the sample were found. The position of the levels was $E_C - 1.09$ eV, $E_C - 0.84$ eV and $E_C - 0.69$ eV, which could correspond to band 10/band 11, band 12 and band 13, respectively. There seems to be only a single peak in the spectral range of 1.1 eV, but the resolution of the Pockels measurement is much more limited than PL investigation. However, as it has been states in the previous chapters, the agreement of the position of deep levels found through different methods is not sufficient for the conclusion of the deep levels being

of the same origin. The paper [52] investigates the deep levels acting in the electrical performance of the detector at room-temperature. The measurement in this thesis studies the complex behavior of the deep levels at low temperatures and is in no way connected to electrical measurements.

In some papers, the “1.1 eV” band was decomposed into two components, typically one with a maximum in the interval $1.1 \text{ eV} < \hbar\omega_{LUMI} < 1.15 \text{ eV}$ and the second maximum at $1.0 \text{ eV} < \hbar\omega_{LUMI} < 1.1 \text{ eV}$. The two components are reported to reveal different characteristics: different activation energies of thermal quenching, distinct dependences of the two components on the excitation power [29], various time constants at chopped excitation [53].

Stadler *et al.* [27] observed several components of the “1.1 eV” band in various samples: 1.145 eV, 1.135 eV, 1.11 eV, 1.05 eV and no correlation with In-doping was found. It was also found that the latter type of the PL band (“1.135 eV”) reveals a shift to higher energies with increasing temperature in some samples [27]. They interpreted it as internal recombination (both excited and ground levels are deep). In the current CdTe measurement, no component revealing such a shift was recognized. The published FWHM $\approx 127 \text{ meV}$ at low temperature is very similar to values obtained in this study.

PL spectra with maxima above 1.15 eV (as component 9) are reported relatively seldom: 1.2 eV in In-doped CdTe after Xe ion implantation [54]; 1.17 eV in some unspecified samples [27], [55]; 1.18 eV after annealing of nominally undoped material in an inert atmosphere. A strongly asymmetric band with a maximum at 1.17 eV was observed for the bulk crystal after mechanical polishing and chemical etching [56]. A dependence of the PL peak position on resistivity in semi-insulating CdMnTe:In was noticed in [24]: the peak is shifted from 1.05 eV for samples with RT resistivity above $10^{10} \Omega\cdot\text{cm}$ up to 1.21 eV for samples with resistivity below $10^8 \Omega\cdot\text{cm}$. No correlations of the peak position to Mn content or In concentration was reported. It should be noted again that the PL peak at 1.19 eV was obtained for the studied sample with resistivity of almost $10^9 \Omega\cdot\text{cm}$.

Only little information in published papers on temperature dependence of the intensity of the PL “1.1 eV” band is to be found.

The value of activation energy gained for the studied high-resistivity sample is significantly lower than in published literature [27], [29], [57], [58]: 73 meV and 77 meV, i.e. about $\frac{1}{2}$ of the acceptor ionization energy. It is in a qualitative

agreement with the results of the Reshchikov [51] models: the quenching activation energy could be approximately equal to the acceptor ionization energy for a conductive n-type material with Fermi level near the CB bottom.

Considering these results for the “1.45 eV” band, one cannot be surprised that a great discrepancy between the quenching activation energy and expected ionization energies is observed for components of the “1.1 eV” band as well, see

Table

4.3

(if mechanism of radiative band-to-bound recombination is assumed).

4.3. Photoluminescence of CdZnTe

For the comparison and deep level investigation of CdZnTe material, two neighboring samples CZT-I and CZT-II were investigated. Both samples were indium doped.

For measurement the samples were mechanically polished using a 1 μm alumina (Al_2O_3) abrasive and then etched by immersion into a 3% Br-methanol solution for 2 minutes, same as with the CdTe samples described in the previous chapters. The material is semi-insulating with a resistivity value of $\rho \sim 2 \cdot 10^{10} \Omega \cdot \text{cm}$, calculated Fermi level position $E_F = E_V + 0.851 \text{ eV}$ and electron mobility $\mu \sim 950 \text{ cm}^2 \cdot \text{V}^{-1} \cdot \text{s}^{-1}$; all values at room temperature. X-ray detectors made from the material were of good quality with mobility-lifetime product of electrons $\mu\tau \approx 1 \times 10^{-3} \text{ cm}^2 \cdot \text{V}^{-1}$. Chemical analysis (glow discharge mass spectroscopy-GDMS) shows a rather high concentration of sulfur (210 ppb), 1 ppb corresponds to concentration $2.94 \times 10^{13} \text{ cm}^{-3}$. As with the CdTe samples, a rather low concentration of shallow acceptors was found, see

Table

4.4.

Both

samples

were

mapped

and photoluminescence was further used in comparison with other methods, see chapter 5.1.

The studied samples exhibits typical structures for CdZnTe doped with indium usually observed in the luminescence spectra with above-bandgap excitation, see Fig. 4.11 and

Table

4.5.

The measured spectra show less bands compared to CdTe measurement. Free exciton is not visible in our studied samples. On the other hand,

well-recognized peaks for donor-bound exciton and C-line and its optical phonon replicas are visible. The "1.45 eV" band, so-called A-center is one broad peak. No ZPL and phonon replicas (on contrary to CdTe) are visible, which is in agreement with published literature. The rise in PL signal in the region around 1.52 eV could indicate the presence of defect causing the Y-line peak in CdTe, as its position is reaching the value of about 135 meV below the bandgap, same as in CdTe.

Element	Conc. [ppb]	Element	Conc. [ppb]
Li	< 2	Fe	< 20
B	13	Cu	< 10
Na	< 2	In	2000
Al	33	Ag	< 30
Si	20	Cl	8
P	1	Sn	< 15
S	210	Sb	< 15

Table 4.4 The most abundant impurities of CZT-II sample as determined by GDMS.

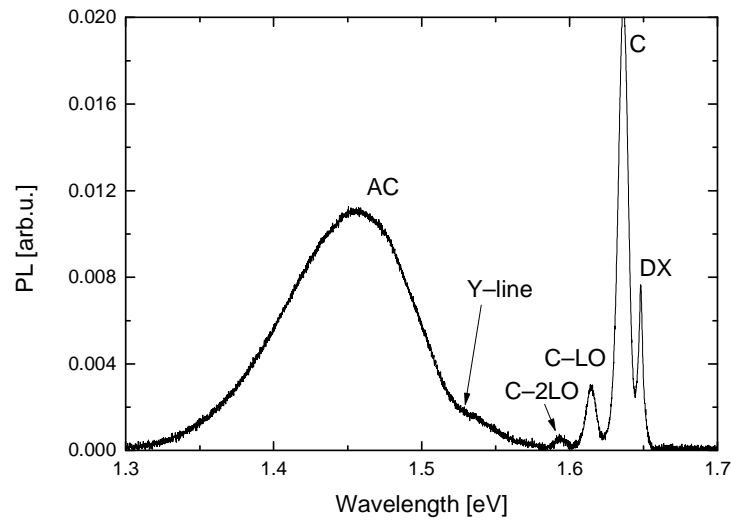


Fig. 4.11 Typical photoluminescence spectrum of CZT-I measured with Si detector at temperature 4.7 K. Incident photon energy 1.94 eV.

	Position at 4K [eV]	Assignment
1	1.648	(D ⁰ ,X); recombination of excitons bound to neutral donors
2	1.637	C-line; recombination of excitons bound to complex defects containing In
3	1.526	Y-line; recombination of excitons at specific type of dislocations
4	1.457	DAP recombination in pairs donor-deeper acceptors A-centers (Cd vacancy + In donor) and Cu acceptors
5	~1.1	?

Table 4.5 Luminescence bands observed in CZT-I doped with In at 4 K. See [49] for references.

At first, temperature dependence with the excitation above the bandgap was measured. Fig. 4.12 shows the temperature dependence of the PL spectra measured with liquid nitrogen cooled germanium detector. A continuous decrease of the PL signal with increased temperature is visible. No separate peaks in the spectral range around 1.1 eV can be distinguished, as the signal decreases very systematically and no persisting peak is observed in the higher temperatures. The position of the maximum of photoluminescence in the spectral range of deep levels in dependence on temperature is shown in Fig. 4.13.

The excitation spectroscopy was measured using the tunable Ti:Sapphire laser at fixed temperature of 4.7 K, see Fig. 4.14. The intensity of luminescence decreases when exciting below the absorption edge. The maximum of photoluminescence signal shifts closer to 1.1 eV. At higher energies the “1.1 eV” band of the CdZnTe sample changes its FWHM. With excitation close to the absorption edge, the band is very broad. In a selected region of excitation photon energies 1.34–1.40 eV, the band becomes narrower and much more distinct. However, no changes in the position of the PL maxima in dependence on excitation energy are visible.

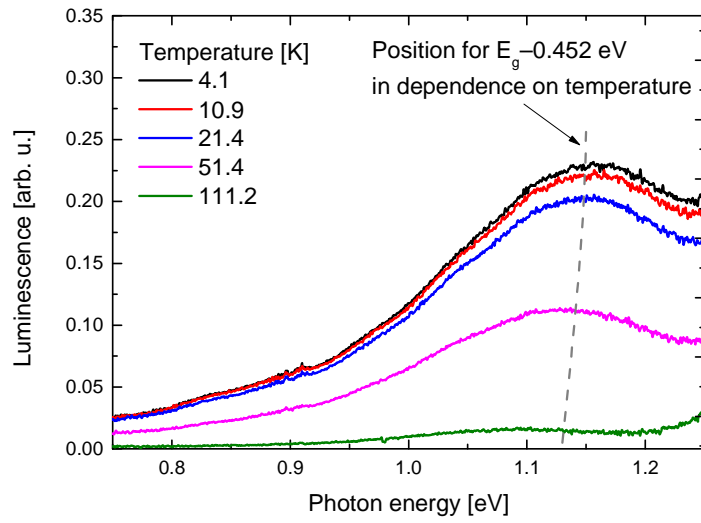


Fig. 4.12 PL spectra recorded by the Ge LN detector with above-bandgap excitation.

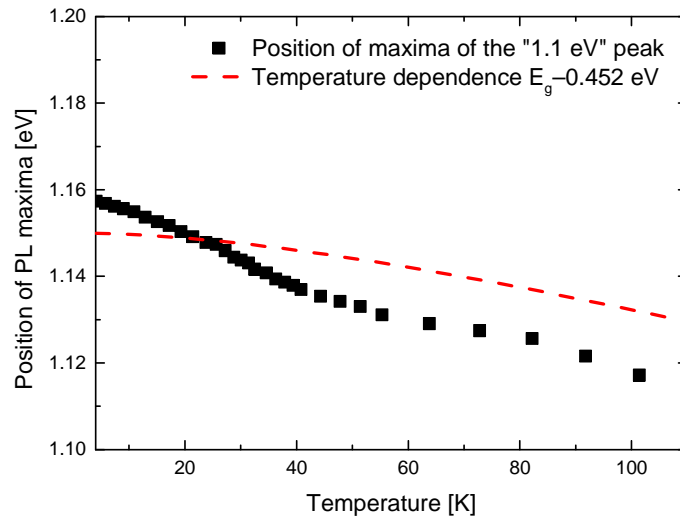


Fig. 4.13 Position of the luminescence maxima in the spectral range 1.0 – 1.2 eV versus temperature. Temperature dependence of $E_G - 0.452$ eV is plotted as well.

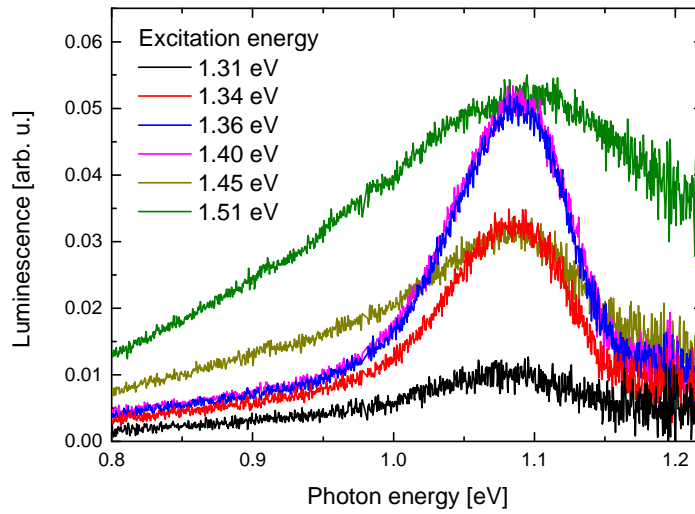


Fig. 4.14 Deep level photoluminescence spectra of CdZnTe in dependence on the excitation energy at 4.7 K.

At excitation energy around 1.38 eV a narrow band with PL maxima at 1.08 eV and FWHM = 0.1 eV dominates. This is in a good correlation with the measurement on CdTe material. It seems to be a similar transition as component 10 in Fig. 4.10. Other components present in CdTe have an intensity rise with the increased excitation energy and are not well resolved in the PL signal.

Because of this, no detailed analysis of the deep level structure, as presented for CdTe, can be done in the case of CdZnTe.

4.4. Chapter summary

The deep levels in the bandgap of CdTe:In and CdZnTe were studied through photoluminescence. The investigation was focused on the spectral range around 1.1 eV, where deep levels are present that are usually connected to polarization of the final detector. Through PL temperature and excitation dependencies, a unique and complex structure (compared to published papers) of three major components contributing to the 1.1 eV band was found in the case of CdTe. Evaluating the PL behavior, possible deep level processes connected with defects and impurities were proposed. Activation energies of the observed components were calculated. CdZnTe showed a rather poorer PL spectra compared to CdTe.

A broad band around 1.1 eV was observed and a narrow peak is dominant at excitation energy $\hbar\omega \sim 1.38$ eV. This could be a component similar to component 10 observed in CdTe. Other peaks could not be distinguished by used methods. The results were compared to published literature.

5. Charge transport and detector performance

5.1. Contactless Sample Characterization

The charge transport properties were investigated on indium doped n-type CdZnTe samples with a spatial distribution of resistivity. As mentioned above, high resistivity is desired for a better signal-to-noise ratio. Homogeneity of the detector material is also wanted for a stable detector performance and a high material yield in the device fabrication. Sample CZT-I was selected as a representative specimen for a detailed charge transport study. At the beginning of the study, the sample was mechanically polished. No metal contacts were deposited at this point. The dimensions of the sample were $6.4 \times 2.7 \times 2$ mm³. The resistivity map of the sample is shown in Fig. 5.1. After the contactless measurement, Hall parameters of the sample were measured. While the exact values for charge concentration and mobility are inconclusive because of a bad repeatability of the measurement, the sample was determined as n-type. The sample seems to have a special distribution of resistivity while having a homogeneous concentration of zinc, studied by the position of exciton bound to donor in the photoluminescence spectra map.

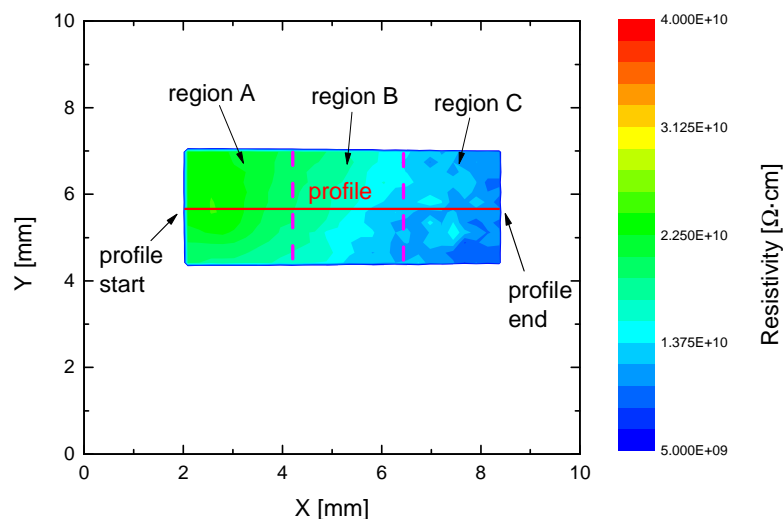


Fig. 5.1 Resistivity profile of sample CZT-I. Depiction of profile selection.

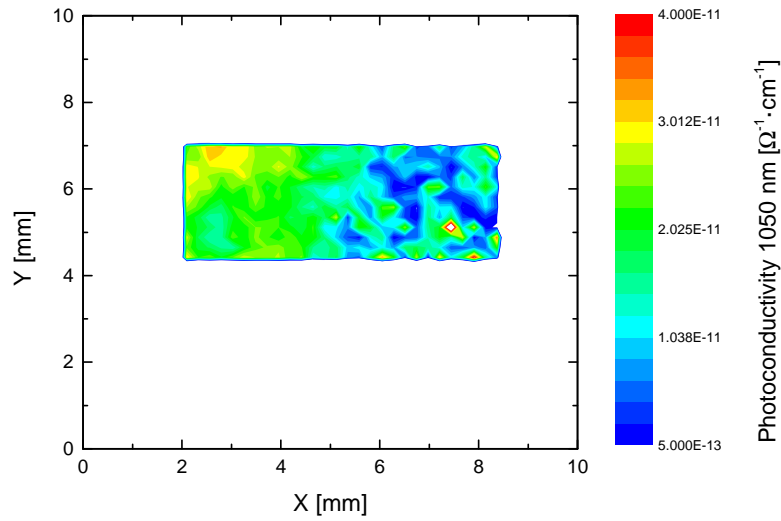


Fig. 5.2 Photoconductivity map of sample CZT-I. Incident photon energy 1.12 eV, photon flux $\varphi=8 \cdot 10^{13} \text{ ph} \cdot \text{cm}^{-2} \cdot \text{s}^{-1}$.

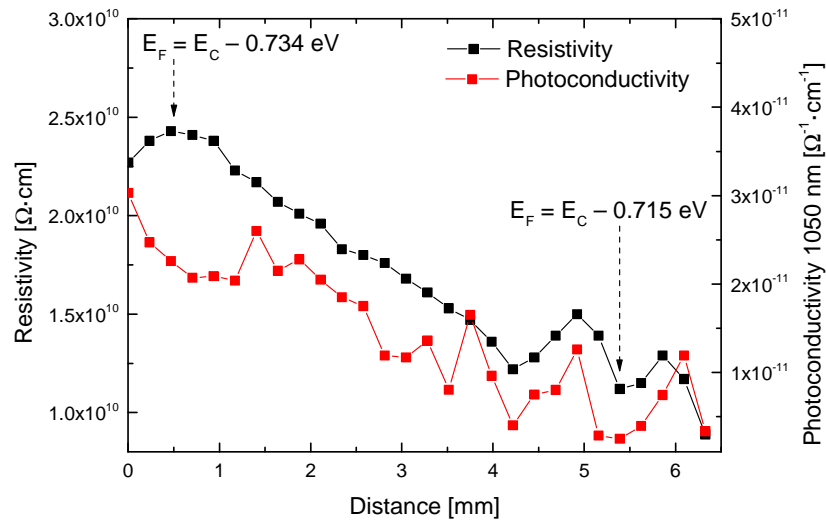


Fig. 5.3 Resistivity and photoconductivity correlation of sample CZT-I.

For the photoconductivity map measurement, a light with a wavelength of 1050 nm was used. This corresponds to the incident photon energy of 1.18 eV and is well below the bandgap to neglect the surface recombination, and yet is still partially absorbed into the bulk of the material. The photoconductivity map is shown in Fig. 5.2. Some of the points could not have been measured and appear white in the map, mostly on the edge of the sample. The reason for these faulty measurements can be an insufficient absorption and evaluation into negative

photoconductivity values or not satisfactory surface preparation inducing additional surface recombination of the photo-generated charge carriers. The behavior of resistivity and photoconductivity was studied up close in the profile depicted in Fig. 5.1 and is shown in Fig. 5.3.

Taken from the starting point at $x = 0$ mm the measured resistivity has an apparent anti-correlation with photoconductivity up to the point with maximal resistivity value and a little after that. From about $x = 1.5$ mm on, there is a correlation between resistivity and photoconductivity, as both of the parameters decrease towards the end of the profile. This is the same behavior as observed on CdZnTe samples grown at the Institute of Physics at Charles University [26] that can be explained using the Fermi level shift theory. Due to different compensation conditions the Fermi level shifts within the sample profile and the resistivity changes [34]. This mechanism also changes the photoconductivity of the material because of the different deep level occupancy. Fig. 4.11 shows the map of photoluminescence using IR light. The changes in the Fermi energy position can occur due to different concentrations of deep levels involved in the compensation process throughout the sample. A detailed model explaining the behavior of resistivity and photoconductivity will be proposed later on with the comparison of resistivity to other charge collection parameters.

Photoluminescence of CZT-I shown in Fig. 4.11 indicates peaks typical for a CdZnTe sample with exciton bound to donor (DX), exciton bound to complex defects with In dopant (C) and its phonon replicas and A-center (AC). Free exciton is not visible, indicating only a mediocre crystalline quality of the material. Also no excitons bound to acceptor are visible in the photoluminescence spectra. Confronted with the resistivity and photoconductivity profile of Fig. 5.3, the photoluminescence spectra do not show any relative changes between the peaks in the range of 1.3–1.7 eV.

While investigating the luminescence with a germanium detector and thus studying the deep levels, two deep level peaks are visible, see Fig. 5.4. The area of the peak in the proximity of 1.1 eV increases only slightly throughout the profile with certain values scattering. The deep level around 0.84 eV decreases more clearly in the latter part of the profile. It should be noted that the energy positions are meant as the position of the peak maxima, not ZPL. Changes in the photoluminescence

of the near midgap level at 0.84 eV can be connected to a concentration or occupancy change of the defect causing the deep level.

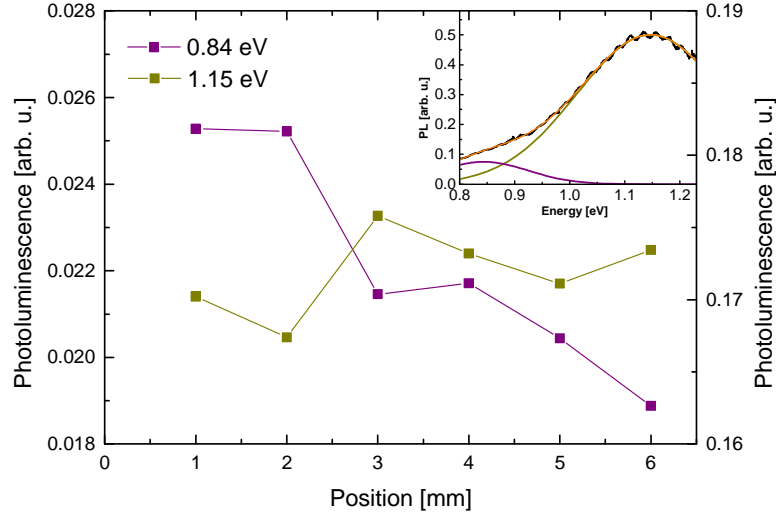


Fig. 5.4 Photoluminescence profile at temperature 4.7 K, measured with a germanium detector.

5.2. Detector Performance

5.2.1. Electron Collection

For electrical measurements of sample CZT-I, metal contacts were prepared. Prior to contact deposition the sample was mechanically lapped and consequently polished in several steps using an Al_2O_3 abrasive with a smaller abrasive size with each polishing step. The final abrasive particle size was 1 μm . Afterwards the sample was chemically polished in a 1% Br-ethylenglycol solution on a silk pad for 60 seconds on each side and then etched in a 1% Br-methanol solution again for 60 seconds. Cleaning was done by rinsing in methanol, acetone and isopropanol. Finally, the sample was dried using compressed air. The final dimensions of the sample were $6.3 \times 2.6 \times 1.9 \text{ mm}^3$. Gold contacts were prepared on both $6.3 \times 2.6 \text{ mm}^2$ planes of the sample using the chemical electroless deposition.

Through masking the sample was then divided into three regions with approx. homogeneous resistivity (Region A and Region C) and a region with the resistivity

gradient (Region B). The masking of the sample is depicted in Fig. 5.1. The results of α -spectroscopy using a ^{241}Am source for Region A–C are shown in Fig. 5.5–Fig. 5.7, respectively. Only about 300 V bias could have been applied in the spectra investigation. The mobility–lifetime $\mu\tau$ product of the charge carriers is calculated using the Hecht equation

$$Q = Q_0 \cdot \frac{U \cdot \mu\tau}{L^2} \cdot \left(1 - e^{-\frac{L^2}{U \cdot \mu\tau}} \right), \quad (5.1)$$

where L is the width of the sample and U is the applied bias.

The ^{241}Am peak is visible even at low bias, which indicates a good charge collection efficiency of all regions, correlating with the relatively high mobility–lifetime product.

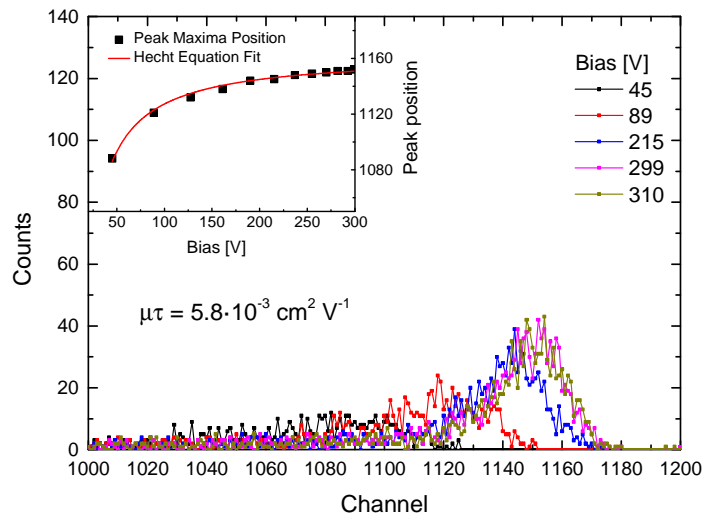


Fig. 5.5 Measured α -spectroscopy of Region A. Electron mobility–lifetime product calculated using the Hecht equation.

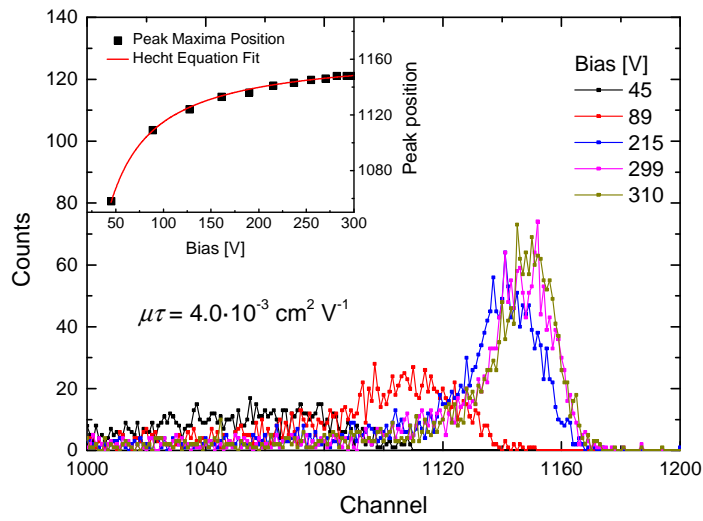


Fig. 5.6 Measured α -spectroscopy of Region B. Electron mobility–lifetime product calculated using the Hecht equation.

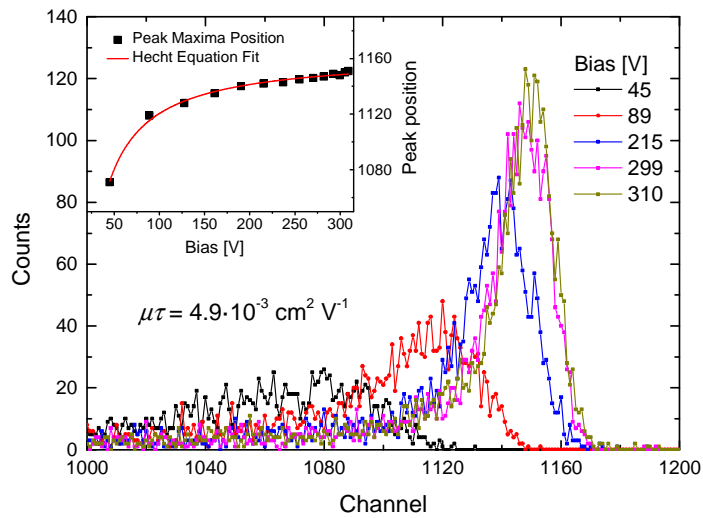


Fig. 5.7 Measured α -spectroscopy of Region C. Electron mobility–lifetime product calculated using the Hecht equation.

The evaluated mobility–lifetime $\mu\tau$ products have similar values in all of the regions of the sample. However a slight discrepancy is visible.

For a better understanding of the differences between the regions of the sample, investigation through laser–induced transient–current–technique (L–TCT) was implemented. In this method, free charge carriers are generated by photo–excitation

and their transport through the biased sample produces a current spike at the metal contacts. A standard L–TCT signal is shown in Fig. 5.8.

The L–TCT pulse recognizes several mechanisms within the measurement. At first the photon pulse generated using laser or laser diode, usually with incident photon energy above the bandgap, hits the sample and charge carriers are generated. Depending on the bias polarity electrons or holes can be collected. Afterwards the generated charge is transported through the material bulk and arrives at the contact opposite to the irradiated contact. The charge carriers are generated and travel through the sample in an ensemble. The arrival of the majority of charge carriers onto the non–irradiated electrode can be determined through the evaluation of the inflection point of the current curve. At that point the statistic mean passed through the detector and the transit time of the charge carriers is pinpointed. Detailed description of the L–TCT measurement is written in [46], [59].

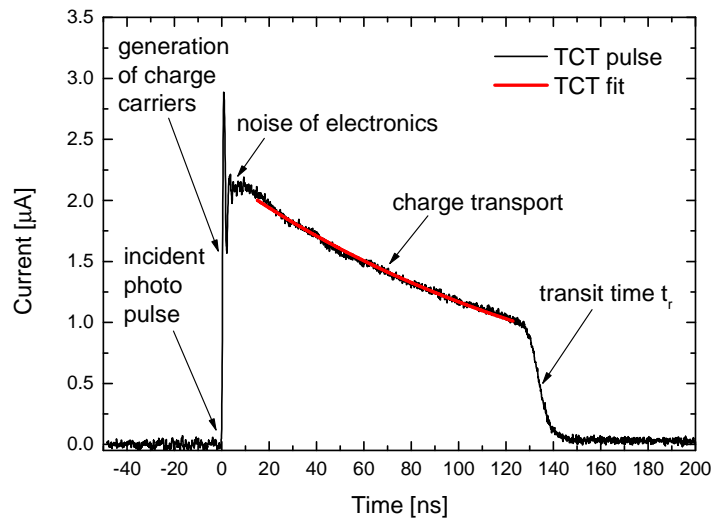


Fig. 5.8 Typical L–TCT pulse of CZT–I, biased at 300 V, with depiction of the pulse properties and charge transport fit.

With transit time t_r , effective mobility μ^{eff} of the carriers can be calculated using the equation as developed by Ramo [40]

$$\mu^{eff}_{e,h} = \frac{L^2}{U \cdot t_r} \quad (5.2)$$

The evaluated mobility is “effective”, as it is influenced by trapping levels, contacts and space charge in the sample. Throughout the profile of the sample, as depicted in Fig. 5.1, 17 points were taken for the L–TCT measurement, having a resolution of approx. 0.35 mm. For this measurement the laser beam was focused to have its diameter smaller than 1 mm to illuminate the majority of the corresponding region of the sample without illuminating the side of the sample. The rather large laser diameter compared to the profile resolution means that the measured point could be influenced by the other measured points in its vicinity. However, it should be noted that an average signal in the laser diode light diameter was measured and the relative changes in the sample were investigated. Three points were selected for the results presentation, each one in a different region of the sample. The L–TCT curves with evaluated electron mobility μ are shown in Fig. 5.9 .

Evaluating the L–TCT curve, differences in the electron mobility values are observed. The point in Region A, which has a higher resistivity, shows a smaller value of mobility $\mu^{\text{eff}} = 866 \text{ cm}^2 \cdot \text{V}^{-1} \cdot \text{s}^{-1}$ and has a curved L–TCT signal, whereas Region C evinces a more constant current after charge generation and has mobility $\mu^{\text{eff}} = 950 \text{ cm}^2 \cdot \text{V}^{-1} \cdot \text{s}^{-1}$. The value of bulk electron mobility is usually referenced as $\mu \sim 1000 \text{ cm}^2 \cdot \text{V}^{-1} \cdot \text{s}^{-1}$. Suzuki et al. [60] published a decrease of the mobility measured with L–TCT pulses as an effect of charge carrier capture on shallow levels in the bandgap, the so called Poole–Frenkel–effect. Electrons composing the current pulse are trapped on shallow levels and are again thermally excited back to the conduction band in a matter of nanoseconds. This trapping causes a delay of the electron bunch arrival to the collecting electrode. The more charge carriers are trapped for longer time, the lesser seems the evaluated effective mobility. The concentration of the point defects (shallow deep levels) can influence the estimation of the electron mobility. Similarly, also defect clusters can delay the electrons travelling through the sample, forcing the electron to travel a longer path throughout the sample than in a simple straight line. Macroscopic defects also influence the evaluation of charge carrier mobility. The curvature of the current signal is related to the space charge formed by trapping of free carriers and to the weighted potential of the electric field inside the bulk of the sample. The reason for the space charge formation is usually the depletion of electrons.

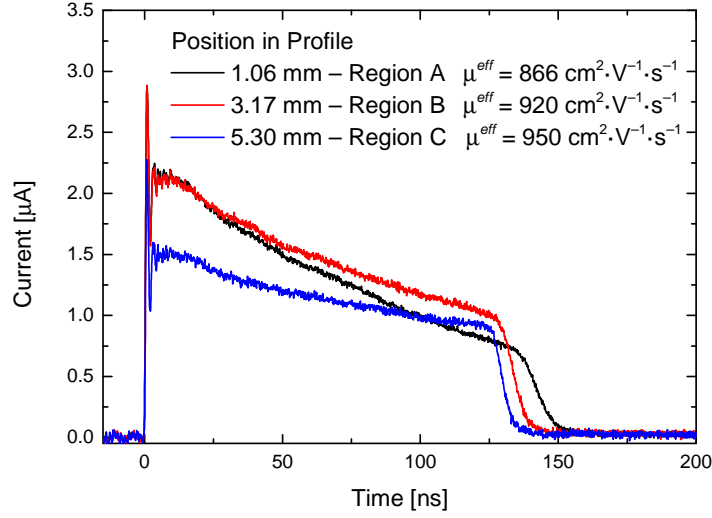


Fig. 5.9 *L-TCT pulse and evaluated mobility at three points at 300 V bias.*

If the L-TCT pulse evinces a clear transit time, the pulse can be fitted using the equation taken from [46]

$$i(t) = \frac{Q_0 E_0 \mu}{L} e^{-\left(a + \frac{1}{\mu\tau}\right)\mu t} \propto e^{-ct}, \quad (5.3)$$

where a is the screening parameter of the electric field, E_0 is the initial field value under the illuminated electrode and Q_0 is the initial drifting charge. Evaluating the transit time t_r and measuring the mobility–lifetime product, the equation (labeled 10 in [46]) for the screening parameter a can be solved numerically and the space charge inside the material bulk can be calculated using

$$a = \frac{eN}{\varepsilon_0 \varepsilon_r}, \quad (5.4)$$

where e is the elemental charge, ε_0 and ε_r are the permittivity of vacuum and relative material permittivity, respectively. N is the charge density, normalized on the elemental charge and it represents rather more a density of the amount of space carriers, having the unit $\text{e}\cdot\text{cm}^{-3}$. This parameter N will be further referenced only as space charge density.

Depending on the sign of a , positive and negative space charge can be distinguished. Positive value of a means positive space charge, whereas negative value of a represents negative space charge.

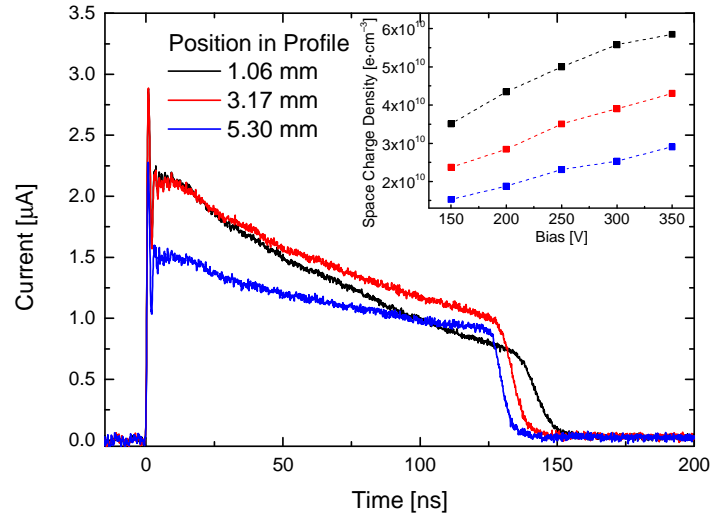


Fig. 5.10 L-TCT pulse at three selected points at 300V bias. Inset: evaluated space charge density is depending on applied bias at these points.

From the curvature of the L-TCT pulses, it is visible that the whole sample has a positive space charge in its bulk. Region A with higher resistivity and lower effective electron mobility has twice the value of space charge density as Region C. With higher bias, the difference increases even more. On the other hand, Region C has the lowest space charge density and evinces a higher effective electron mobility. With regard to [60], the conclusion follows that Region A has a higher concentration of shallow levels or contains more defect clusters causing the effective mobility to be lower in this part of the sample.

The slope of the electric field and the screening of the charge transport are crucial in evaluating the differences between the regions of the sample. To confirm the correlations between resistivity, electron mobility and space charge density, the parameters in the whole profile are shown in Fig. 5.11 and Fig. 5.12. As the sample resistivity and the sample itself seem very inhomogeneous, it is difficult to ascertain the exact values of the mobility-lifetime product and space charge density in the specific measured point of the sample profile. Because of this, the effective mobility values were evaluated with a systematic error

of $20 \text{ cm}^2 \cdot \text{V}^{-1} \cdot \text{s}^{-1}$ and the space charge density had an evaluation uncertainty of about ten percent of the calculated value.

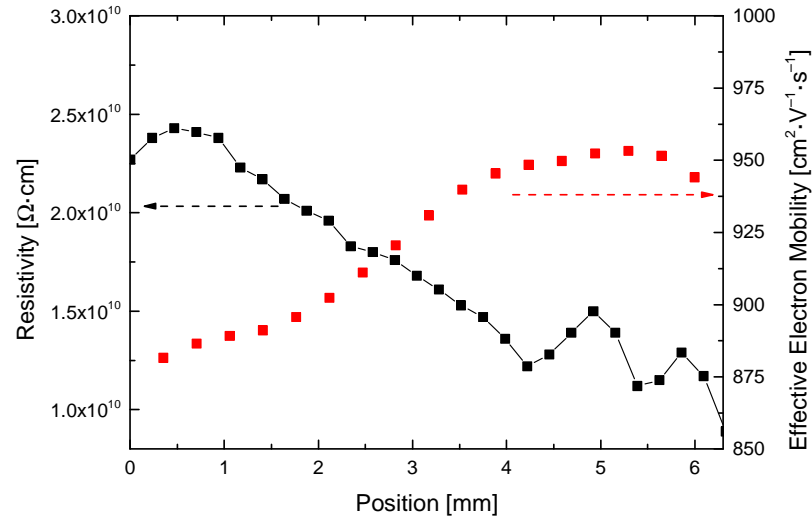


Fig. 5.11 Correlation between resistivity and calculated effective electron mobility in the sample profile at 300 V bias.

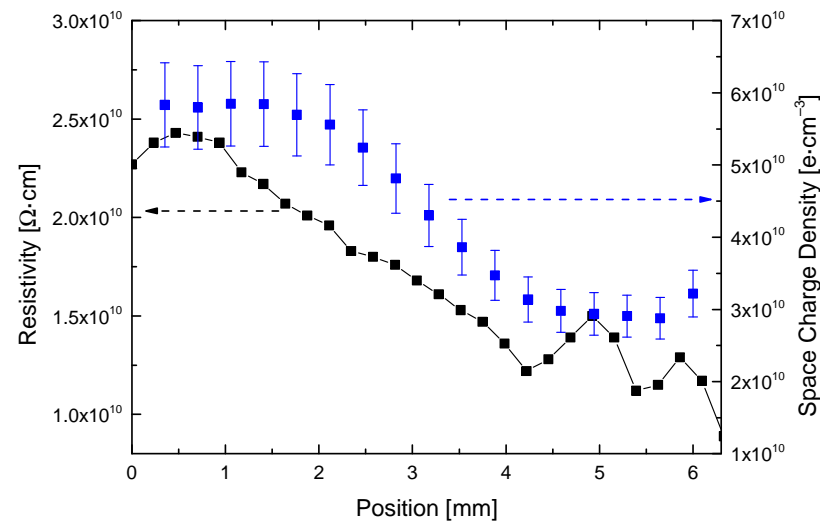


Fig. 5.12 Correlation between resistivity and calculated space charge density in the sample profile at 300 V bias.

The resistivity measured using the contactless method and the calculated effective electron mobility evaluated from the L-TCT pulses are very close to fully anti-correlated. Points around the maximal resistivity values show the lowest

effective mobility. In the high resistivity region the Fermi level is pinpointed near the middle of the bandgap and this influences the occupancy of the deep levels. At the end with lower resistivity, the Fermi level is shifted towards the conduction band. Region A with higher resistivity seems to have a greater concentration of either point defects or defect clusters causing the decrease of the evaluated effective electron mobility.

In contrast to mobility, the space charge density correlates with resistivity. It follows the transition trend from the high resistive region towards the region with lower resistivity and the space charge density value in this region decreases approximately by the factor of two compared to Region A.

The anti-correlation of electron mobility and space charge density depending on the bias applied to the sample is shown in Fig. 5.13 and Fig. 5.14.

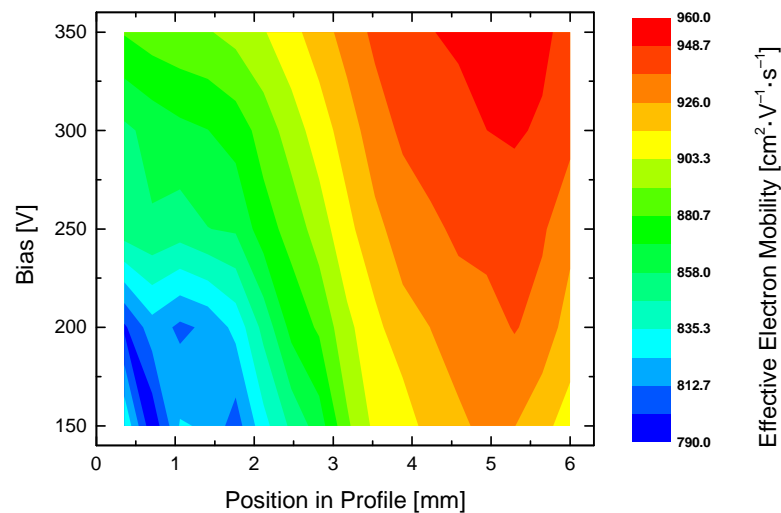


Fig. 5.13 Evaluated effective electron mobility map in dependence on the position on the profile of the sample and on the applied bias.

The evaluated effective mobility is dependent on the applied bias. It systematically increases with higher bias. This confirms the idea that the effective mobility is influenced by trapping on shallow levels or travelling a longer path around defect clusters. With a higher bias, the force drawing the electrons towards the collecting electrode is stronger. This way, electrons are travelling faster throughout the sample and cannot be trapped or their path is more straight.

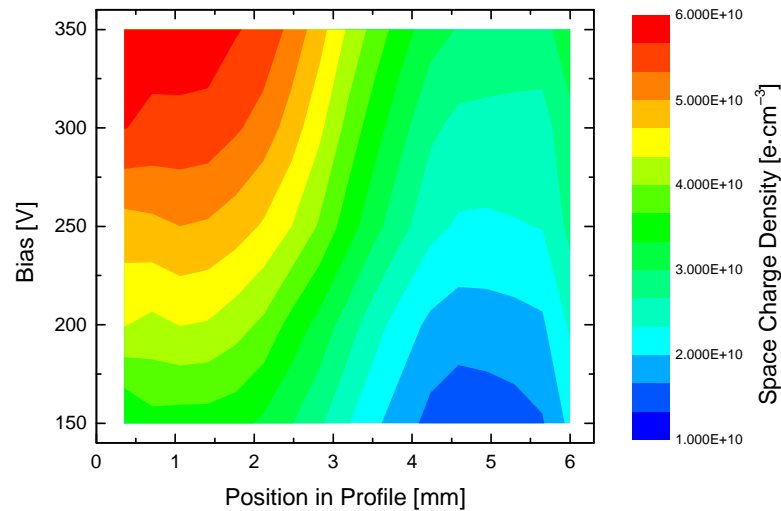


Fig. 5.14 Space charge density map in dependence on the position on the profile of the sample and on the applied bias.

5.2.2. Hole Collection

The ability to collect holes is a sign of a good detector performance. The collection of electrons or holes was changed by switching the applied bias to the opposite polarity. The sample used in these measurements was the same as with the electron collection measurement, no distinct adjustment was made for the study of hole collection. The obtained ^{241}Am spectra and the calculated mobility–lifetime $\mu\tau$ for Regions A–C are shown in Fig. 5.15–Fig. 5.17, respectively.

In the measurement of holes much fewer counts are recorded compared to the electron collection. Hole collection follows the trend of the electron measurement in the variance of the obtained $\mu\tau$ values. The lowest mobility–lifetime product is seen in Region C, whereas the highest value was measured in Region B. But the variance in the values is much smaller than in the electron measurement. The α –spectroscopy measurement results in all sample regions having a similar $\mu\tau$ of holes.

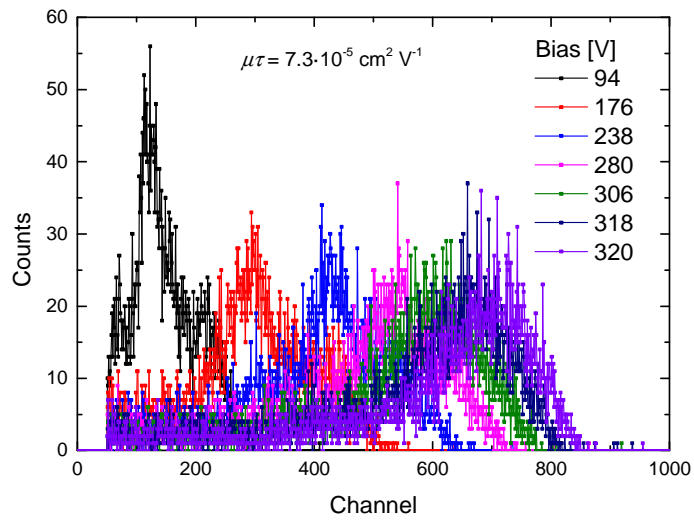


Fig. 5.15 Measured α -spectroscopy of Region A. Hole mobility–lifetime product was calculated using the Hecht equation.

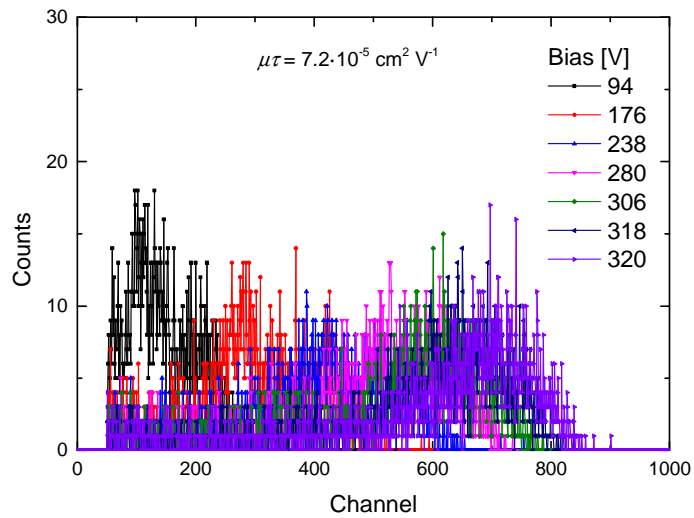


Fig. 5.16 Measured α -spectroscopy of Region B. Hole mobility–lifetime product was calculated using the Hecht equation.

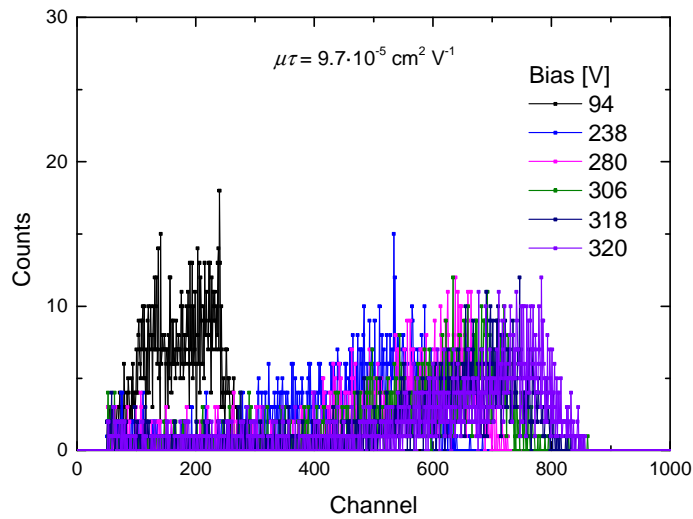


Fig. 5.17 Measured α -spectroscopy of Region C. Hole mobility–lifetime product was calculated using the Hecht equation.

As with the electron measurement, L–TCT pulses were studied for hole collection. The typical L–TCT pulse for holes is shown in Fig. 5.18. Holes evince much greater transit time value than electrons, which is a manifestation of a much smaller mobility of the positively charged carriers. The L–TCT pulses for holes also exhibit a greater noise when compared to electrons. The curvature of the pulse is opposite to the curvature of measurement with electron, as the current here is increasing throughout the transport. This is caused by a stronger electric field when nearing the cathode of the sample and in the presence of a positive space charge in the sample. After arriving at the non–illuminated electrode and contributing to the measured current (after transit time t_r), a slow relaxation part is visible. In this part the captured holes are released through a thermal mechanism and produce a slow relaxation current. This effect also finds place in electron collection, only the electrons seem to be released much faster and the relaxation contribution to the measured current is hardly visible.

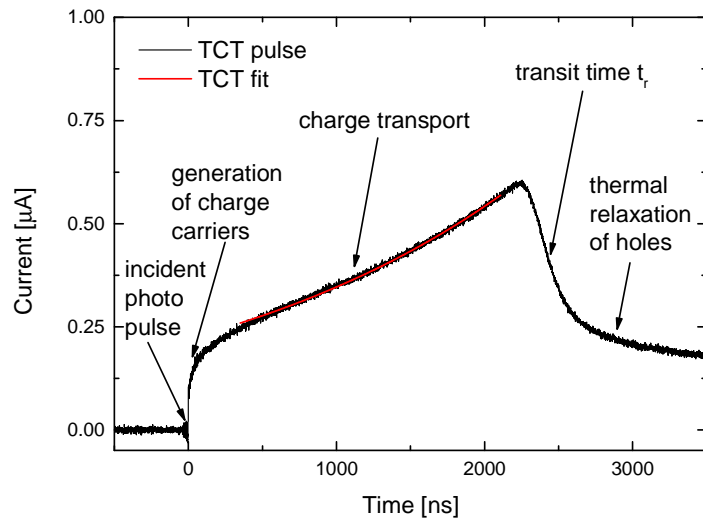


Fig. 5.18 Typical L-TCT pulse of CZT-I, biased at 300 V, with depiction of the pulse properties and charge transport fit.

Fig. 5.19 and Fig. 5.20 show the values for effective hole mobility and space charge density, evaluated using equations (5.2) and (5.4), respectively.

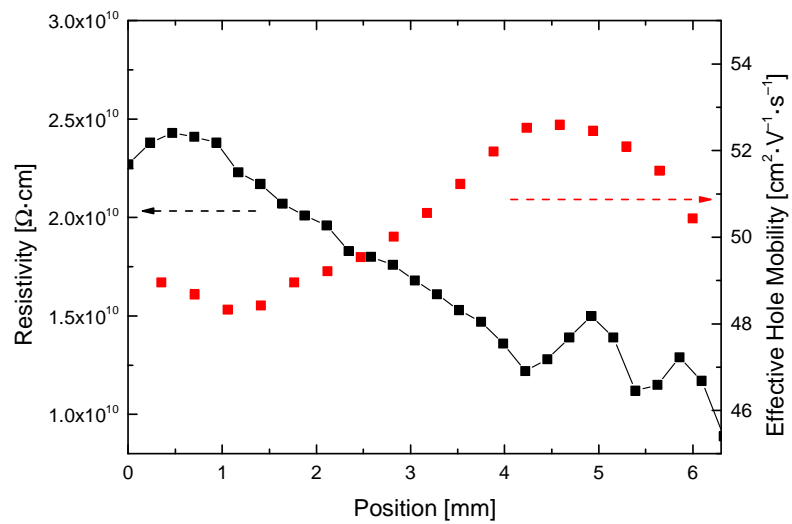


Fig. 5.19 Correlation between resistivity and calculated effective hole mobility in the sample profile at 300V bias.

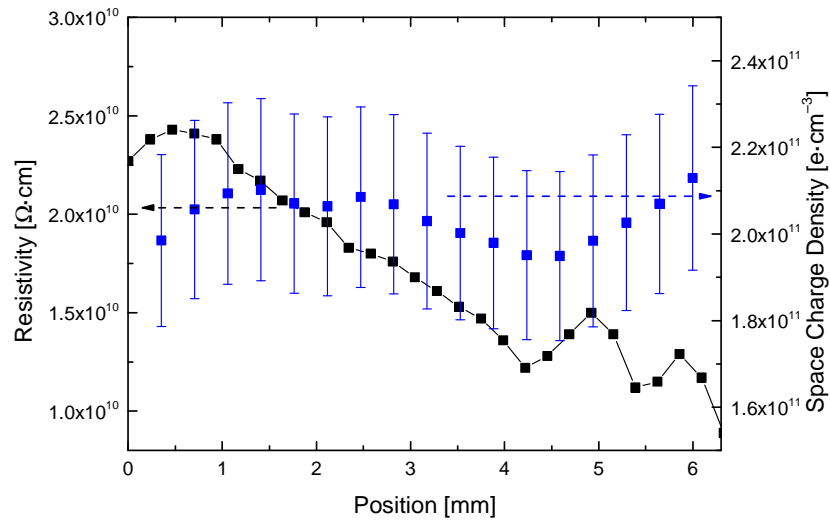


Fig. 5.20 Correlation between resistivity and calculated space charge density in the sample profile at 300 V bias.

The values of effective hole mobility vary between $48\text{--}50\text{ cm}^2\cdot\text{V}^{-1}\cdot\text{s}^{-1}$. The error of the mobility evaluation was about $5\text{ cm}^2\cdot\text{V}^{-1}\cdot\text{s}^{-1}$. The similar effective mobility corresponds with the similar mobility–lifetime product measured using α –spectroscopy in the profile throughout the sample.

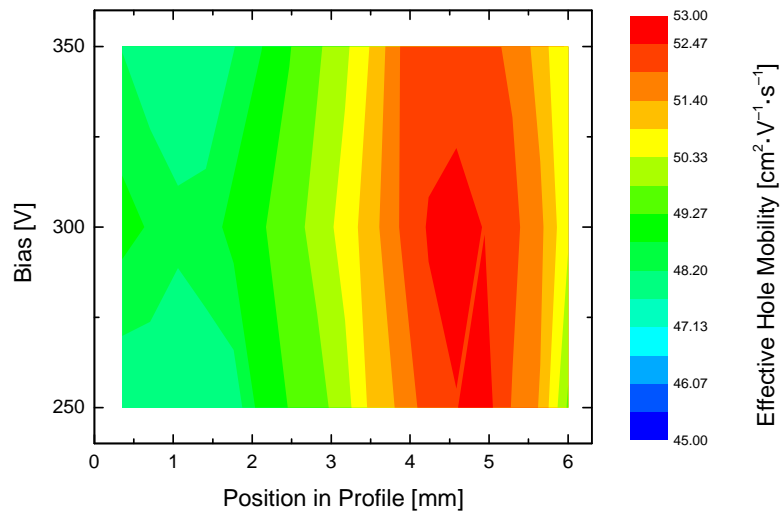


Fig. 5.21 Evaluated effective hole mobility map in dependence on the position on the profile of the sample and on the applied bias.

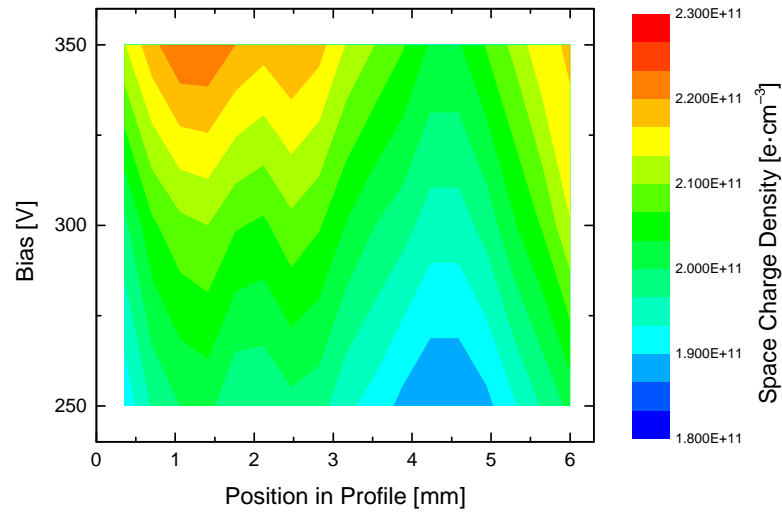


Fig. 5.22 Space charge density map in dependence on the position on the profile of the sample and on the applied bias.

The evaluated effective hole mobility correlates with the profile of electron mobility. A region with high effective electron mobility also has high effective hole mobility and vice versa. Only the absolute values and their variation throughout the sample differ. The space charge with hole collection has the same polarity compared to the collection of electrons. When collecting holes, the sample is charged with the space charge density varying around $2.05 \times 10^{11} \text{ e}\cdot\text{cm}^{-3}$. The amount of the space charge is larger than in the collection of electrons. Nevertheless, the profile of the space charge correlates with the space charge when measuring electrons. For comparison, the parameters in dependence on the applied bias are displayed in Fig. 5.21 and Fig. 5.22. In the effective hole mobility evaluation there seems to be a semi-saturation of the values when measuring with 350 V bias. Even despite of that, the effective hole mobility and the evaluated space charge density are in good anti-correlation as in the case of collecting electrons.

5.3. Theoretical model

The evaluated results can be explained using the model of the Fermi level shift throughout the sample, as used in [26], only slightly modified. The preconditions for the theoretical model development are: Region A has a higher resistivity, higher

photoconductivity when illuminated by below bandgap radiation, lower effective mobility and a greater positive space charge, opposite to Region C.

Two theoretical models can explain the measured behaviors in the sample regions, depending on the lowered photoconductivity in Region C being caused by concentration decrease of conducting electrons or holes. The decisive factor is therefore the type of the conductivity, which by itself cannot be measured by the COREMA setup. Therefore both theoretical models will be discussed here.

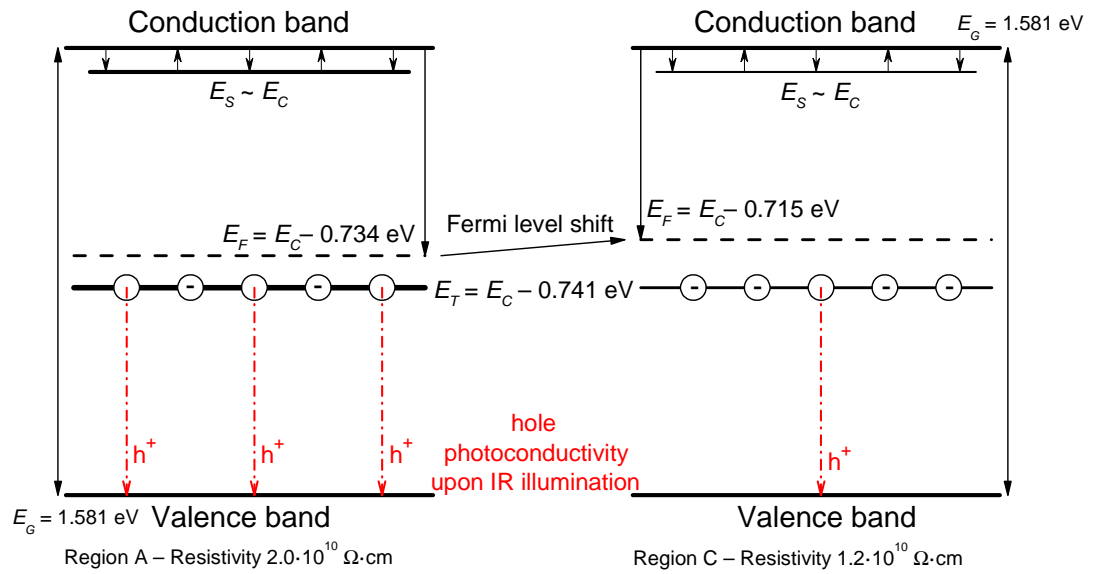


Fig. 5.23 Theoretical model I of the bandgap arrangement, supposing a hole photoconductivity.

Model I counts with the increased photoconductivity in Region A being caused by holes. The schema of the bandgap trapping and de-trapping processes is depicted in Fig. 5.23. In Region A, there is a higher concentration of the deep level close to the midgap position, $E_T = E_C - 0.741 \text{ eV}$. This causes that the Fermi level is positioned closer to midgap and results in a higher resistivity of Region A. In Region C the concentration of the midgap E_T level is smaller and the Fermi level is shifted towards the conduction band, resulting in the lower resistivity measured in this region. The levels are deliberately placed in the upper part of the bandgap, because of the sample being an n-type in the Hall measurements. The midgap level is set to be the 0.84 eV level, observed in photoluminescence and placed from the valence band, $E_T = E_V + 0.840 \text{ eV} = E_C - 0.741 \text{ eV}$. The supposed difference in the concentration of this deep level between Region A and C is also partially

supported by photoluminescence, where the signal of this level is greater in Region A. More charge carriers can be trapped on the level with a higher concentration and this can result into the evaluated greater space charge density in Region A.

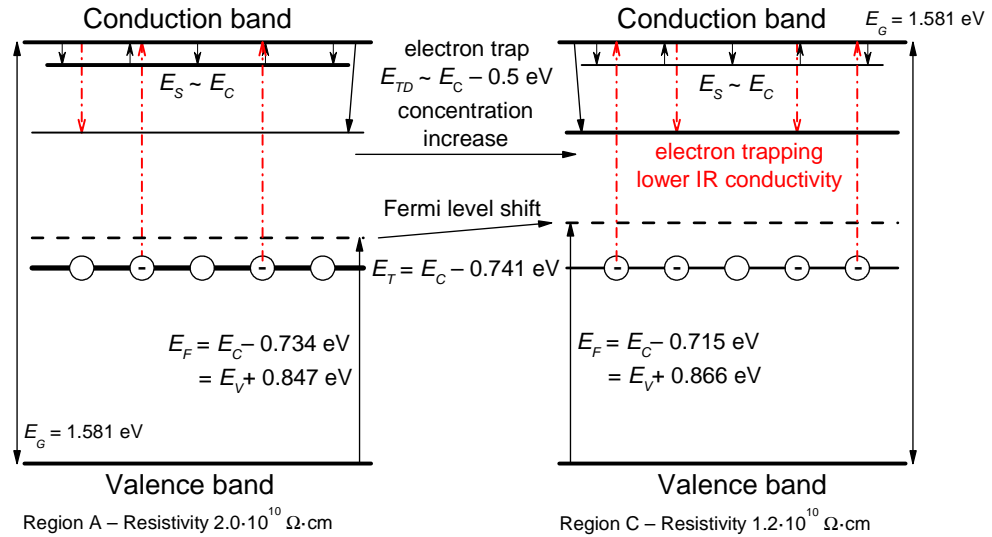


Fig. 5.24 Theoretical model II of the bandgap arrangement, supposing an electron photoconductivity.

The shift of the Fermi level also influences the occupation of the deep level E_T . In the case of the Fermi level closer to the midgap level E_T , the level is less filled with electrons and when illuminated, more holes can be excited to the valence band and can cause the increased photoconductivity in Region A. In Region C, the occupation of electrons at the midgap level is higher and holes from the deep level cannot be excited and contribute to conductivity. The changes in the effective mobility evaluation were discussed in chapter 5.2.1 as a result of charge trapping at point defects (as described in [60]) or due to defect clusters “prolonging” the path the charge carriers must travel through the sample. This is depicted in the model as shallow level E_S placed several meV below the minimum of the conduction band. Region A has a higher concentration of this shallow level, which is far from the Fermi level and is not influencing its shift. Its higher concentration results in a lowered effective mobility.

Fig. 5.24 shows the other model, model II, explaining the measured effects. It is similar to model I assuming that the Fermi level shift is caused by different concentrations of a near midgap level E_T . This results in the different space charge density. The lower effective mobility in Region A is then an effect of an increased electron trapping on shallow defects with energy E_S .

In contrast to model I, the photoconductivity here is caused by electrons. The decrease of photoconductivity in Region C would generally be in contradiction with the bandgap arrangement described by model II, because with the Fermi level positioned closer to the conduction band, the deep level is more filled with electrons and should have a higher photoconductivity. But the concentration of the deep level E_T is lowered and photoconductivity is affected by both concentration and occupancy of the level. With specific parameters of the midgap level, the decreased photoconductivity can be explained. However, the value of photoconductivity decreases almost by one order of magnitude in Region C, see Fig. 5.3. Because of the rather large decrease of the measured value, the presence of a deep electron trap E_{TD} in the bandgap far away from the Fermi level is possible. This deep level would trap the excited electrons and cause the decrease of photoconductivity in Region C. The level is not connected to other measurements and would have to be non-radiative and not appearing in the photoluminescence measurements.

Both theoretical models I and II can explain the behaviors of resistivity and space charge density in the sample. Calculations of the proposed bandgap arrangement were done using a computer program developed at the Institute of Physics at Charles University. The program solved the drift equation, Poisson equation and Shockley–Read–Hall trapping model for the sample simultaneously. The calculations were made for the measurement of electrons at 300 V bias. The input parameters for the calculations without photoconductivity and the resulting steady state outputs are written in Table 3.1. The model assumed the bandgap energy $E_G = 1.581$ eV (taken from [4]), the band bending on the metal–semiconductor interface of $E_C = 0.858$ eV, and the capture cross-sections of the midgap level $\chi_e = 5 \cdot 10^{-30}$ cm² and $\chi_h = 5 \cdot 10^{-13}$ cm² for electrons and holes, respectively.

Sample Region	Fermi level position [eV]	Concentration of deep level E_T [cm^{-3}]	Simulated resistivity [$\Omega \cdot \text{cm}$]	Simulated space charge density N [$\text{e} \cdot \text{cm}^{-3}$]
Region A	$E_C - 0.734$	$1.1 \cdot 10^{11}$	$2.43 \cdot 10^{10}$	$5.81 \cdot 10^{10}$
Region C	$E_C - 0.715$	$3.2 \cdot 10^{10}$	$1.23 \cdot 10^{10}$	$2.32 \cdot 10^{10}$

Table 5.1 Parameters for the theoretical model simulation of the bandgap effects.

The results obtained from the calculation of the bandgap arrangement seem in good correlation with the observed behaviors seen in Fig. 5.12. The calculated profiles of space charge density for Region A and Region C are depicted in Fig. 5.25 and Fig. 5.26, respectively.

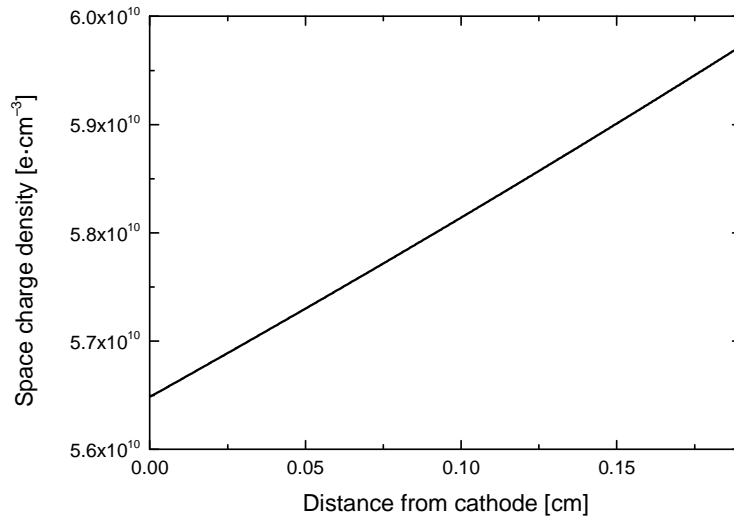


Fig. 5.25 Simulated profile space charge density in Region A.

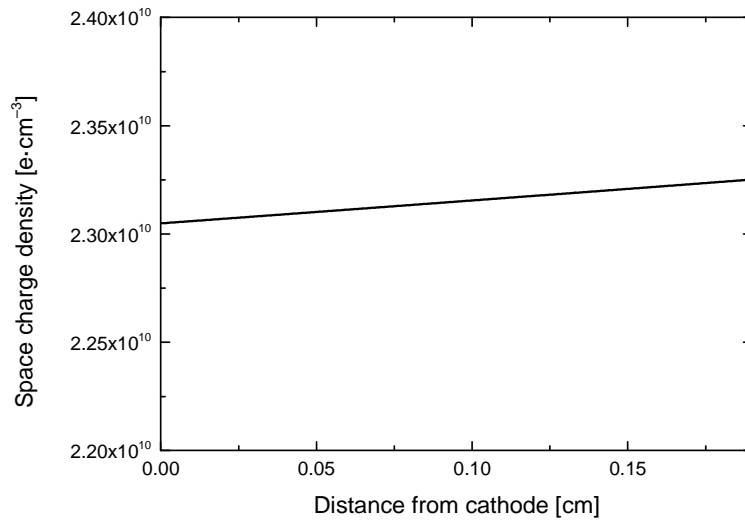


Fig. 5.26 Simulated profile of space charge density in Region B.

The basic outline of the theoretical model of the Fermi level shift explains the differences between Region A and Region C in resistivity and space charge density. For a decisive selection of which model works for the photoconductivity measurement, other measurements must be done.

Pousset *et al.* [61] published a study where the contribution of electrons and holes to conductivity can be distinguished by measuring the L–TCT pulse with spectral scanning of below–bandgap illumination wavelengths.

5.4. Chapter summary

A CdZnTe sample with homogeneous Zn concentration, but inhomogeneous resistivity distribution was studied. Resistivity and photoconductivity were correlated with photoluminescence and detector performance (measured by α –spectroscopy and L–TCT). The observed behavior of effective electron mobility and space charge density induced after biasing the sample is explained using the Fermi level shift theory. The resistivity and space charge density are influenced by the concentration change of a near midgap level. This assumption is supported by the photoluminescence measurement. The obtained data were confronted with theoretical model calculations and were in good correlation.

6. Surface Preparation

The focus of this chapter lies on a study of influence of surface preparation in the final detector development.

Recent research shows that the surface leakage current is very dependent on the surface treatment prior to contacts deposition [62]. Different mechanical and chemical treatments of the CdTe/CdZnTe sample can lead to different leakage currents [8], [63]–[66]. It has been shown that the surface treatment on the lateral sides can significantly influence the detector performance [66]–[69]. Procedures commonly used during fabrication of detectors are the surface polishing with different-size abrasives and chemical etching in variable solutions, mostly Br–methanol [70], [71]. The impact of mechanical polishing and chemical etching in Br–methanol solutions has been studied by measurements of IV characteristics and photocurrent [8], [72]–[74], while the surface morphology was investigated using optical microscopy, interferometry and X–ray photoelectron spectroscopy (XPS) measurements [62], [70], [75].

A number of publications indicate an increased surface leakage current after chemical treatment than the mechanical one [76], [77]. However, the published results did not present a clear conclusion about an optimal surface treatment process from the detector performance viewpoint.

All of the published investigations of the surface treatments on the material and detector performance have been measured on the plane used for metal contacts by current–voltage characteristics and X–ray spatial mapping with a gold strip or plane contacts [64], [72], [74], [78], [79]. Little attention for investigation of the surface without gold contact has been paid.

Bensouici *et al.* [75] investigated the plane surface roughness after lapping and polishing using AFM and contactless resistivity measurement. With a greater focus on surface morphology they observed a change of resistivity during chemical etching, but the results were only briefly mentioned.

Photoluminescence measurement has been done so far on low resistive material, material doped with Sn, Ge or Fe; polycrystalline or epitaxial material [56], [80]–[82].

This chapter offers a complex study of contactless resistivity, contactless photoconductivity [7], [83] and photoluminescence signal of both shallow and deep energy levels in dependence on the surface preparation on semi-insulating detector-grade CdTe and CdZnTe samples. This enables the research of the material parameters independent of metallization, which can be useful for understanding the variations in detector's performance.

6.1. Surface effects on deep levels

The effect of surface preparation of the CdTe and CdZnTe samples on deep levels is difficult to ascertain, as the effect can be small and the standard methods (PICTS, DLTS, etc.) have insufficient resolution or the effect can be covered by the effects of metallization of the surface in contact development. Optical methods are therefore useful in the surface characterization.

The effects of surface treatments on shallow levels in photoluminescence measurement are substantial. If the surface layer is damaged, the charge excited by illumination recombines on the structural defects, leaving the PL structure on shallow donors and acceptors completely distorted. The mechanically damaged layer must be removed in order to get a clear PL signal, see Fig. 6.1.

However, the effects of intentionally induced stress to the crystalline lattice done by “scratching” the surface with a pyramid diamond indenter was investigated in [84]. This way, linear trenches were carved into the material, causing a great mechanical stress. It resulted in the increase of a shallow level called the Y-line.

The focus of the present chapter is to study the effect of preparation procedures usually employed for detector preparation, such as mechanical polishing and chemical etching. With mechanical polishing the whole surface area is exposed to mechanical stress that is smaller than when using an indenter, but reaches the whole sample surface. The focus lies here on the evolution of the signal originating from the deep energy levels as a result of surface treatment (photoluminescence in the range of 0.7–1.4 eV).

Sample CT-II was used for the investigation. The resistivity of the sample $\rho \sim 8 \cdot 10^8 \Omega \cdot \text{cm}$ was measured using the contactless method (COREMA). After cutting from the ingot with a diamond wire the sample was lapped and then

polished in several steps using Al_2O_3 abrasive. The intention was to remove with each polishing a layer three times thicker than the grain size used in the previous step. The last used grain size was $1\ \mu\text{m}$. After the initial measurement of the photoluminescence of the polished samples, they were chemically etched by immersion into a 1% Br-methanol solution for 1 min. Sample CT-II was etched successively four times and was used for spectral analysis, resistivity and detector performance measurement; sample CT-III was etched twice and was used only to study the temperature dependence of photoluminescence (see chapter 4.2.2). The thickness of the samples was measured using a digital indicator. The material removal was determined by the difference of the thickness of the sample with polished surface and the thickness after the chemical treatment.

Sample CT-II was used to measure the spectral dependence of photoluminescence after each surface treatment step (polishing and etching) applying the laser with excitation energy 1.94 eV. Fig. 6.1 shows the spectra measured with Si detector for the as-polished sample and the sample after subsequent etching done by immersion into the 1% Br-methanol solution for 60 s. The description of the measured peaks is presented in Table 4.2.

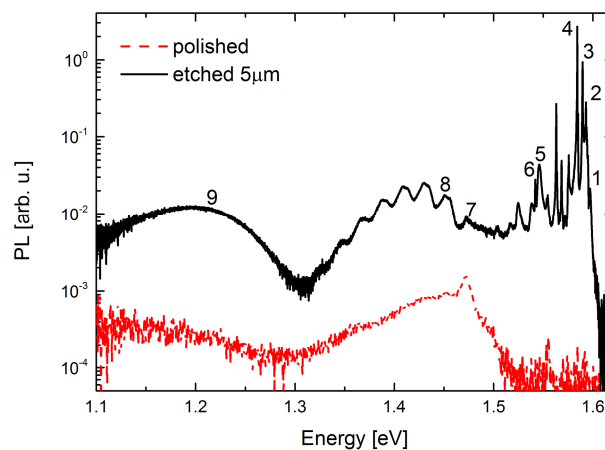


Fig. 6.1 Photoluminescence spectra of sample CT-II, measured with Si detector at 4.6 K using excitation energy 1.94 eV.

The measurement of the as-polished sample shows a much distorted photoluminescence spectrum in comparison with PL spectra of high quality samples. This is caused by the damaged surface layer present after mechanical treatment of the sample. However, the Y-line (peak 7) at 1.472 eV is clearly dominant in this

measurement. In literature, this peak is often linked to plastic deformation and is assigned to an exciton bound to Te glide dislocations [85]–[88]. After a slight etching of the sample the photoluminescence of excitons and donor–acceptor pairs becomes clearly visible, showing a good quality of the studied crystal.

The photoluminescence spectrum related to deep levels was obtained with a liquid-nitrogen cooled germanium detector. The spectra show a rather broad signal in the range of 0.8–1.3 eV. The chapter 4.2 of this thesis deals with the evaluation of the detailed measurement on the sample after etching. In chapter 4.2 there is also the investigation of the composition of the broad deep level peak and concludes into the evaluation of four different contribution to the deep levels in this spectral range, see Fig. 4.2, Fig. 4.3.

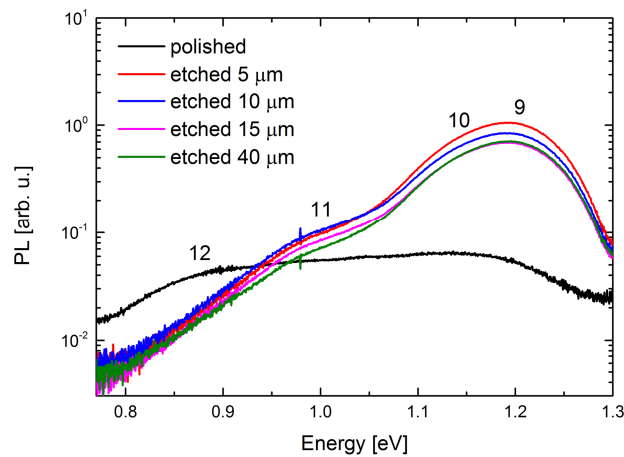


Fig. 6.2 Photoluminescence spectra of sample CT-II measured with Ge detector at 4.6 K with excitation 1.94 eV.

The deep level spectra depending on the amount of material etched away from the surface are shown in Fig. 6.2. To evaluate the dependence of the photoluminescence spectrum on surface treatment the deep level peaks 9–12 were fitted using the Gaussian function. The fitting procedures took into account the position of the peaks found in the best quality PL spectra obtained for the etched surfaces. The errors were calculated as the fit error itself and an estimated error in fitting of the peaks position that could change without greatly influencing the cumulative peak fit. An example of fitting the spectra is shown in the inset in Fig. 6.3. The fitted peak area was used as a significant parameter to evaluate

the photoluminescence. Fig. 6.3 shows the dependence of the fitted peak areas on the thickness of the surface layer removed by chemical etching on sample CT-II. The sample with as-polished surface shows the area of peak 12 at ~ 0.9 eV greater than the area of the other fitted peaks. With only 5 μm surface layer removal the luminescence of peaks 9–11 increases rapidly. At the same time the area of peak 12 diminishes. With further etching the luminescence of peaks 9–11 reaches the maximum and then slightly decreases. Through evaluation of the spectra it is assumed that peaks 9–11 are connected to bulk defects that are present in an increased concentration in the surface layer up to 15 μm . The signal of peak 12 remains practically the same with further surface treatments and is much lower than the signal of other measured deep levels. Fig. 6.1 shows the Y-line remaining almost unchanged during the etching treatments while the area of peak 12 changes. As the Y-line is often described as caused by plastic deformation and linked to tellurium dislocations and in this measurement it is independent on the area of peak 12, peak 12 seems to be connected with radiative recombination of carriers on another type of defects related to lattice disorder in a thin surface layer (< 5 μm). Both point defects (possibly connected with a stoichiometry deviation) and more extended defects due to the strain (or a combination of both effects) should be taken into account as origin of the PL band at ~ 0.9 eV.

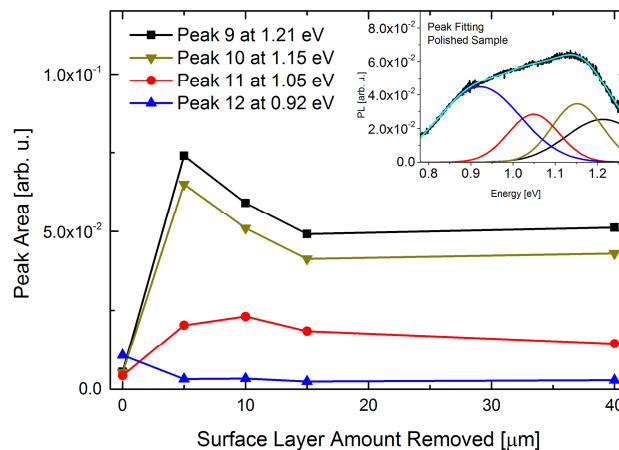


Fig. 6.3 Area dependence of bands 9–12 on total thickness of layer removed by consecutive chemical etching.

Luminescence bands with a maximum near 0.9 eV are reported rather rarely, bands near and below 0.8 eV are observed much more often. A broad luminescence band with components 0.85, 0.9, and 1.1 eV was observed by cathodoluminescence at 80 K in a deformed region (plastic deformation by indentation; low resistivity, nominally undoped sample) after annealing in inert atmosphere [18], [89], where a Cd-deficit in very disturbed material could be supposed. Doping with Ge induces a luminescence band in this region as well [18]. Sobiesierski *et al.* [23] observed a double luminescence band 0.875, 0.925 eV on the surface of p-type samples etched by Br-methanol; XPS showed that the surface was highly Cd-deficient (Te-rich). At the same time almost stoichiometry Cd/Te ratio surface generated PL spectra where “1.1-eV” and “1.4-eV” bands prevailed [23]. On the contrary, in this investigation the mechanically polished surface, where band 12 was more visible, had a better stoichiometry ratio than the surface after chemical etching. The chemical treatment produced a more Te-rich surface, but the luminescence of band 12 decreased upon such preparation.

The mechanical treatment induces the damaged layer that is shown in photoluminescence and can possibly influence the final detector performance. The thickness of the layer evaluated from photoluminescence measurement is up to 5 micrometers, but it is possible to vary within the order of magnitude.

The measurements of the PL spectra with InSb detector have shown a band with a peak near 0.65 eV that is well separated from the ~0.9 eV band. The PL spectra above 1.3 eV are dominated by the “1.4 eV-band” peaking at 1.43 eV. Its tail in the spectral range of the 1.2 eV can be considered as minor. It can increase an error of integral intensity of the band 9, but it cannot substantially change the used interpretation.

6.2. Resistivity and Photoconductivity

Sample CZT-V was used for the investigation of the influence of surface preparation on the resistivity. The single-crystalline sample was cut from an ingot grown by the Vertical-Gradient-Freeze method (VGF). The sample dimensions were $8 \times 5 \times 2 \text{ mm}^3$. The sample was of a semi-triangular shape. The first cut was done using a diamond-wire saw. Both of the large $8 \times 5 \text{ mm}^2$ plane surfaces of the sample

(usually contact surfaces) were then prepared using different treatments. Lapping by Al_2O_3 with grain size 9 μm and 4 μm (LAP9 and LAP4), polishing using Al_2O_3 with grain size 3 μm , 1 μm , 0.3 μm , and 0.05 μm (POL3, POL1, POL0.3, and POL0.05, respectively) were used. As a final step, the sample was immersed into a chemical 0.5% Br–methanol solution for 45 s (CHE1) and afterwards into a 1% Br–methanol solution for 180 s (CHE2). The summary of used surface preparation treatments is shown in

Table 6.1.

From this point on it should be noted that by using the contactless resistivity mapping for the sample characterization, only “apparent” values of the resistivity and photoconductivity are obtained. These values represent only the best mono–exponential fit of the measured charging curve and can differ from the bulk resistivity and photoconductivity values. The issue of correct evaluation of the contactless measurement data will be discussed later on in chapter 6.4. For now, however, the terms for resistivity and photoconductivity will be used without the adjective “apparent” and the meaning will be the best fit of the exponential data in the contactless resistivity evaluation.

The resistivity of the sample was mapped after each surface preparation process. Photoconductivity of the sample after different surface preparations was measured on the polished and chemically etched surfaces. The lateral sides were protected during the surface preparation and did not change during the measurements. No passivation was used for the plane surfaces.

Method	Abrasive, Etchant	Abbreviation	RMS Roughness [nm]	Oxide Thickness [nm]
Lapping	9 μm Al_2O_3	LAP9	—	—
Lapping	4 μm Al_2O_3	LAP4	—	—
Polishing	3 μm Al_2O_3	POL3	11.62	10.75
Polishing	1 μm Al_2O_3	POL1	4.99	—
Polishing	0.3 μm Al_2O_3	POL0.3	2.06	4.52
Polishing	0.05 μm Al_2O_3	POL0.05	2.27	—
Etching	0.5% Br–methanol for 45 s	CHE1	3.86	0.78
Etching	1% Br–methanol for 180 s	CHE2	—	0.69

Table 6.1 Surface preparation methods and parameters.

The surface roughness of the treated surfaces was measured by a noncontact three-dimensional surface profiler (Zygo, USA), which uses noncontact scanning white-light interferometry to acquire ultrahigh- z -resolution images. Only good reflective surface can be measured by this method. The surface roughness was therefore evaluated using this method on all types of surfaces except of LAP9, LAP4 and CHE2 (

Table 6.1). The values of the root-mean-square (RMS) surface roughness are also shown in the

Table 6.1.

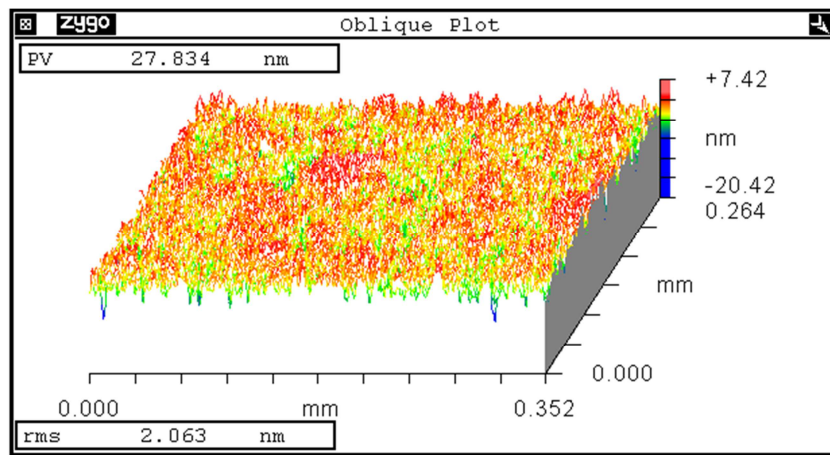


Fig. 6.4 Surface morphology after polishing with 0.3 μm size alumina (POL0.3). Scanning area is 0.352×0.264 mm².

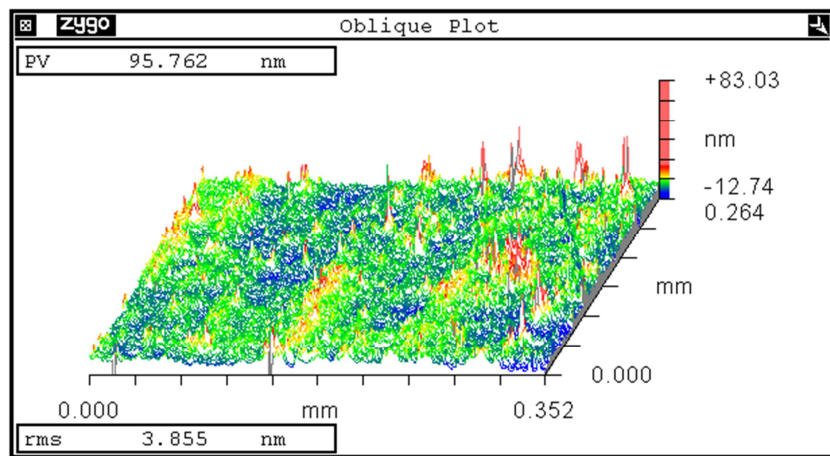


Fig. 6.5 Surface morphology after chemical etching with 0.5% Br-methanol solution for 45 s. Scanning area is 0.352×0.264 mm².

Two selected morphology representations of the detector sample after lapping with $0.3\ \mu\text{m}\ \text{Al}_2\text{O}_3$ (LAP0.3) and after etching in a 0.5% Br–methanol solution for 45 s (CHE1) are presented in Fig. 6.4 and Fig. 6.5. In contrast to mechanical lapping, lots of thin and very high peaks are visible after CHE1 procedure. This is due to the different etching velocity of these spots caused by stoichiometry deviation and/or structural defects of the crystal.

Right after each surface preparation procedure a resistivity map of the sample was measured. An area of $10\times 10\ \text{mm}^2$, which covers the whole sample, was mapped with the resolution of 64×64 pixels. Fig. 6.6 shows a resistivity map of the sample after polishing the surfaces with $0.3\ \mu\text{m}$ alumina abrasive (POL0.3).

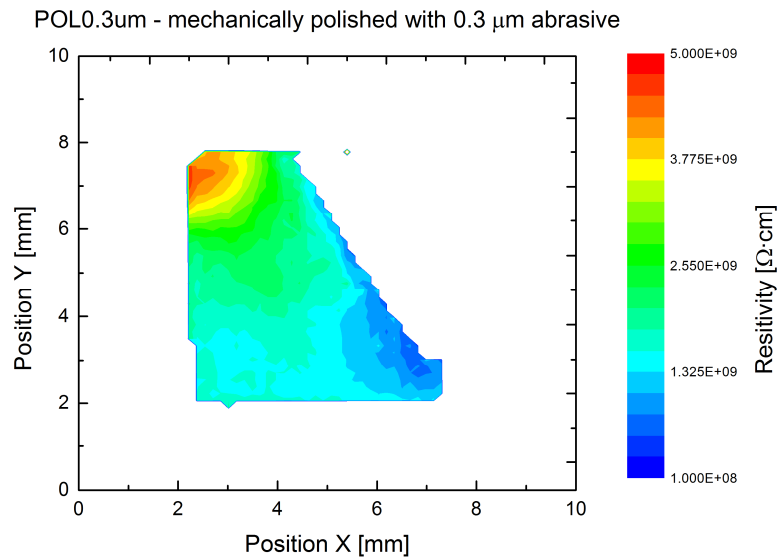


Fig. 6.6 Resistivity map of the sample CZT–V plane surface when polished with $0.3\ \mu\text{m}$ alumina abrasive.

The sample has high resistivity and its maximum and minimum values of the resistivity distribution lie on the edges of the sample. For polished and etched surface, the photoconductivity map was measured. The light source used for the photoconductivity measurements was a commercial L785P090 laser diode with a peak wavelength at 785 nm ($\approx 1.58\ \text{eV}$) with FWHM wavelength 20 nm and output power 90 mW at 120 mA operating current. This type of the diode was chosen because of the maximum power at a wavelength of the light close to the maximum of spectral dependence of photoconductivity. In this case, the light penetrates to such a depth below the surface, where the surface recombination is still negligible, but the electron–hole pairs are generated only several μm below the contact.

A representative photoconductivity map is shown in Fig. 6.7. Photoconductivity is calculated as the difference of reciprocal resistivity when illuminated and in dark, as described in chapter 3.2.

In the case of a polished surface with 1 μm alumina abrasive the photoconductivity is very homogeneous throughout the surface area.

By mapping the sample, statistical ensemble of point measurements throughout the surface preparations is obtained.

Comparing the values of resistivity of measured points between surface treatments, it can be observed that although there are some deviations the resistivity has a strongly correlated development, see Fig. 6.8 and Fig. 6.9.

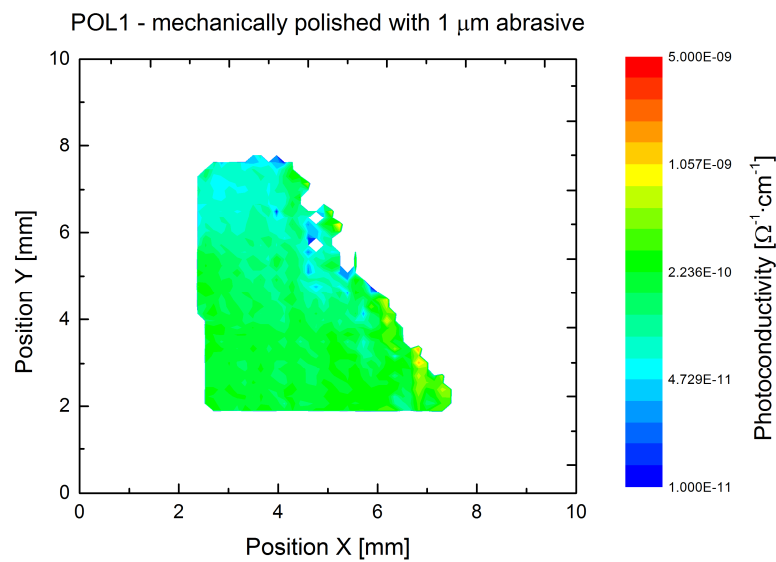


Fig. 6.7 Photoconductivity map of the sample CZT-V polished with 1 μm alumina abrasive. Illumination source was a laser diode with peak wavelength at 785 nm.

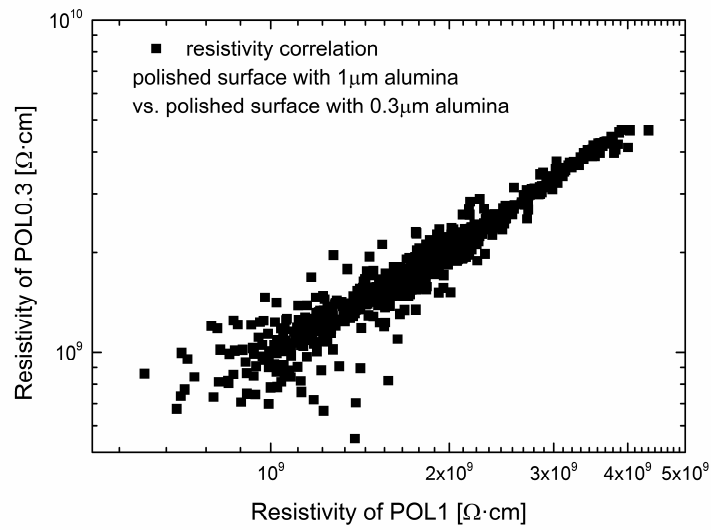


Fig. 6.8 Comparison of resistivity values of POL1 and POL0.3 treatments.

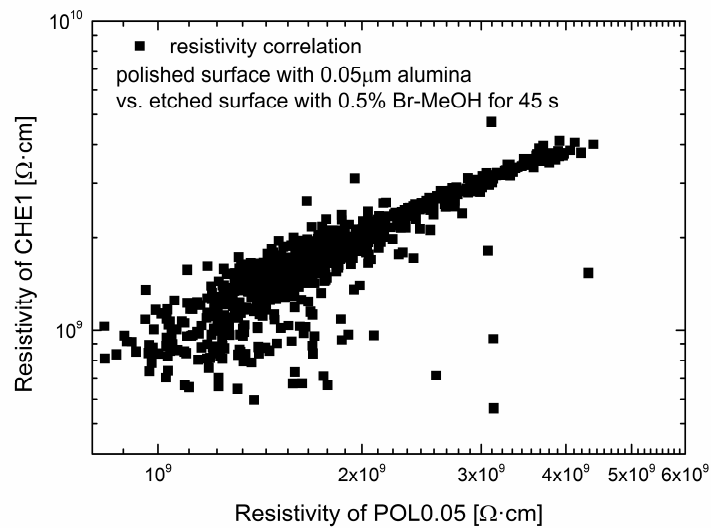


Fig. 6.9 Comparison of resistivity values of POL0.05 and CHE1 treatments.

The dependence of resistivity and photoconductivity on surface morphology can be investigated on each measured point of the CdTe sample. Because the resistivity is correlated between the treatments (see Fig. 6.8 and Fig. 6.9), the average values can be used as a representation of the sample with one surface preparation. Fig. 6.10 shows the development of the average resistivity after the different treatments.

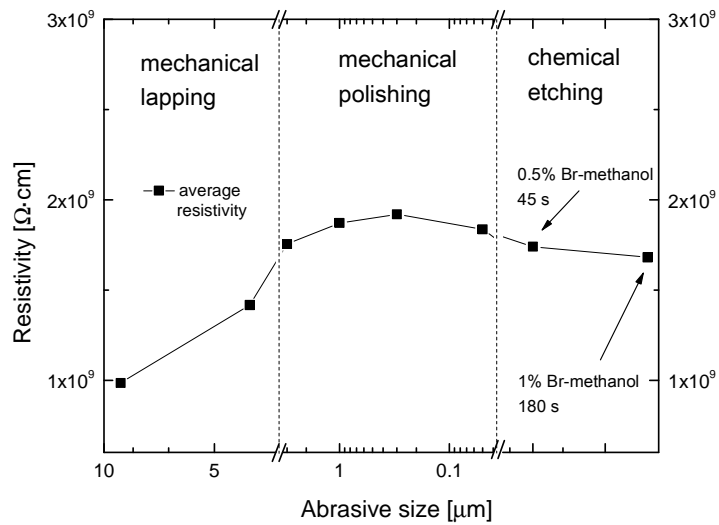


Fig. 6.10 Average sample resistivity dependence on surface preparation method.

The difference in the absolute value of resistivity can be up to 100%. Large increase of the resistivity is observed between LAP9, LAP4 and POL3. In the other treatments there are only slighter differences in the resistivity. The maximum average resistivity is observed for polished surface with $0.3 \mu\text{m}$ Al_2O_3 abrasive. With chemically etched surface, the average resistivity is about 20% smaller than that with POL0.3 treatment. Etching in stronger Br–methanol solution for longer time (CHE2) decreases the average resistivity even further. The average photoconductivity depending on the surface treatments is shown in Fig. 6.11.

The minimum average photoconductivity value is observed at polished surface with $0.3 \mu\text{m}$ abrasive. Other mechanically polished surfaces show higher values of photoconductivity, an anti–correlation with resistivity is observable. A great increase of photoconductivity was measured with the chemically etched surfaces. The difference to the polished surfaces is up to one order of magnitude.

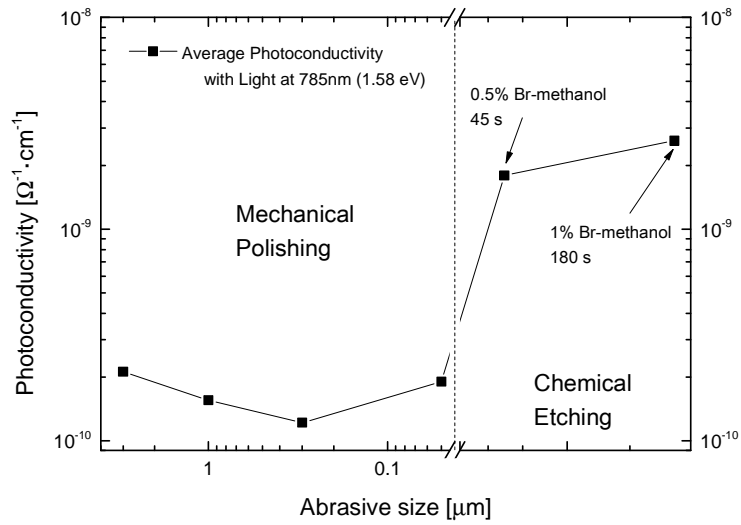


Fig. 6.11 Average sample photoconductivity dependence on the surface preparation method. The illumination source was a laser diode with peak wavelength at 785 nm.

To investigate the reason of the resistivity behavior, the sample treated with POL0.3 (maximum resistivity) and CHE1 was studied using X-ray photoelectron spectroscopy (XPS). Fig. 6.12 shows Te3d XPS spectra taken after two selected treatments. In a doublet structure of the Te3d region, there are two peaks corresponding to the Te elemental state (doublet at 572.5 and 582.9 eV) and two other peaks corresponding to the Te oxide state (doublet at 576.1 and 586.5 eV). The evaluated Te oxide/Te elemental atomic ratio drops rapidly from the value of 1.1 (treatment POL0.3) to 0.05 after the chemical treatment CHE1. The concentration of surface oxides thus diminished after chemical etching.

To support the results, further investigations of the sample were made using a spectroscopic ellipsometer to determine the thickness of the oxide layer on the sample surface after the treatments. Obtained experimental results were confronted with a simple theoretical model structure consisting of an oxide-damaged layer (containing TeO_2 oxide) on the CdZnTe bulk and the least square minimization was used to determine the surface layer thickness (listed in

Table 6.1).

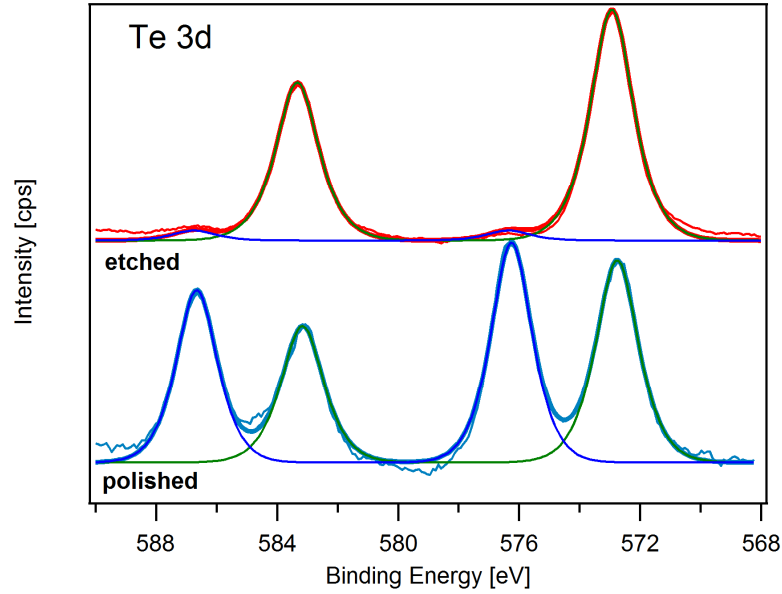


Fig. 6.12 *Te3d photoelectron spectra taken after two different treatments of CdZnTe sample. Te3d spectrum is composed of oxide (doublet at 576.1 and 586.5 eV) and elemental (doublet at 572.5 and 582.9 eV) components.*

The measured oxide thickness correlates with the surface roughness within the technological step of mechanical polishing of the sample. With lower RMS and less surface oxides the resistivity value increases up to its maximum at POL0.3. After chemical etching, fewer oxides are present on the surface with the higher roughness. This leads to lower values of resistivity. With the change of the surface oxide ratio upon chemical etching, the photoconductivity increases over an order of magnitude. This indicates that the oxide layer strongly decreases the photoconductivity of the material. The oxide thickness and its evaluation using spectroscopic ellipsometry measurement will be studied further in chapter 6.5.

The presence of a maximum in the resistivity dependence and a minimum in the photoconductivity dependence can be explained as a result of the influence of two independent effects.

With increased surface roughness (higher RMS) the evaluated resistivity decreases. This can be caused by the damaged layer introducing conducting channels into the semi-insulating material. On the other hand a thicker oxide layer was observed on surfaces with higher RMS results in a higher measured resistivity value. These two trends thus act in opposite directions and a maximum of resistivity in dependence on surface roughness (Fig. 6.10) can be seen. Overall the maximum value of average resistivity correlates with the smallest measured surface roughness.

The results of this study without contacts are in a general agreement with the research published in [90], where samples with Au contacts were investigated.

6.3. Surface effect on detector performance

As mentioned in chapter 6.1, sample CT-III was at first mechanically polished and consequently etched in Br-methanol solution to remove a surface damaged layer. Throughout these technological steps the map of resistivity and photoconductivity was measured. Fig. 6.13 shows the sample resistivity measurement at room temperature with a polished surface (initial state) and when a 10 μm surface layer was etched away. Average resistivity and photoconductivity with illumination above the bandgap was calculated as described in chapter 6.2 and is shown in Table 6.2. Upon etching, the sample resistivity changes and the photoconductivity using above bandgap light source (at ~ 1.77 eV) increases by almost one order of magnitude.

The detector properties of the sample were measured by α -spectroscopy with Am^{241} radiation source with both surface preparations (mechanical polishing and subsequent chemical etching), shown in Fig. 6.14. With polished surface a broader and smaller peak with low-energy tail and lower multi-channel-analyzer (MCA) channel is visible. In contrast to that, a narrow peak at higher energy is measured with the etched sample surface, concluding a better charge collection and detectivity of the sample when using chemical etching. The depreciation of the MCA channel maximum by ≈ 30 amounting to $\approx 3\%$ reduction of the collected charge in polished detector reflects the enhanced photo-carriers trapping and recombination in the surface damage layer. The low-energy tail points to existing regions with even much stronger damage represented by cracks and dislocation aggregates. This is consistent with results published in [83] and presented in the previous chapters 6.1 and 6.2, where resistivity dependence of CdZnTe material was studied. The influence of the used surface preparation type and method on the detector performance was investigated further in [8], [77], [91], [92] and the results support the evident importance of the surface treatment.

Surface preparation	Resistivity [$\Omega \cdot \text{cm}$]	Photoconductivity [$\Omega^{-1} \cdot \text{cm}^{-1}$]
Polished	$\sim 7.6 \cdot 10^8$	$\sim 5.2 \cdot 10^{-10}$
Etched – 10 μm	$\sim 8.6 \cdot 10^8$	$\sim 1.3 \cdot 10^{-9}$

Table 6.2 Average resistivity and photoconductivity values for sample No. 2 with different surface preparation.

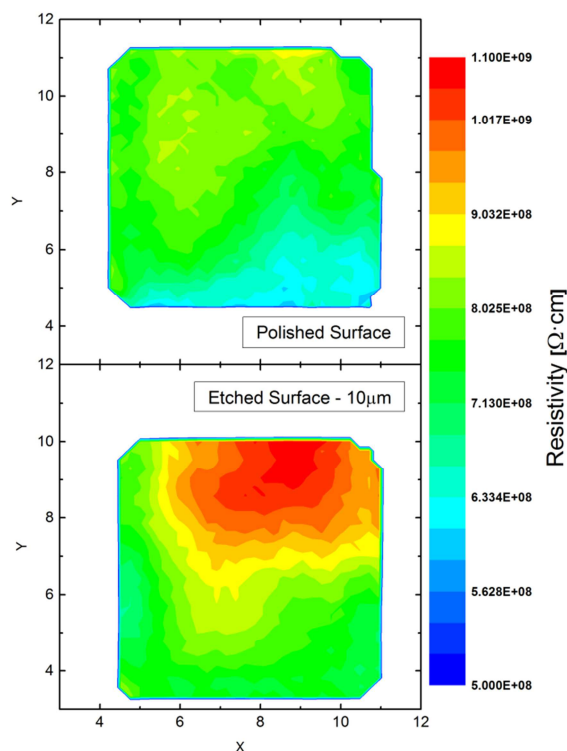


Fig. 6.13 Contactless resistivity of sample CT-III with two different surface preparations – a mechanically polished surface and surface after removal of 10 μm by etching.

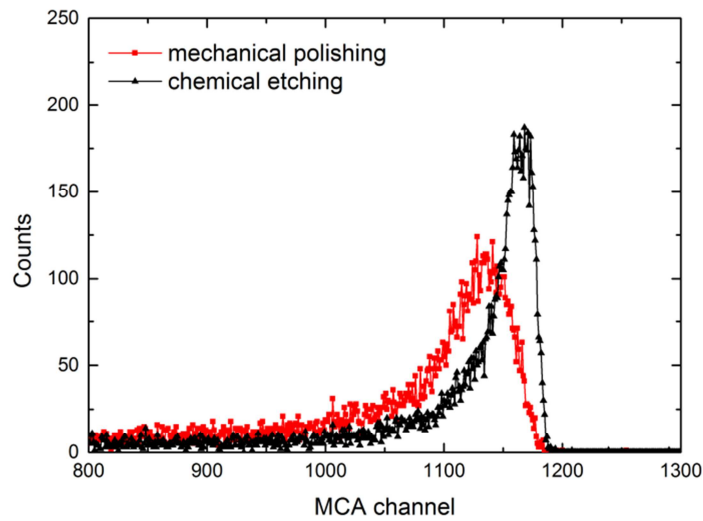


Fig. 6.14 *Detector performance measurement by α -spectroscopy at 300 V bias with mechanically polished surface (red dots) and consequently etched surface (black dots). The lines between points serve as guide only.*

6.4. Detailed investigation of contactless resistivity

From the results of chapters 6.2 and 6.3 it seems that the sample resistivity changes upon surface preparation. However, one must be careful in such a conclusion as the method used for the observations was the contactless resistivity mapping. This method has significant theoretical assumptions and by inspecting those, the results of the measurement can be clarified or better explained.

Contactless resistivity mapping employs the time dependent charge measurement, as presented by Stibal in [7]. It employs a simple model of the material being charged between two electrodes. The material charging should follow a simple exponential curve as calculated by evaluating the substitute electrical schema of the system. However, samples that do not follow this theory and their resistivity evaluation is affected with a certain error have been encountered. Previously (in chapter 6.2) it was mentioned that the evaluated resistivity after surface treatment was only “apparent” and the values were not necessarily the values of the bulk. The evaluated resistivity was the result of the best fit of the sample charging and can be influenced by surface layers. At this point, the charging of the

sample itself will be investigated and the encounter of non-standard charging behaviors will be reported.

The used method and experimental setup are described at the beginning of this thesis. It employs the dielectric properties of the material as described in [7]. The sample (resistance R_S and capacity C_S) is placed between two electrodes, laying on the bottom one while having an air gap (capacity C_A) between the top electrode and the sample. Evaluating the substitute electrical schema (see inset in Fig. 6.15) the charging should follow a simple exponential behavior, see Fig. 6.15.

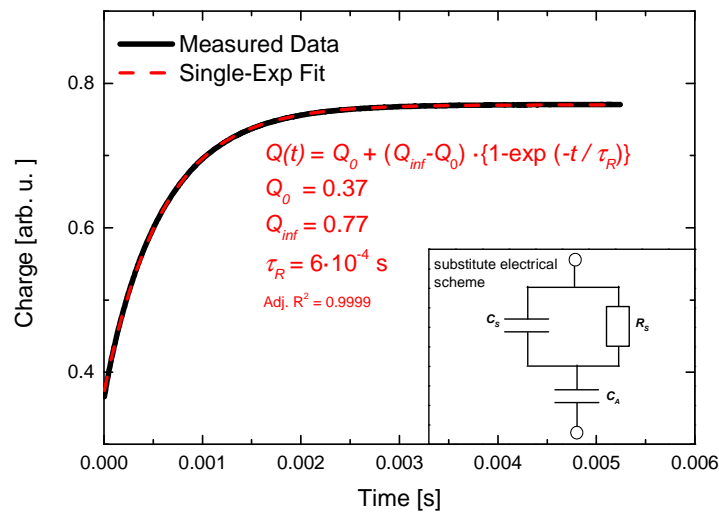


Fig. 6.15 Sample CdTe-IV following single-exponential charging according to [7].

Through fitting of the measured charge curve with the single-exponential theory, all parameters needed to evaluate the sample resistivity using the equation (3.3) are obtained. This way a bulk resistivity of the material is measured. Employing an x-y stage the resistivity distribution can be mapped.

Sample CdTe-IV follows the mono-exponential charging proposed by Stibal [7]. However, several CdTe and CdZnTe samples, all doped with indium, have been investigated and did not follow the theoretical curve. All of the samples were lapped and mechanically polished consequently using a smaller abrasive until the RMS value, measured via the Zygo interferometer, were about 2 nm. The sample charging curves were investigated using the COREMA setup. Some samples were then chemically etched or chemo-mechanically polished. Resistivity was measured after the surface preparation.

A representative sample CZT-II was chosen for the study of the charging characteristics. Resistivity at one point in the center of the sample was measured after mechanical polishing, see Fig. 6.16.

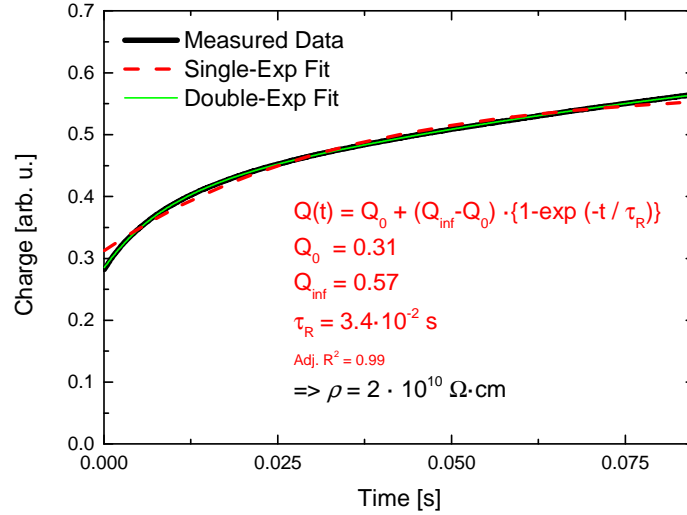


Fig. 6.16 Depiction of non mono-exponential charging of the sample.

The mono-exponential curve cannot be fitted correctly and the simple model of the substitute electrical schema does not describe the charging behavior. Two stages of charging are measured: fast component up to ≈ 15 ms and slow component from then on. This is well described using the double-exponential function

$$Q(t) = Q_0 + A_1 \cdot \left\{ 1 - \exp\left(-\frac{t}{\tau_{R1}}\right) \right\} + A_2 \cdot \left\{ 1 - \exp\left(-\frac{t}{\tau_{R2}}\right) \right\}, \quad (6.1)$$

However, this function does not have much physical meaning at this point.

The sample was chemically etched by immersion into a 3% Br-methanol solution for two minutes and consequently the charging characteristics were measured, see Fig. 6.17.

An apparent faster charging of the sample after etching, resulting in lower evaluated resistivity, is observed. Moreover a loss in the Q_{inf} value, which represents the total charge that is able to be deposited on the sample, is visible. The overall goodness of the fit has worsened, which can indicate that the change in the resistivity value can be attributed to surface modifications.

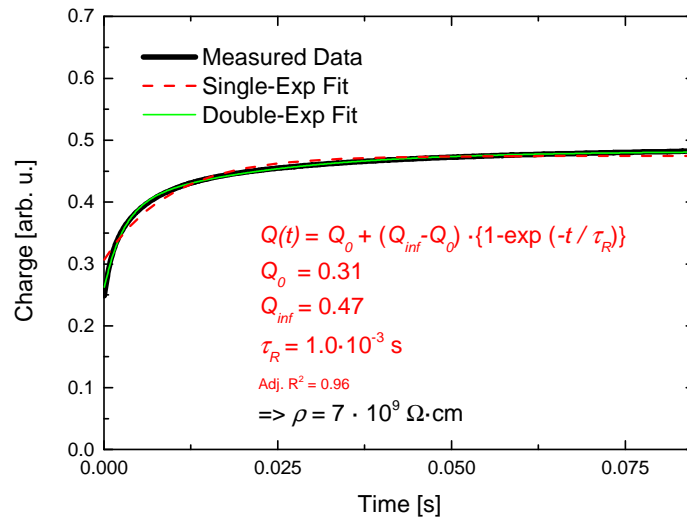


Fig. 6.17 Sample charging characteristics after surface modification by chemical etching.

The evaluated resistivity value is therefore only apparent and does not represent the accurate bulk resistivity. The deviation from the mono-exponential behavior is relatively small, but it can influence the absolute values of the evaluated resistivity. The dependence of the resistivity upon surface treatment, visible in Fig. 6.10, can reflect the deviations from the theoretical bulk charging and not the bulk resistivity itself. Nevertheless, even the deviations and goodness of fit dependence can show substantial changes in the surface of the sample, which have to be considered while preparing the final CdTe detector.

The changes in the sample behavior upon surface manipulation are usually attributed to a development of a damaged layer and oxide layer growth. Changes in the photoluminescence spectra and charge collection efficiency between polished and etched samples have also been presented in the previous chapters.

The charge characteristics were further investigated in time dependence after the surface etching. For a better depiction of the time influence the relaxation parameter τ_R as a function of time after etching was evaluated, see Fig. 6.18.

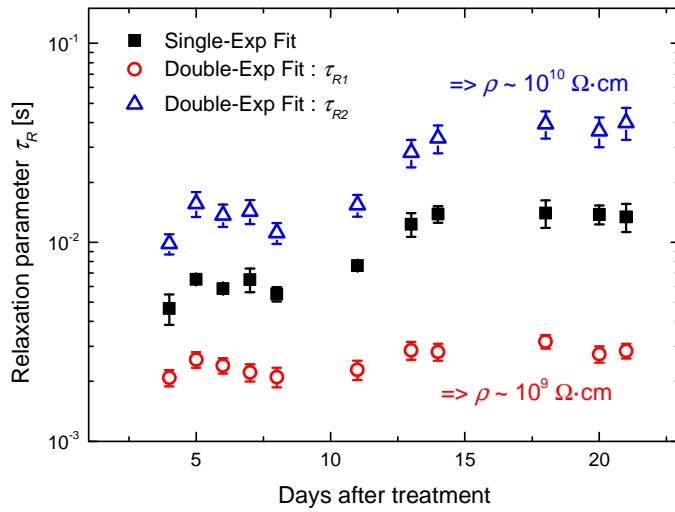


Fig. 6.18 Time evolution of relaxation parameter τ_R after surface treatment.

An increase of the relaxation parameter value in time, when evaluating with the mono-exponential model, is observed. The parameter is almost doubled after 20 days. While evaluating using the double-exponential fitting, the faster component (connected with resistivity value $\sim \rho = 1 \cdot 10^9 \Omega \cdot \text{cm}$) remains relatively stable within 20 days after etching, whereas the slower component (connected with resistivity value $\sim \rho = 1 \cdot 10^{10} \Omega \cdot \text{cm}$) value increases in time. This is then reflected as a resistivity increase, when evaluating with the mono-exponential theory. With the assumption of a dielectric oxide layer growth on the sample surface, the slower component can be attributed to this growth. The surface oxide is a dielectric and has a higher resistivity than the sample bulk. The faster component seems to be connected with the bulk of the sample. However, the correct bulk resistivity in this case is not the value $\rho = 1 \cdot 10^9 \Omega \cdot \text{cm}$. The double-exponential evaluation is also not correct and only serves to fit the experimental data and to investigate the behavior. It points out that the actual contactless resistivity measurement can be influenced by surface preparation and that the evaluated resistivity serves only as an “apparent” value. Nevertheless, the values of resistivity upon surface treatment change almost only within one order of magnitude. In this case the correct resistivity value is thought not to be very different from the evaluated one. It is possible to operate with the single-exponentially evaluated resistivity values. But in that case, it is necessary to assume that they are charged with some measurement error.

The surface layer of the sample (consisting of damaged and oxide layers) induces charge occupation changes. Different charge can be placed onto the sample with variously thick oxide layers. These changes also influence the resistivity measurement. Sample CT–IV was further studied with metal contacts deposited onto the large planes. The contact material was gold (Au) and indium (In), both of them were deposited through thermal evaporation. The contacts induce bending of the valence and conduction bands. Fig. 6.19 shows measurements in two different arrangements, either the gold contact faces the top electrode (Au on Top) or the indium contact does. The two metals cause different band bending. Fig. 6.19 shows similar double–exponential behavior of the sample charging as the measurement without contacts. This concludes that the surface states achieved through mechanical and chemical sample preparations can induce band bending similar to the case with the metal contact deposition.

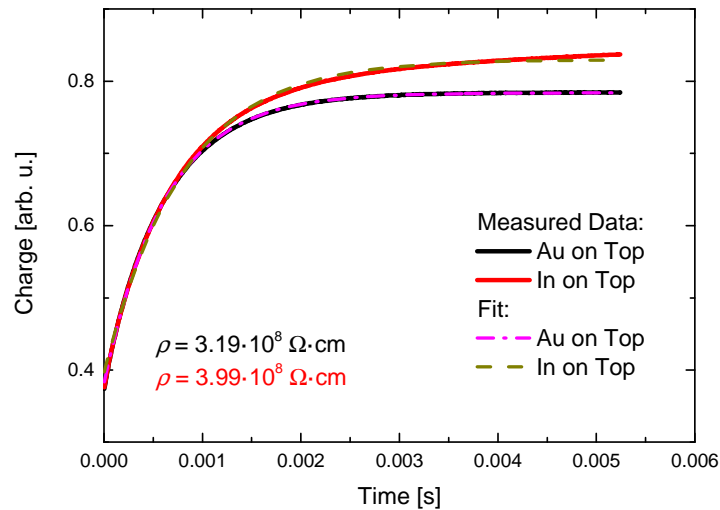


Fig. 6.19 Sample charging characteristics with metals deposited onto the surface.

Using the contactless resistivity measurement, the goodness of fit must also be studied to evaluate the measurement error of the surface preparation. For an exact charge characteristics evaluation, a new theory with a modified sample structure must be investigated. When counting–in the sample surface, the new structure must consist of the bottom electrode, bottom sample surface oxide layer, sample bulk, top sample surface oxide layer, and air gap, see Fig. 6.20.

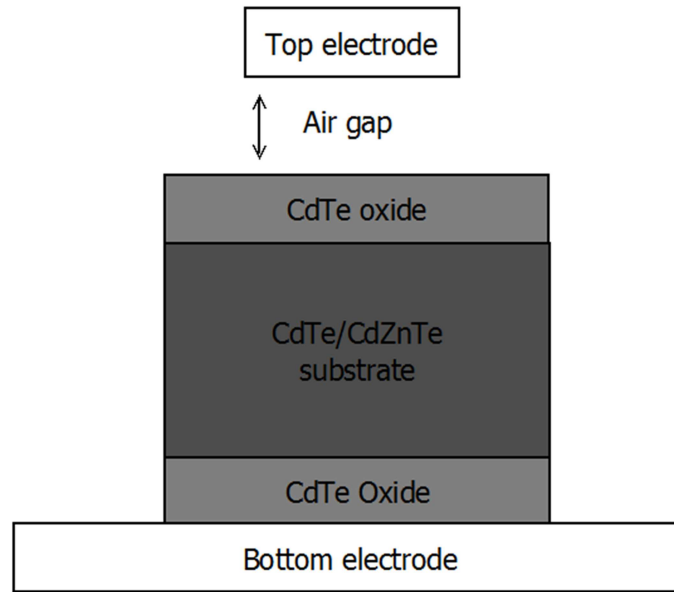


Fig. 6.20 Proposed corrected structure for evaluation of contactless resistivity measurement.

6.5. Surface oxide thickness and growth

On several occasions time evolution of the leakage current and of the detector quality was observed [70], [77] as it was presented in the previous chapter. The sample evolution has been attributed to oxidization of the detector surface. Even without any passivation a thin layer of oxide grows on the CdTe surface when exposed to ambient air. Already published XPS results suggest that the oxygen is almost exclusively bound to tellurium [70], [93], forming a layer consisting of mainly TeO_2 and CdTeO_3 . Several studies have been made employing spectroscopic ellipsometry to evaluate the surface layer thickness in dependence on preparation techniques used and on the oxide atomic ratio obtained by XPS measurements [94]–[96]. However, a systematic study of the dynamics of native oxide formation and oxide layer thickness evolution with respect to the time after the surface treatment has not been reported yet. The knowledge of this dynamics may help to better understand the process of the surface oxide formation, which is crucial for the development of a suitable surface treatment technique and to ensure a long time functional stability of the detectors. This chapter presents a systematic study of the evolution of the surface oxide layer thickness on various CdTe and CdZnTe samples, with respect to the time (up to 30 days) after the sample treatment.

Two CdTe samples (CT-I and CT-III) and two CdZnTe sample (CZT-III, CZT-IV) were used for this investigation. For sample parameters see

Table 3.1 and

Table 3.2.

All samples, except of CZT-IV, had no contacts. The side with the largest surface area was used in the measurements. All samples were chemo-mechanically polished on a silk pad using a 3% Br-ethylenglycol solution for 60 seconds. Afterwards they were chemically etched by immersion into a 3% Br-methanol solution for 60 seconds. On average 20 μm off the top of each sample were removed after the chemical polishing and etching, which was measured by a digital indicator with the resolution of 1 μm . The samples were kept on ambient air at room temperature after the surface treatment and between measurements.

The optical response of the samples by spectroscopic ellipsometry with respect to the time after etching was studied. A proper theoretical model structure must be devised and used for the fitting of the experimental data. Through measurement evaluation, spectrally dependent optical properties of investigated material as well as the thickness of the surface oxide layer can be derived. In the presented case the model structure consisted of a semi-infinite bulk CdTe material with the surface oxide layer of a certain thickness and roughness. An assumption of semi-infinite CdTe is justifiable owing to its high absorption coefficient in the investigated spectral region and a large thickness of the sample with respect to the surface layer. Sample CZT-IV was selected for electrical IV measurements and their correlation with the oxide evolution. Gold contacts were chemically deposited at the $4 \times 2 \text{ mm}^2$ lateral sides of this sample by immersion into an aqueous AuCl_3 solution for one minute.

Ellipsometry was measured in reflection for three incident angles $\Phi = 55^\circ$, 60° and 65° , respectively. The use of variable-angle-spectroscopic-ellipsometry (VASE) was necessary to determine the surface layer thickness with good accuracy. Fig. 6.21 shows a typical evolution of parameters Ψ and Δ with time after the surface treatment. The incident light spot diameter was 4 mm. In this case, practically most of the sample was illuminated and the gathered information was averaged over the whole surface. From Fig. 6.21 one can see a significant impact of time on the spectra of the Δ parameter. Since Δ describes the phase shift of the light wave

induced by the reflection on the sample, the change of this parameter during time suggests certain changes at the surface.

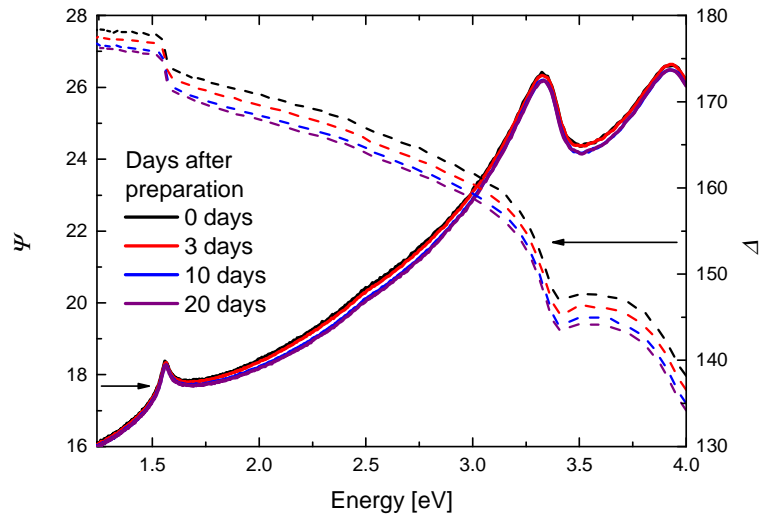


Fig. 6.21 Evolution of ellipsometric parameters Ψ (full lines) and Δ (dashed lines) for Sample 3 after the surface treatment. The data were acquired at incident angle of 60° .

To justify the assumption of the oxide layer growth, XPS was measured on Sample CZT-IV and the results are shown in Fig. 6.22. Te3d spectra were measured after the initial preparation by mechanical polishing – red line in Fig. 6.22. A peak doublet of elemental tellurium is visible at energies 573 eV and 583 eV, marked as “elemental”. Another peak doublet related to the oxygen bound to tellurium is also visible in Fig. 6.22, marked as “oxide”. Because the doublet shift is about 3.3 eV, the measurement indicates a formation of the TeO_2 layer [95], [97]. Then the sample was chemically etched and the XPS experiment was performed again within an hour after the etching. The XPS spectrum shows no signal of oxygen bound to tellurium – green line in Fig. 6.22. After three weeks of exposure of the sample to ambient air XPS was measured again (see Fig. 6.22, line c). The spectra showed oxidization of the sample. The peaks of oxygen bound to tellurium were clearly visible. This way a formation of an oxide surface layer after keeping the sample three weeks on ambient air at room temperature was confirmed.

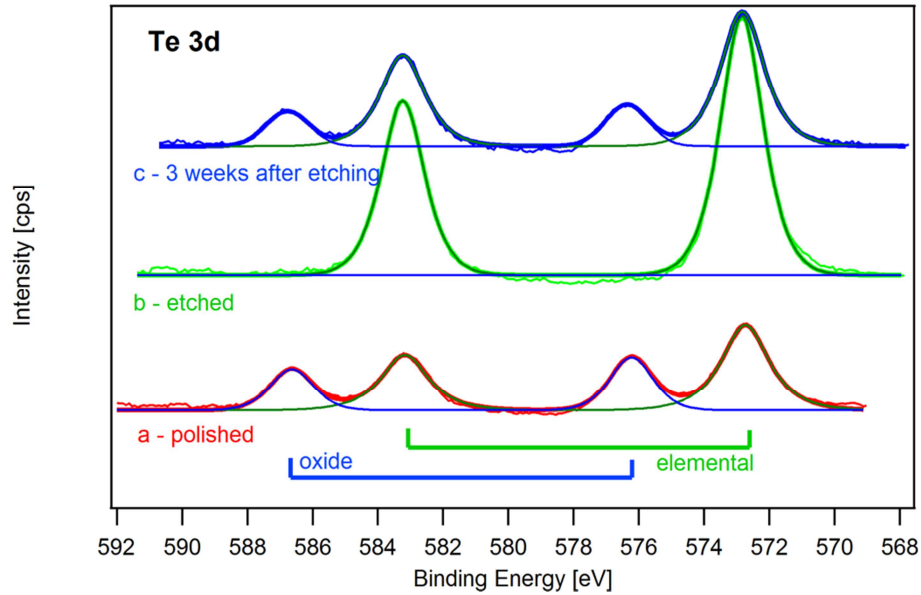


Fig. 6.22 XPS spectra of CZT–IV (a) for mechanically polished surface, (b) surface etched with Br–methanol within an hour after the preparation and (c) three weeks after chemical etching. The ratio of oxygen bound on tellurium to elemental tellurium is (a) 0.55, (b) 0.02 and (c) 0.30, showing that the damaged layer after the mechanical polishing which contains oxygen can be removed by etching in Br–methanol; three weeks after etching the oxide layer bound to tellurium is again established.

The growth of the surface oxide layer and the correlation between the oxide thickness evaluated with ellipsometry and “oxide” peak height and width in XPS was proven already by Badano *et al.* [95]. However, a detailed insight into the dynamics and the growth rate after the chemical preparation has not been published yet. This study concentrates on the evaluation of the oxide layer thickness in time after etching. It is focused on determining the impact of air exposure of the CdTe/CdZnTe samples during the fabrication process on the thickness of the surface oxide layer. To evaluate the thickness of the oxide layer the experimental data had to be confronted with a theoretical model of the surface structure. Yao *et al.* [94] used a simple layer of CdTe–oxide and an intermix of the CdTe–oxide and void on a CdTe substrate. Badano *et al.* [95] used a more complicated structure consisting of the substrate, intermix layer, metallic tellurium layer, oxide layer, and surface roughness. Both approaches were tried and investigated, but the resulting fits of experimental data were not of a sufficient level. After implementing these models in the experimental data processing, a compromise mix of both approaches was selected and a model with three components – the semi–infinite CdTe bulk, the layer

consisting of bulk CdTe and the oxide layer, described by effective-medium-approximation (EMA), and the surface roughness layer, was proposed. The schema of the model is shown in Fig. 6.23.

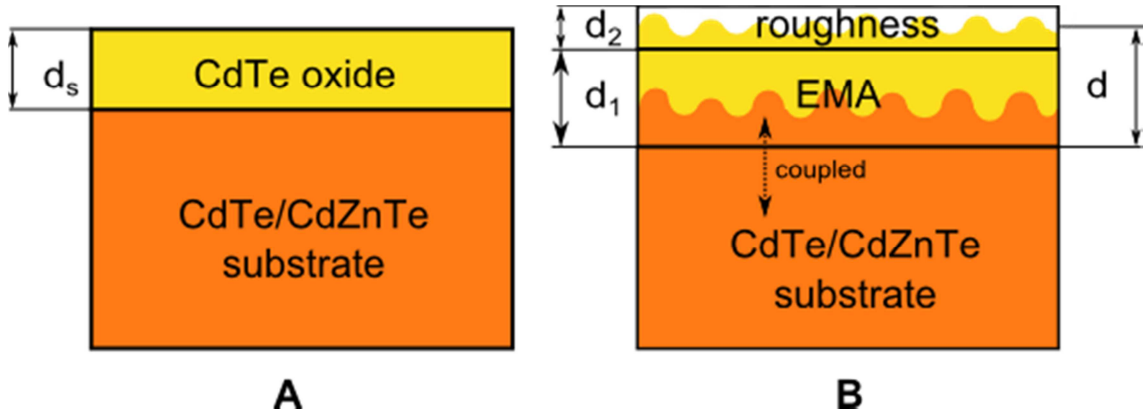


Fig. 6.23 Theoretical model – A: simple model (not used in our evaluation), B – the used model with an effective-medium-approximation (EMA): coupled substrate and CdTe oxide.

In EMA the optical constants of the consisting materials are mixed with the ratio from 0 to 100%. This approach practically substitutes a non-uniform surface layer with material peaks and trenches. Moreover, the optical parameters of bulk CdTe material were coupled to the parameters used in the EMA layer. The idea was that the CdTe bulk itself has a non-uniform surface and the oxide layer grows upon its roughness. The angular spread on the sample surface was also taken into account. To fit the experimental data, the CompleteEASE software was used. The initial optical parameters of bulk CdTe and of the CdTe oxide were taken from the database supplied by Woollam Co. Inc. The CdTe bulk was parametrized using Lorentz oscillators and the CdTe oxide was parametrized with the Cauchy approximation. The experimental data were analyzed using Multi-Sample-Analysis (MSA). In the studied case the analysis consisted of multiple measurements performed on each sample with respect to the time after the surface treatment. The optical parameters of the bulk and of the EMA layer were set the same for the whole data ensemble. Only the composition ratio of the EMA, the thickness of the EMA layer d_1 and the roughness d_2 could change individually in each measurement. In Fig. 6.24 the scatter points show measured data of sample CZT-IV and the full lines represent the fit using the model structure described above.

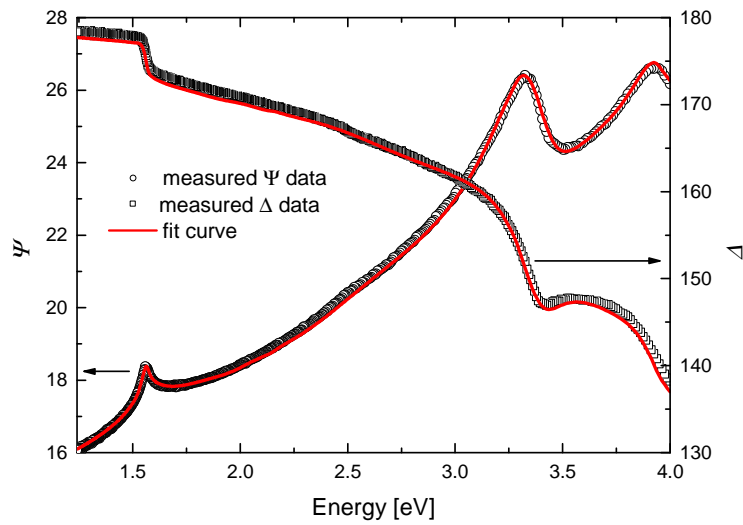


Fig. 6.24 Representative plot of the fitting of measured data. The scatter points represent the data measured on sample CZT–IV right after surface preparation. The full red lines demonstrate the fit agreement with the measurement. Selected dataset had the highest MSE, remaining fits showed even better fit reliability.

Because of the interface roughness between the bulk and the oxide layer, the overall surface layer thickness as the thickness of the EMA layer d_1 and a half of the roughness d_2 ($d = d_1 + 0.5 \times d_2$) was evaluated, as shown schematically in Fig. 6.23–B. The time evolution of the surface layer thicknesses for all samples is shown in Fig. 6.25. CdTe samples exhibit almost no surface layer right after the surface treatment, whereas CdZnTe samples show surface layer with thickness around 0.5 nm right after the surface etching. The presence of the surface oxide layer right after the surface treatment in CdZnTe samples is necessary to achieve the best MSE of the fit. Interestingly, this is only necessary with the CdZnTe samples. On the other hand, in CdTe samples the presence of the initial oxide layer is not necessary to achieve the fit with similar MSE. Therefore, one can conclude that the CdZnTe samples have a fast initial oxidation of the surface compared to CdTe samples.

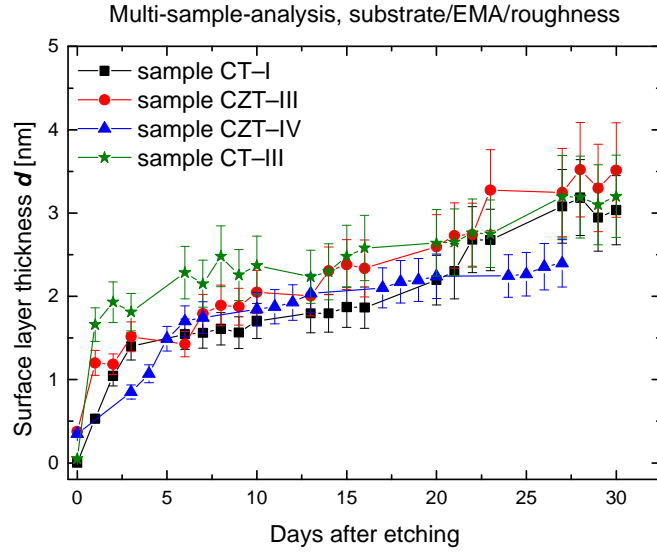


Fig. 6.25 Time dependent surface layer thickness d after the surface preparation treatment.

The growth rate of the surface layer on all samples within one month is visible in Fig. 6.25. A semi-saturation of the surface layer growth can be seen in about 5 days for all of the samples. Within these first 5 days a fast oxidation of the surface occurs and is slowed afterwards. Within one month after the chemical treatment, all the samples show about 3 nm thick surface layer. The fit error increases with larger layer thicknesses. This can indicate that the parameters of the theoretical model can vary, e.g. the evaluation program cannot decide whether a layer thickness should increase or the optical parameters (index of refraction and extinction coefficient) of the layer are changing, so that the layer becomes more absorbent. In the evaluation the oxide layer optical parameters were kept constant in the whole evolution datasets. Even so, the dynamics of the oxide layer growth is clearly visible. It was also found that within the first growth phase (up to 5 five days) the evolution of the EMA layer thickness d_1 has the greatest contribution to the surface layer thickness d . After the semi-saturation both the EMA layer thickness d_1 and the surface roughness d_2 are increasing similarly. The reason of the increase in roughness might be attributed to mechanical stress and lattice mismatch of the oxide layer, resulting in non-uniform columnar surface structure.

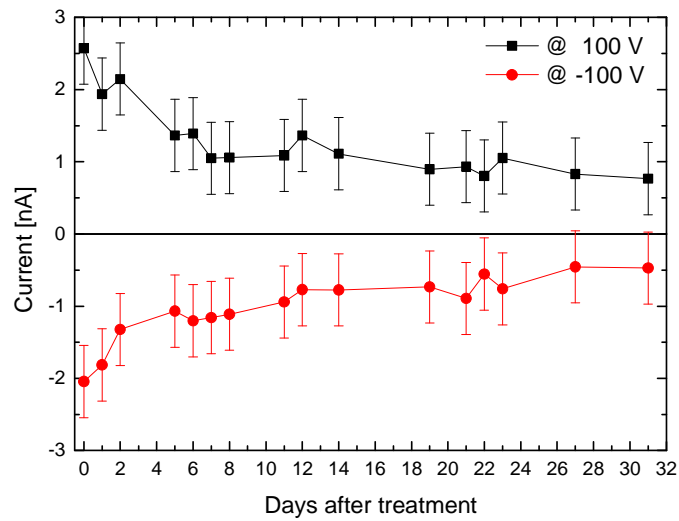


Fig. 6.26 Current evolution of sample CZT-IV biased at 100 V (both polarities) with time after the chemical etching. Lines between measurements serve as guidelines only.

The IV characteristics of sample CZT-IV were measured and correlated with the surface layer thickness evolution. Fig. 6.26 and Fig. 6.27 show the evolution of the measured current within 31 days after the surface treatment. The current through the sample relaxes over the time towards lower values. The semi-saturation after about five days is also clearly visible. The conclusion follows that the thicker surface layer influences the detector by passivating the lateral sides and decreases the leakage current, because the decreased current values correlate with thicker surface layer evaluated from ellipsometry.

While determining the surface layer thicknesses, the optical parameters of the bulk CdTe and CdZnTe were also evaluated and are shown in Fig. 6.28.

Fig. 6.28 shows the absorption edge moving towards higher energies in the samples with higher zinc concentrations. This is in agreement with theoretical predictions and another measurements [4], and indicates the correctness of the data fitting.

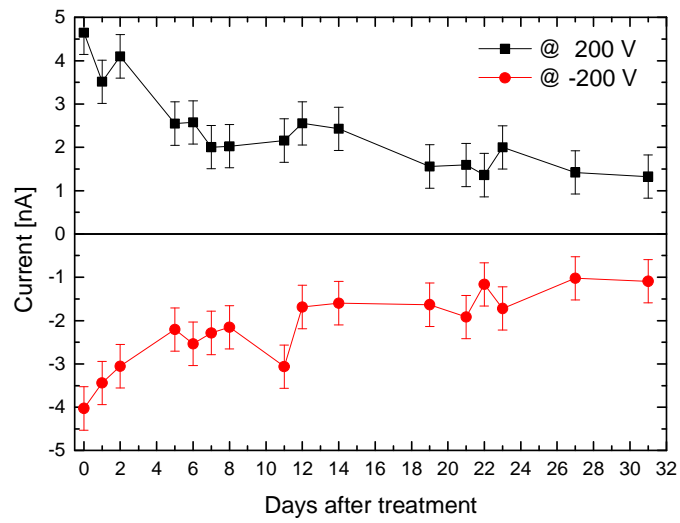


Fig. 6.27 Current evolution of sample CZT-IV biased at 200 V (both polarities) with time after the surface treatment. Lines between measurements serve as guidelines only.

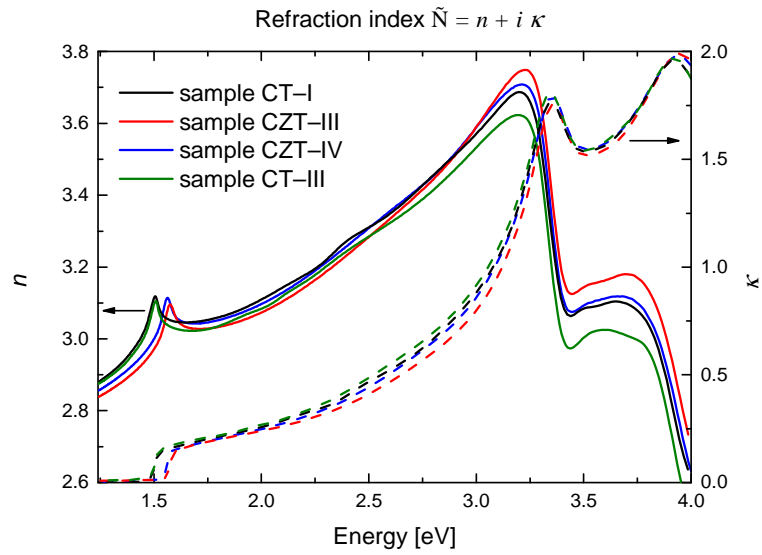


Fig. 6.28 Optical parameters of bulk part of the investigated samples determined by VASE.

6.6. Chapter summary

The effects of surface treatment on the final CdTe and CdZnTe detector were investigated. The changes in the deep level PL spectra upon mechanical and chemical etching point to a more pronounced defect with surface polishing. Changes in the resistivity and photoconductivity with different sample treatments were attributed to the effect of damaged layer and surface oxidation. The mechanical polishing influence on α -spectroscopy was established. The growth rate and thickness of TeO₂ layer formed in time after chemical etching of the sample was measured and correlated with the decrease of the leakage current flowing through the detector. The influence of the oxide formation on the contactless resistivity measurement was investigated. The oxide layer, serving as a passivation, affects the charging of the detector sample and disturbs the evaluation of the resistivity using the COREMA system. The correlation between changes in the charging parameters and the oxide growth was observed.

7. Conclusions

The detector preparation process can be divided into three stages: semiconductor crystal growth and characterization, surface preparation and detector performance. All the stages have been investigated in detail in focus on the influence on the final spectroscopic device. Various CdTe and CdZnTe samples have been investigated through contactless resistivity mapping, photoluminescence measurement, laser-induced transient-current-technique and IV characteristics in dependence on material type, quality and surface preparation.

After the growth process the structure of the bandgap and the influence of impurities and defects were investigated through optical measurement. The structure of the photoluminescence signal in the region of 1.1 eV was studied. The deep level in the vicinity $E_C - 1.1$ eV was previously found to have a great influence on the polarization and the functionality of the radiation detector. However, it was found that the deep level $E_{DLI} = E_C - 1.1$ eV seems to have a rather complex structure. With extensive luminescence measurement of excitation and temperature dependencies, three distinct deep levels were found in the region around 1.1 eV. The three levels have energies 1.19 eV, 1.13 eV and 1.03 eV, respectively. Though the analysis does not give the answer of the origin of these deep levels, their structure and possible connection to already investigated published defects is given. The measured data of CdTe were compared with measurement of CdZnTe, where the deep level structure and its behavior are rather poor. Comparison with the already published studies has been made and commented.

For the investigation of detector performance, material resistivity and photoconductivity was compared with photoluminescence measurement. Correlation and anti-correlation of the studied physical quantities were explained using theory of the Fermi level shift inside the bandgap. Concentration changes of a near midgap deep level influence the charge compensation conditions and results in the Fermi level shift. This has a further effect on the material photoconductivity and space charge formation in the detector. The evaluated data were confronted with a theoretical model and calculations. Impact of the deep levels on the detector performance was established. Resistivity was also correlated to mobility of charge carriers studied through transient-current-technique measurement.

With CdTe and CdZnTe the surface preparation was found to be crucial for optimal detector performance. Resistivity and leakage current were investigated in dependence on the surface preparation and on the time after the final preparation step. Resistivity changes with different mechanical and chemical processes were attributed to the competition of two effects: surface damaged layer thickness and surface oxide thickness. These effects can change the sample resistivity by a small amount, but greatly influence the photoconductivity and illumination response, proving to be vital in the detector performance.

Surface influence was investigated through XPS, IV characteristics and optical ellipsometry measurement. With ellipsometry a theoretical model for measurement evaluation was proposed. The native oxide layer thickness and growth rate was determined in dependence on time after chemical etching of the sample. The layer growth was correlated with leakage current measurement and concludes that the surface layer thickness decreases the leakage current and stabilizes the detector in the signal-to-noise ratio. Native oxide growth was compared to purposefully oxidized surface and seems to have similar effect.

The contactless resistivity measurement was confronted in the sight of oxides formation on the material surface. Theoretically the contactless measurement calculates only with one bulk material of a single response to electric bias application. In real conditions, having a sandwich structure of oxide-bulk-oxide results in a non-linear charge transport through the sample. The consequence to this is the non-exponential charging character of the detectors in the contactless resistivity measurement which can be falsely evaluation into an incorrect resistivity value. This has been investigated and an explanatory theoretical model was devised.

Summarizing the results from different characterization methods a revised approach to detector preparation for a better detector performance is suggested: Homogeneous material with a stable spatial concentration of the midgap deep is optimal for preparation of radiation detectors. After mechanical surface treatment the sample should be etched. Afterwards it should be waited approximately five days for the surface oxide layer to be formed and the leakage current decrease to be saturated.

A comprehensive study of the spectroscopic high energy radiation CdTe-based detector development was made.

References

- [1] B. Sapoval and C. Hermann, *Physics of Semiconductors*. Springer-Verlag New York Inc., 1995.
- [2] R. B. James and T. E. Schlesinger, *Semiconductors for room-temperature nuclear detector application*. San Diego: Academic Press, 1995.
- [3] P. Horodysky and P. Hlidek, “Free-exciton absorption in bulk CdTe: Temperature dependence,” *Phys. Status Solidi* **243**, 2006, p. 494–501.
- [4] J. Franc, R. Grill, P. Hlidek, and P. Horodysky, “Mapping of Zinc Content in Cd_{1-x}Zn_xTe by Optical Methods,” *J. Electron. Mater.* **35**, 2006, p. 1491–1494.
- [5] J. Franc, L. Sedivy, E. Belas, M. Bugar, J. Zazvorka, J. Pekarek, S. Uxa, P. Hoschl, and R. Fesh, “Melt growth and post-grown annealing of semiinsulating (CdZn)Te by vertical gradient freeze method,” *Cryst. Res. Technol.* **48**, 2013, p. 214–220.
- [6] J. Franc, V. Dedic, M. Rejhon, J. Zazvorka, P. Praus, J. Tous, and P. J. Sellin, “Control of electric field in CdZnTe radiation detectors by above-bandgap light,” *J. Appl. Phys.* **117**, 2015, p. 165702.
- [7] R. Stibal, J. Windscheif, and W. Jantz, “Contactless evaluation of semi-insulating GaAs wafer resistivity using the time-dependent charge measurement,” *Semicond. Sci. Technol.* **6**, 1999, p. 995–1001.
- [8] L. Marchini, A. Zappettini, E. Gombia, R. Mosca, M. Lanata, and M. Pavesi, “Study of surface treatment effects on the metal-CdZnTe interface,” *IEEE Trans. Nucl. Sci.* **56**, 2009, p. 1823–1826.
- [9] G. F. Knoll, *Radiation Detection and Measurement*. John Wiley & Sons, Ltd, 2000.
- [10] A. I. Anselm, *Introduction to semiconductor theory*. Praha: Academia, 1967.
- [11] C. Kittel, *Introduction to Solid State Physics*. Praha: Academia, 2004.
- [12] A. G. Milnes, *Deep impurities in semiconductors*. New York: Wiley, 1973.
- [13] A. Castaldini, A. Cavallini, B. Fraboni, P. Fernandez, and J. Piqueras, “Deep energy levels in CdTe and CdZnTe,” *J. Appl. Phys.* **83**, 1998, p. 2121.
- [14] X. Mathew, “Photo-induced current transient spectroscopic study of the traps in CdTe,” *Sol. Energy Mater. Sol. Cells* **76**, 2003, pp. 225–242.

- [15] D. de Nobel, "Phase Equilibria and Semiconducting Properties of Cadmium Telluride," *Philips Res. Reports* **14**, 1959, p. 361–399.
- [16] S. Gurumurthy, K. S. R. K. Rao, A. K. Sreedhar, H. L. Bhat, B. Sundershesu, R. K. Bagai, and V. Kumar, "Influence of deviation from stoichiometry on the photoluminescence in CdTe doped with indium," *Bull. Mater. Sci.* **17**, 1994, p. 1057–1064.
- [17] K. Guergouri, N. Brihi, Y. Marfaing, and R. Triboulet, "Optical study of interactions of hydrogen with dislocations in CdTe," *J. Cryst. Growth* **256**, 2003, p. 230–236.
- [18] P. Fernandez, "Defect structure and luminescence properties of CdTe based compounds," *J. Optoelectron. Adv. Mater.* **5**, 2003, p. 369–388.
- [19] V. Babentsov, V. Boiko, G. A. Schepelskii, R. B. James, J. Franc, J. Prochazka, and P. Hlidek, "Photoluminescence and electric spectroscopy of dislocation-induced electronic levels in semi-insulated CdTe and CdZnTe," *J. Lumin.* **130**, 2010, p. 1425–1430.
- [20] N. Zambelli, L. Marchini, G. Benassi, D. Calestani, and A. Zappettini, "Modification of the luminescence properties of CZT crystals around tellurium inclusions," *IEEE Trans. Nucl. Sci.* **59**, 2012, p. 1526–1530.
- [21] K. H. Kim, J. H. Choi, A. E. Bolotnikov, G. S. Camarda, A. Hossain, G. Yang, Y. Cui, and R. B. James, "New insight into the 1.1-eV trap level in CdTe-based semiconductor," *J. Korean Phys. Soc.* **62**, 2013, p. 623–627.
- [22] A. A. Pruchkina, N. S. Nikolaev, V. S. Krivobok, V. S. Bagaev, E. E. Onishchenko, Y. V. Klevkov, and S. A. Kolosov, "Effect of annealing in liquid cadmium upon photoluminescence in polycrystalline cadmium telluride grown under nonequilibrium conditions," *Semiconductors* **48**, 2014, p. 292–298.
- [23] Z. Sobiesierski, I. M. Dharmadasa, and R. H. Williams, "Correlation of photoluminescence measurements with the composition and electronic properties of chemically etched CdTe surfaces," *Appl. Phys. Lett.* **53**, 1988, p. 2623–2625.
- [24] K. H. Kim, A. E. Bolotnikov, G. S. Camarda, A. Hossain, R. Gul, G. Yang, Y. Cui, J. Prochazka, J. Franc, J. Hong, and R. B. James, "Defect levels of semi-insulating CdMnTe:In crystals," *J. Appl. Phys.* **109**, 2011, p. 113715.
- [25] N. Armani, C. Ferrari, G. Salviati, F. Bissoli, M. Zha, and L. Zanotti, "Crystal

- defects and optical transitions in high purity, high resistivity CdTe for device applications,” *Mater. Sci. Eng. B Solid-State Mater. Adv. Technol.* **91–92**, 2002, p. 353–357.
- [26] J. Zazvorka, J. Franc, P. Hlidek, and R. Grill, “Photoluminescence spectroscopy of semi-insulating CdZnTe and its correlation to resistivity and photoconductivity,” *J. Lumin.* **143**, 2013, pp. 382–387.
- [27] W. Stadler, D. M. Hofmann, H. C. Alt, T. Muschik, B. K. Meyer, E. Weigel, G. Muller-Vogt, M. Salk, E. Rupp, and K. W. Benz, “Optical investigations of defects in Cd_{1-x}Zn_xTe,” *Phys. Rev. B* **51**, 1995, p. 10619–10630.
- [28] R. C. Bowman and D. E. Cooper, “Detection of dilute iron impurities in CdTe,” *Appl. Phys. Lett.* **53**, 1988, p. 1521.
- [29] J. Krustok, V. Valdna, K. Hjelt, and H. Collan, “Deep center luminescence in p-type CdTe,” *J. Appl. Phys.* **80**, 1996, p. 1756–1762.
- [30] P. Emanuelsson, P. Omling, B. K. Meyer, M. Wienecke, and M. Schenk, “Identification of the cadmium vacancy in CdTe by electron paramagnetic resonance,” *Phys. Rev. B* **47**, 1993, p. 15578–15580.
- [31] D. Verstraeten, C. Longeaud, A. Ben Mahmoud, H. J. Von Bardeleben, J. C. Launay, O. Viraphong, and P. C. Lemaire, “A combined EPR and modulated photocurrent study of native defects in Bridgman grown vanadium doped cadmium telluride: the case of the tellurium antisite,” *Semicond. Sci. Technol.* **18**, 2003, p. 919–926.
- [32] V. Babentsov and R. B. James, “Anion vacancies in II-VI chalcogenides: Review and critical analysis,” *J. Cryst. Growth* **379**, 2013, p. 21–27.
- [33] A. Carvalho, A. K. Tagantsev, S. Öberg, P. R. Briddon, and N. Setter, “Cation-site intrinsic defects in Zn-doped CdTe,” *Phys. Rev. B* **81**, 2010, p. 075215.
- [34] K. Biswas and M. H. Du, “What causes high resistivity in CdTe,” *New J. Phys.* **14**, 2012, p. 063020.
- [35] M. H. Du, H. Takenaka, and D. J. Singh, “Carrier compensation in semi-insulating CdTe: First-principles calculations,” *Phys. Rev. B* **77**, 2008, p. 094122.
- [36] I. A. Hümmelgen and W. Schröter, “Deformation induced deep levels in p-CdTe,” *Appl. Phys. Lett.* **62**, 1993, p. 2703.
- [37] V. Babentsov, V. Boiko, R. Grill, J. Franc, and G. A. Shepelskii, “Point and

- nanoscale defects in Cd(S, Se, Te) crystals induced by plastic deformation,” *Phys. Status Solidi Curr. Top. Solid State Phys.* **7**, 2010, p. 1492–1494.
- [38] W. Shockley and W. T. Read, “Statistics of the Recombination of Holes and Electrons,” *Phys. Rev.* **87**, 1952, p. 835–842.
- [39] R. N. Hall, “Electron-Hole Recombination in Germanium,” *Phys. Rev.* **87**, 1952, p. 387–387.
- [40] S. Ramo, “Currents Induced by Electron Motion,” *Proc. IRE* **27**, 1939, p. 0–1.
- [41] Z. He, “Review of the Shockley-Ramo theorem and its application in semiconductor gamma-ray detectors,” *Nucl. Instruments Methods Phys. Res. Sect. A Accel. Spectrometers, Detect. Assoc. Equip.* **463**, 2001, p. 250–267.
- [42] Y. Cui, M. Groza, D. Hillman, A. Burger, and R. B. James, “Study of surface recombination velocity of Cd(1-x)Zn(x)Te radiation detectors by direct current photoconductivity,” *J. Appl. Phys.* **92**, 2002, p. 2556.
- [43] I. Pelant and J. Valenta, *Luminescence spectroscopy of semiconductors*. Oxford : Oxford University Press, 2012.
- [44] J. Prochazka, P. Hlidek, J. Franc, R. Grill, E. Belas, M. Bugar, V. Babentsov, and R. B. James, “Selective pair luminescence in the 1.4-eV band of CdTe:In,” *J. Appl. Phys.* **110**, 2011, p. 093103.
- [45] D. R. Vij, *Handbook of Electroluminescent Materials*. CRC Press, 2004.
- [46] S. Uxa, E. Belas, R. Grill, P. Praus, and R. B. James, “Determination of electric-field profile in CdTe and CdZnTe detectors using transient-current technique,” *IEEE Trans. Nucl. Sci.* **59**, 2012, p. 2402–2408.
- [47] H. Fujiwara, *Spectroscopic Ellipsometry: Principles and Applications*. Chichester, UK: John Wiley & Sons, Ltd, 2007.
- [48] J. Zazvorka, P. Hlidek, R. Grill, J. Franc, and E. Belas, “Photoluminescence of CdTe:In in the spectral range around 1.1eV,” *J. Lumin.* **177**, 2016, p. 71–81.
- [49] J. Zazvorka, P. Hlidek, J. Franc, J. Pekarek, and R. Grill, “Photoluminescence study of surface treatment effects on detector-grade CdTe : In,” *Semicond. Sci. Technol.* **31**, 2016, p. 25014.
- [50] G. Lucovsky, “On the photoionization of deep impurity centers in semiconductors,” *Solid State Commun.* **3**, 1965, p. 299–302.
- [51] M. A. Reshchikov, “Temperature dependence of defect-related photoluminescence in III-V and II-VI semiconductors,” *J. Appl. Phys.* **115**, 2014, p. 012010.

- [52] J. Zazvorka, J. Franc, V. Dedic, and M. Hakl, “Electric field response to infrared illumination in CdTe/CdZnTe detectors,” *J. Instrum.* **9**, 2014, p. C04038.
- [53] R. Kernocker, K. Lischka, and L. Palmethofer, “Luminescence of Fe⁺-implanted CdTe,” *J. Cryst. Growth* **86**, 1990, p. 625–628.
- [54] C. B. Norris, “Cathodoluminescence studies of postrange defect introduction from ion implantation in CdSe,” *J. Appl. Phys.* **53**, 1982, p. 5177–5181.
- [55] B. K. Meyer, H. Linke, P. Omling, M. Salk, and K. W. Benz, “Determination of the iron acceptor level in CdTe,” *Mater. Sci. Eng. B* **16**, 1993, p. 243–245.
- [56] S. R. Das, J. G. Cook, N. L. Rowell, and M. S. Aouadi, “Photoluminescence spectroscopy of CdTe epilayers grown by rf magnetron sputtering,” *J. Appl. Phys.* **68**, 1990, p. 5796–5803.
- [57] J. Lee, N. C. Giles, D. Rajavel, and C. J. Summers, “Donor-acceptor pair luminescence involving the iodine a center in CdTe,” *J. Appl. Phys.* **78**, 1995, p. 5669–5674.
- [58] D. Kuciauskas, P. Dippo, Z. Zhao, L. Cheng, A. Kanevce, W. K. Metzger, and M. Gloeckler, “Recombination Analysis in Cadmium Telluride Photovoltaic Solar Cells With Photoluminescence Spectroscopy,” *IEEE J. Photovoltaics* **6**, 2015, p. 313–318.
- [59] S. Uxa, R. Grill, and E. Belas, “Evaluation of the mobility-lifetime product in CdTe and CdZnTe detectors by the transient-current technique,” *J. Appl. Phys.* **114**, 2013 p. 094511.
- [60] K. Suzuki, T. Sawada, and K. Imai, “Effect of DC bias field on the time-of-flight current waveforms of CdTe and CdZnTe detectors,” *IEEE Trans. Nucl. Sci.* **58**, 2011, p. 1958–1963.
- [61] J. Pousset, I. Farella, S. Gambino, and A. Cola, “Subgap time of flight: A spectroscopic study of deep levels in semi-insulating CdTe:Cl,” *J. Appl. Phys.* **119**, 2016, p. 105701.
- [62] A. Hossain, A. E. Bolotnikov, G. S. Camarda, Y. Cui, S. Babalola, A. Burger, and R. B. James, “Effects of surface processing on the response of CZT gamma detectors: Studies with a collimated synchrotron X-ray beam,” *J. Electron. Mater.* **37**, 2008, p. 1356–1361.
- [63] J. Crocco, H. Bensalah, Q. Zheng, F. Dierre, P. Hidalgo, J. Carrascal, O. Vela, J. Piqueras, and E. Dieguez, “Study of the effects of edge morphology on

- detector performance by leakage current and cathodoluminescence,” in *IEEE Trans. Nucl. Sci.* **58**, 2011, p. 1935–1941.
- [64] G. Zha, W. Jie, T. Tan, and X. Wang, “Effect of surface treatments on the electrical and optical properties of CdZnTe single crystal,” *Nucl. Instruments Methods Phys. Res. Sect. A Accel. Spectrometers, Detect. Assoc. Equip.* **566**, 2006, p. 495–499.
- [65] J. Crocco, H. Bensalah, Q. Zheng, V. Corregidor, E. Avles, A. Castaldini, B. Fraboni, D. Cavalcoli, A. Cavallini, O. Vela, and E. Dieguez, “Study of asymmetries of Cd(Zn)Te devices investigated using photo-induced current transient spectroscopy, Rutherford backscattering, surface photo-voltage spectroscopy, and gamma ray spectroscopies,” *J. Appl. Phys.* **112**, 2012, p. 074503.
- [66] V. A. Gnatyuk, O. I. Vlasenko, S. N. Levytskyi, E. Dieguez, J. Crocco, H. Bensalah, M. Fiederle, A. Fauler, and T. Aoki, “Surface processing of CdZnTe crystals,” *Proc. SPIE* **8507**, 2012, p. 85071S.
- [67] A. Burger, H. Chen, K. Chattopadhyay, D. Shi, S. H. Morgan, W. E. Collins, and R. B. James, “Characterization of metal contacts on and surfaces of cadmium zinc telluride,” *Nucl. Instruments Methods Phys. Res. Sect. A Accel. Spectrometers, Detect. Assoc. Equip.* **428**, 1999, p. 8–13.
- [68] A. J. Nelson, A. M. Conway, C. E. Reinhardt, J. L. Ferreira, R. J. Nikolic, and S. A. Payne, “X-ray photoemission analysis of passivated Cd(1 - x)ZnxTe surfaces for improved radiation detectors,” *Mater. Lett.* **63**, 2009, p. 180–181.
- [69] Q. Zheng, F. Dierre, J. Franc, J. Crocco, H. Bensalah, V. Corregidor, E. Alves, E. Ruiz, O. Vela, J. M. Perez, and E. Dieguez, “Investigation of generation of defects due to metallization on CdZnTe detectors,” *J. Phys. D. Appl. Phys.* **45**, 2012, p. 175102.
- [70] S. Tari, F. Aqariden, Y. Chang, C. Grein, J. Li, and N. Kioussis, “Impact of surface treatment on the structural and electronic properties of polished CdZnTe surfaces for radiation detectors,” *J. Electron. Mater.* **42**, 2013, p. 3252–3258.
- [71] V. G. Ivanitska, P. Moravec, J. Franc, Z. F. Tomashik, P. I. Feychuk, V. M. Tomashik, L. P. Shcherbak, K. Masek, and P. Hoschl, “Chemical Etching of CdTe in Aqueous Solutions of H₂O₂-HI-Citric Acid,” *J. Electron. Mater.* **36**, 2007, p. 1021–1024.

- [72] Y. Cui, M. Groza, A. Burger, and R. B. James, "Effects of Surface Processing on the Performance of Cd_{1-x}Zn_xTe Radiation Detectors," *IEEE Trans. Nucl. Sci.* **51**, 2004, p. 1172–1175.
- [73] M. C. Duff, D. B. Hunter, A. Burger, M. Groza, V. Buliga, and D. R. Black, "Effect of surface preparation technique on the radiation detector performance of CdZnTe," *Appl. Surf. Sci.* **254**, 2008, p. 2889–2892.
- [74] H. Bensalah, J. L. Plaza, J. Crocco, Q. Zheng, V. Carcelen, A. Bensouici, and E. Dieguez, "The effect of etching time on the CdZnTe surface," *Appl. Surf. Sci.* **257**, 2011, p. 4633–4636.
- [75] A. Bensouici, V. Carcelen, J. L. Plaza, S. De Dios, N. Vijayan, J. Crocco, and H. Bensalah, "Study of effects of polishing and etching processes on Cd_{1-x}Zn_xTe surface quality," *J. Cryst. Growth* **312**, 2010, p. 2098–2102.
- [76] G. Zha, W. Jie, T. Tan, and P. Li, "The surface leakage currents of CdZnTe wafers," *Appl. Surf. Sci.* **253**, 2007, p. 3476–3479.
- [77] W. Xiaoqin, J. Wanqi, L. Qiang, and G. Zhi, "Surface passivation of CdZnTe wafers," *Mater. Sci. Semicond. Process.* **8**, 2005, p. 615–621.
- [78] H. Yoon, J. M. V. A. N. Scyoc, and M. S. Goorsky, "Investigation of the Effects of Polishing and Etching on the Quality of Cd_{1-x}Zn_xTe Using Spatial Mapping Techniques," *J. Electron. Mater.* **26**, 1997, p. 529–533.
- [79] M. Prokesch and C. Szeles, "Accurate measurement of electrical bulk resistivity and surface leakage of CdZnTe radiation detector crystals," *J. Appl. Phys.* **100**, 2006, p. 014503.
- [80] J. Krustok, H. Collan, K. Hjelt, J. Madasson, and V. Valdna, "Photoluminescence from deep acceptor-deep donor complexes in CdTe," *J. Lumin.* **72–74**, 1997, p. 103–105.
- [81] J. Franc, M. Fiederle, V. Babentsov, A. Fauler, K. W. Benz, and R. James, "Defect structure of Sn-doped CdTe," *J. Electron. Mater.* **32**, 2003, p. 772–777.
- [82] J. Franc, H. Elhadidy, V. Babentsov, A. Fauler, and M. Fiederle, "Comparative study of vertical gradient freeze grown CdTe with variable Sn concentration," *J. Mater. Res.* **21**, 2006, p. 1025–1032.
- [83] J. Zazvorka, J. Franc, P. Moravec, E. Jesenska, L. Sedivy, J. Ulrych, and K. Masek, "Contactless resistivity and photoconductivity correlation to surface preparation of CdZnTe," *Appl. Surf. Sci.* **315**, 2014, p. 144–148.

- [84] V. Babentsov, V. Boiko, G. A. Schepelskii, R. B. James, J. Franc, J. Prochazka, and P. Hlidek, "Photoluminescence and electric spectroscopy of dislocation-induced electronic levels in semi-insulated CdTe and CdZnTe," *J. Lumin.* **130**, 2010, p. 1425–1430.
- [85] F. Halle, L. Pacs, G. L. I. Other, S. Hildebrandt, H. Uniewski, J. Schreiber, and H. S. Leipner, "Localization Telluride of Y Luminescence at Glide Dislocations in Cadmium," *J. Phys. III France* **7**, 1997, p. 1505–1514.
- [86] J. Schreiber, L. Horing, H. Uniewski, S. Hildebrandt, and H. S. Leipner, "Recognition and distribution of A(g) and B(g) dislocations in indentation deformation zones on {111} and {110} surfaces of CdTe," *Phys. Status Solidi Appl. Res.* **171**, 1999, p. 89–97.
- [87] D. P. Halliday, M. D. G. Potter, J. T. Mullins, and A. W. Brinkman, "Photoluminescence study of a bulk vapour grown CdTe crystal," *J. Cryst. Growth* **220**, 2000, p. 30–38.
- [88] M. Cardenas-Garcia, J. Aguilar-Hernandez, and G. Contreras-Puente, "Study of the radiative mechanism of the 1.471-eV luminescent band in polycrystalline CdTe films," *Thin Solid Films* **480–481**, 2005, p. 269–272.
- [89] P. Hidalgo, J. Piqueras, N. V. Sochinskii, M. Abellan, E. Saucedo, and E. Dieguez, "Cathodoluminescence study of CdTe crystals doped with Bi and Bi:Yb," *J. Mater. Sci.* **43**, 2008, p. 5605–5608.
- [90] A. Hossain, A. Dowdy, A. E. Bolotnikov, G. S. Camarda, Y. Cui, U. N. Roy, R. Tappero, X. Tong, G. Yang, and R. B. James, "Topographic evaluation of the effect of passivation in improving the performance of CdZnTe detectors," *J. Electron. Mater.* **43**, 2014, p. 2941–2946.
- [91] S. U. Egarievwe, A. Hossain, I. O. Okwechime, R. Gul, and R. B. James, "Effects of Chemomechanical Polishing on CdZnTe X-ray and Gamma-Ray Detectors," *J. Electron. Mater.* **44**, 2015, p. 3194–3201.
- [92] G. Wright, Y. Cui, U. N. Roy, C. Barnett, K. Reed, A. Burger, F. Lu, L. Li, and R. B. James, "The Effects of Chemical Etching on the Charge Nuclear Radiation Detectors," *IEEE Trans. Nucl. Sci.* **49**, 2002, p. 2521–2525.
- [93] S. S. Choi, "Native oxide formation on CdTe," *J. Vac. Sci. Technol. B Microelectron. Nanom. Struct.* **6**, 1988, p. 1198.
- [94] H. W. Yao, J. C. Erickson, H. B. Barber, R. B. James, and H. Hermon, "Optical properties of Cd_{0.9}Zn_{0.1} Te studied by variable angle spectroscopic

- ellipsometry between 0.75 and 6.24 eV,” *J. Electron. Mater.* **28**, 1999, p. 760–765.
- [95] G. Badano, A. Million, B. Canava, P. Tran-Van, and A. Etcheberry, “Fast detection of precipitates and oxides on CdZnTe surfaces by spectroscopic ellipsometry,” *J. Electron. Mater.* **36**, 2007, p. 1077–1084.
- [96] M. E. Ozsan, P. J. Sellin, P. Veeramani, S. J. Hinder, M. L. T. Monnier, G. Prekas, A. Lohstroh, and M. A. Baker, “Chemical etching and surface oxidation studies of cadmium zinc telluride radiation detectors,” *Surf. Interface Anal.* **42**, 2010, p. 795–798.
- [97] M. K. Bahl, R. L. Watson, and K. J. Irgolic, “X-ray photoemission studies of tellurium and some of its compounds,” *J. Chem. Phys.* **66**, 1977, p. 5526.

List of Tables

<i>Table 3.1 CdTe samples used for the investigation.....</i>	<i>24</i>
<i>Table 3.2 CdZnTe samples used for the investigation.....</i>	<i>24</i>
<i>Table 4.1 The most abundant impurities of CdTe-III sample as determined by GDMS.....</i>	<i>27</i>
<i>Table 4.2 Luminescence bands observed in CdTe doped with In at 4 K. See [49] for references.....</i>	<i>29</i>
<i>Table 4.3 Activation energies deduced from PL thermal quenching at relatively high temperatures at above-gap excitation compared to estimated ZPL energies at 4 K (published in [48]). The values 1.430 and 1.450 are for the stronger component of the band 8.....</i>	<i>45</i>
<i>Table 4.4 The most abundant impurities of CZT-II sample as determined by GDMS.....</i>	<i>48</i>
<i>Table 4.5 Luminescence bands observed in CZT-I doped with In at 4 K. See [49] for references.....</i>	<i>49</i>
<i>Table 5.1 Parameters for the theoretical model simulation of the bandgap effects.....</i>	<i>74</i>
<i>Table 6.1 Surface preparation methods and parameters.....</i>	<i>83</i>
<i>Table 6.2 Average resistivity and photoconductivity values for sample No. 2 with different surface preparation.....</i>	<i>91</i>

Symbols and abbreviations

E_G	bandgap energy
Z	atomic number
VGF	vertical–gradient–freeze
THM	travelling–heater–method
SPECT	single–photon emission computed tomography
GDMS	glow–discharge mass spectroscopy
PL	photoluminescence
PICTS	photo–induced current transient spectroscopy
DLTS, I–DLTS	deep level transient spectroscopy, current induced DLTS
TEES	thermo–electric effect spectroscopy
k_B	Boltzmann constant
T	temperature
E_C, E_V	minimal value of conduction band and maximal value of valence band, respectively
E_D, E_A	energy of deep donor and acceptor, respectively
$n(E)$	density of states
$j_{e,h}$	electrical current density for electrons and holes, respectively
e	elemental charge
n,p	concentration of free electrons and holes, respectively
$\mu_{e,h}$	mobility of electron and holes, respectively
E	electric field
$\zeta_{n,h}$	Soret coefficient for electrons and holes, respectively
$\sigma_{n,h}$	conductivity of electrons and holes, respectively
n_0	electron concentration of a non–illuminated sample
Δn	addition electron concentration created by sample illumination
E_t	deep level energy
N_t	deep level concentration
$S_{e,h}$	trapping cross–section for electrons and holes, respectively
n_t	concentration of electrons present on deep level
$\nu_{e,h}$	electron and hole trapping speed, respectively
$\gamma_{e,h}$	trapping rate of electrons and holes, respectively
$\alpha_{e,h}$	probability of a thermal release for electrons and holes

N_C	amount of energy states in conduction band
Q	charge
Φ_0	electric potential
v	charge carrier velocity
i	electrical current
CCE	charge collection efficiency
U	electrical bias
L	sample width
$\tau_{e,h}$	lifetime of electrons and holes, respectively
ZPL	zero phonon line
$\hbar\omega$	energy of light with distinct wavelength
SPL	selective pair luminescence
COREMA	contactless resistivity mapping
TDCM	time dependent charge measurement
R_S	sample resistance
C_S, C_A	capacity of sample and air gap, respectively
τ_S	charging time
ρ	resistivity
ϵ_0, ϵ_r	vacuum and relative permittivity, respectively
g	photoconductivity obtained by the contactless method
TCT, L-TCT	transient-current-technique, laser-induced TCT
MSE	mean squared error
E_F	Fermi level
DAP	donor-acceptor pair
FE	free exciton
(D^0, X) ;	recombination of excitons bound to neutral donors
(A^0, X) ;	recombination of excitons bound to neutral acceptors
LN	liquid nitrogen
PLE	excitation dependent photoluminescence
CB, VB	conduction band and valence band, respectively
φ	photon flux
IR	infrared
IV	current-voltage
t_r	transit time
μ^{eff}	effective mobility

a	screening parameter
N	normalized charge density
E_S	shallow level energy
$\chi_{e,h}$	capture cross-section for electrons and holes, respectively
XPS	X-ray photoelectron spectroscopy
AFM	atomic force microscopy
Br-methanol	bromine-methanol
RMS	root mean square
EMA	effective medium approximation
MSA	multi-sample-analysis
VASE	variable angle spectroscopic ellipsometry

Epilogue

"In the end, I am not interested in that which I fully understand. The words I have written over the years are just a veneer. There are truths that lie beneath the surface of the words. Truths that rise up without warning like the humps of the seamount and then disappear. What [science and research] is to me is finding a way to tempt the monster to the surface. To create a space where the creature can break through what is real and what is known to us. This shimmering space, where imagination and reality intersect [...]. This is the place. This is where we live."

Nick Cave: 20,000 Days on Earth, Dir. I. Forsyth & J. Pollard,
Channel 4 DVD, 2014